University of Alberta
Department of Civil &
Environmental Engineering

Structural Engineering Report No. 197

Prediction of Wrinkling Behavior of Girth-Welded Line Pipe

by

L.T. Souza

and

D.W. Murray

April 1994

Structural Engineering Report 197
Department of Civil Engineering
University of Alberta

PREDICTION OF WRINKLING BEHAVIOR OF GIRTH-WELDED LINE PIPE

A Report to the
National Energy Board of Canada
311 - 6th Avenue S.W.
Calgary AB T2P 3H2

by
L.T. Souza
and
D.W. Murray

1994

Structural Engineering Report 197
Department of Civil Engineering
University of Alberta

EXECUTIVE SUMMARY

Context of report

This report was produced under a research grant from the National Energy Board of Canada with additional financial support from Interprovincial Pipe Line Company Ltd., Edmonton, Alberta. It is one of a series of publications that has arisen from research into the behavior of pipelines, as undertaken within the structural engineering group of the Department of Civil Engineering of the University of Alberta (U of A) in recent years. A list of the publications from this group that have appeared, are in press, or are in preparation is given in Appendix B. An additional study to develop user-friendly menu driven programs in order to make feasible the application of these developments, for design and assessment of pipelines in the standard design office, is now in the planning stage (summer, 1994). The studies undertaken have consisted of both experimental and analytical work and cover a relatively wide range of parameters. A brief review of the work completed to date is contained in the Introduction to the report.

It should be understood, however, that the present report is intended to cover only a specific portion of the scope of the work referred to in the paragraph above. Its primary purpose is to describe the procedures and establish the validity of an analytical methodology for predicting the behavior of girth-welded line pipe under the action of constant internal pressure (the design pressure), constant axial load, and monotonically increasing imposed curvatures. In order to establish this validity, the results of the analyses are compared to some of the results of the experimental work. However, full reports on the experimental work, both with respect to the experimental techniques and with respect to the analysis and interpretation of the results, will be left to other publications and should not be expected herein.

The unique aspect of the pipeline analyses associated with the research work described above is the realistic inclusion of wrinkling behavior. The characteristics of this type of pipe behavior are established from three-dimensional finite element analysis of pipe segments. These characteristics are then incorporated into a two dimensional interactive soil-structure pipeline-beam analysis in order that the development of wrinkling may be predicted and the assessment of the significance of this wrinkling may be made for pipelines under service conditions. The present report is confined to discussing analysis for the realistic prediction of the three-dimensional behavior of segments of line pipe in the vicinity of girth welds. The report is divided into two parts: Part A and Part B. Part A deals with the presentation of results obtained using the recommended modelling procedures. Part B deals with the effects that variations in the modelling procedures may have on these results. A brief description of the report contents and some major conclusions follows.

Content and Conclusions of Part A of Report

Part A deals first with a description of previous work undertaken at the University of Alberta and attempts to place the present report in context (Chapter 1- Introduction). It then describes the computer modelling technique, using the ABAQUS computer code, for the numerical simulation of a specific set of specimens that composed an experimental test series on full-sized girth-welded pipe. This set of tests is referred to as the 1993 Test Series to distinguish it from the test series on plain pipe that is referred to as the 1992 Test Series.

It was found that, in order to predict the proper deformed configurations in the post-buckling range for girth-welded pipe, it is necessary to include in the mesh refinement: (i) weld elements of the same dimensions as the weld size; (ii) a gradual variation in the element dimensions as the weld is approached (see Fig. 2.1.2); (iii) the effects of imperfect geometric mismatch of the pipe cross-sections at the junction of the cans (see Fig. 2.4.1) ; and (iv) the residual stresses generated by the welding process (see Fig. 2.3.2). It was also found that the most reliable results are obtained for a finite strain element (see Part B). Chapter 2 discusses all of these factors as adopted for the recommended modelling procedure. Because the components of the model can vary widely, a system of notation to describe the detail incorporated into the various models of all specimens is introduced, as defined in Table 2.4.2.

Chapter 3 presents the results of the analyses for all seven of the specimens in the 1993 Test Series. It compares the analytical predictions with the experimental observations with respect to moment-curvature curves and the deformed configurations. Each specimen comparison is treated in a separate section. (For instance, see Sect. 3.2.1 for the results associated with specimen UGA12W.) It is concluded in Chapter 4 that the recommended analytical techniques produce results that closely simulate the real behavior of the pipe segments up to and including deformed configurations associated with very large wrinkles.

Content and Conclusions of Part B of Report

The function of Part B is to present the effect of changes in the finite element models on the results predicted by the models. It was the investigation of such effects that formed the basis for the recommendations for the modelling procedure adopted in Part A. It should be noted that experimental results for both plane and girth-welded pipe indicate that unpressurized pipe (i.e.- empty pipe) ultimately assumes a diamond pattern while pressurized pipe generally assumes a configuration with one dominant outward buckle.

Section 6.1 presents the results of six different mesh and element type combinations for the analysis of the plain pipe specimen UGA20. The uniform meshes and the finite strain mesh all ultimately give proper diamond forms of deformed configurations. However, further comparisons for moment vs. curvature curves for specimens UGA20W and HGA20W, in Sect. 6.2, indicate that the model with the finite strain element is the one to be preferred.

The influence of geometric misalignment and residual stresses are investigated in Chapter 7. It is demonstrated in Sect. 7.1, that geometric misalignment of the elliptic type was necessary in order to develop the proper diamond shape pattern in the unpressurized 12 inch pipe. Hence, elliptic misalignment was incorporated into the recommended model. In Sect. 7.2, analytical results for the 20 inch girth-welded pipe, with elliptic mismatch and residual stress, are compared with analytical results for plain pipe. The effect of the weld on the moment vs. curvature curve is significant for the empty pipe but practically disappears for fully pressurized pipe.

Chapter 8 gives a brief summary of the experience of the authors' and their recommendations with respect to modelling for the analysis of line pipe segments.

TABLE OF CONTENTS

PART A
ANALYTICAL SOLUTIONS AND EXPERIMENTAL VERIFICATION

PART B
ANALYTICAL EXPERIENCE AND INFLUENCE OF MODELLING TECHNIQUE ON SOLUTIONS

LIST OF TABLES FOR PART A

LIST OF FIGURES FOR PART A

LIST OF TABLES FOR PART B

LIST OF FIGURES FOR PART B

Structural Engineering Report 197
Department of Civil Engineering
University of Alberta

PREDICTION OF WRINKLING BEHAVIOR OF GIRTH-WELDED LINE PIPE

PART A

ANALYTICAL SOLUTIONS AND EXPERIMENTAL VERIFICATION

1.0 INTRODUCTION

1.1 OVERVIEW OF PROBLEM AND DESCRIPTION OF STATE-OF-THE-ART AT THE UNIVERSITY OF ALBERTA

1.1.1 Behavioral Considerations

As stated in the Executive Summary, this report is one of a series of publications that has arisen from research into the behavior of pipelines as undertaken within the structural engineering group of the Department of Civil Engineering of the University of Alberta (U of A) in recent years. The work has as its general objective the realistic prediction of the physical behavior of buried pipe when subjected to the various loading combinations that may arise in field situations.

One of the conditions that pipelines may be subjected to in the field is the imposition of large displacements resulting from geotechnical movements of the surrounding soil. For an operating pipeline, these movements are imposed while the pipe is sustaining both its internal design pressure and an axial thrust that is dependent on the temperature differential between the operating condition and the tie-in condition. For large relative geotechnical movements as, for instance, might occur for settlements at the interface between thaw-stable and thaw unstable zones in discontinuous permafrost, the pipe may be subjected to severe bending resulting in large curvatures. Sooner or later, any line pipe subjected to large curvatures will buckle locally and develop wrinkles. The strains under these conditions can be considerably in excess of limiting strains as currently stated in the applicable codes and standards. The question that arises is: At what strain limit, or alternative deformation state, is it necessary to remove the pipe from service or undertake other remedial action? The research work undertaken in the structures group at the University of Alberta (U of A) has been directed to answering this question in a generic way.

A pipe is a three-dimensional shell structure. For pipeline applications under realistic conditions the pipe usually does not deform excessively until it has developed significant plastic response. In order to predict behavior for complex response, such as local buckling or post-buckling wrinkling, it is necessary to understand the behavior of three-dimensional shell structures and to be able to predict their three-dimensional large -displacement large - strain elastic - plastic behavior. Analysis to predict such behavior is not a simple matter, but with modern finite element computational methods it is feasible. Significant progress in developing such analyses have been made in this investigation.

1.1.2 Initial Analytical Work at U of A

The development at the U of A began with the work of Dr. Zhilong Zhou who made important conceptual contributions to the analysis of underground pipelines. In particular, he devised a way to carry out shell analysis of line pipe well into the wrinkling range and to extract stiffness-property-deformation relations from these analyses that permitted the incorporation of local buckling into the analysis of pipelines. (This work was, however, very demanding and because of time and resource limits had to be confined to one size of pipe.) He then designed and implemented a pipeline program, designated as ABP for Analysis of Buried Pipelines, with capabilities similar to PIPLIN-III (1989), that allows the effect of wrinkling to be incorporated into the line-of-pipe analysis.

Dr. Zhou's studies of soil-structure interaction for pipelines, undertaken with the ABP program for line-of-pipe analysis, demonstrated that for large settlements, because of the softening of the pipe response due to local buckling, a single wrinkle is triggered at each end of the flexural zone that forms around a settlement transition region. The settlement at which this wrinkling is triggered was computed and the settlement associated with any selected deformation criterion for the pipe can also be computed.

Publications arising from the work of Dr. Zhou are listed in Appendix B. These consist of his structural engineering report (Zhou and Murray B1993a[1]), an OMAE conference paper (Zhou and Murray B1993b), an ISOPE conference paper (Zhou and Murray B1993c), and three journal papers presently under review (Zhou and Murray B1994a; Zhou and Murray B1994b; and, Zhou and Murray B1994c).

---

[1] References for which the date is preceeded by a B refer to those in Appendix B.

1.1.3 Experimental Work at U of A

1.1.3.1 Plain Pipe: 1992 Test Series

It was recognized early in this work that the analytical predictions carried out involved innovative techniques for the pipeline industry and were breaking new ground for applications of shell theory. In order for the predictions to be given credibility it was necessary to carry out experimental work on full-sized pipe to determined its behavioral characteristics and to verify that the analyses were capable of representing correctly and realistically the pipe response. A set of pipe tests on full-sized pipe with realistic simulation of field loading conditions was designed and executed, in 1992, by Mohareb (Mohareb, *et al,* B1992; Mohareb, *et al,* B1993; and, Mohareb, *et al,* B1994).

The technique used by Mohareb to test the line pipe specimens is similar to that used for eccentric column testing in civil engineering structural research. This was used in lieu of the 'four point bend test' that is more common in the pipeline industry. The innovation proved highly successful and much more economical than bend testing. A schematic of the test set-up is shown in Fig. 1.1.1. The internal pressure is kept constant. The axial force, C, in the pipe wall was also kept constant. Bending moments up to the maximum capacity of the pipe, and beyond, can be applied by varying the relative displacement between the outrigger arms that are attached to the end of the specimen. As the force F varies, the axial force, P, delivered by a large MTS Universal testing machine is also varied in order that the predetermined force in the pipe wall, C, remains constant.

A total of seven specimens, four of 20 inch (508 mm) diameter and three of 12.75 inch (324 mm) diameter, were tested. Details of the test specimens and their loading are given in Table 1.1. It is recommended that the reader spend some time becoming familiar with the interpretation of the designations used for the test names, as shown in Column 1 of Table 1, in order to differentiate between the pipe sizes and loading conditions for the various specimens. The definitions of the characters composing the designations are given in the Notes to Table 1.1. These designations, and variations of them, will be used throughout this work in order to identify both experimental specimens and their analytical models.

A typical plot of the test results for the variation of the forces applied to an experimental specimen, as the relative rotation between the end loading arms is increased, is shown in Fig. 1.1.2. The bending moment on the ends of the specimen is proportional to the eccentric load, F. For deformations in excess of a certain limiting relative rotation, designated as the softening point (SP) that is approximately 4.4 degrees in Fig. 1.1.2, the moment decreases as the rotation continues to increase. This softening of the moment capacity occurs coincidentally with the development of a wrinkle in the pipe and is a significant behavioral characteristic of pipes subjected to monotonically increasing curvatures such as those that would occur as a result of continuing settlements related to geotechnical movements.

A photograph of the test set-up for the tests of Mohareb is shown in Fig 1.1.3. These tests are presently being processed to digest the data and present it in a manner that is the most relevant characterization for the local buckling behavior of plain pipe specimens. Details will appear in Mohareb, *et al*, (B1994).

1.1.3.2 Girth-Welded Pipe: 1993 Test Series

Because girth welds introduce residual stresses and initial imperfections into the pipe, limiting strains for buckling and development of wrinkles are expected to be different for welded pipe than those associated with the plain pipe of the 1992 Series. To determine the effect of girth welds on the response of the pipe, and how they influence the different limiting conditions of pipe behavior, a series of girth-welded specimens were tested in 1993 by Yoosef-Ghodsi (Yoosef-Ghodsi, *et al*, B1994b). It was the intent of this 1993 test series to replicate exactly the specimens of the 1992 test series with the only difference being the presence of the girth-weld at mid-length of the specimens.

The seven specimens and their loading conditions for the 1993 series of girth-welded pipes are defined in Table 1.2. The acronyms that designate the test specimens are constructed in the same way as for Table 1.1 except that they are followed by a W, indicating that the test is of a welded pipe. Because of difficulties in executing test UGA20W, two tests of this type were run, indicated by the '-1' and '-2' on the specimen designations on lines 1 and 2 of Table 1.2.

1.2 OBJECTIVE AND ORGANIZATION OF REPORT

The analytical modelling of the 1993 girth-welded specimens is more difficult than the modelling of the 1992 plain pipe specimens because of: (i) the misalignments that arise in the fit-up of the two cans that are joined at the weld, (ii) the change in material properties that are introduced by the heat effected zone, (iii) the residual stresses that arise from the welding process, and (iv) pinching deformations that arise at the weld from the thermal contractions and that contribute to initial imperfections.

It is the purpose of this report to examine the techniques of modelling the girth-welded pipe specimens to determine if the state-of-the-art of analytical methods is adequate to simulate with confidence the response of such specimens. If the answer to this question is in the affirmative, then this investigation should determine the best modelling procedures and make recommendations as to what procedures should be used to insure that reliable results will be obtained from analyses.

There are a great many variables in the selection of a model for the analysis of a pipe segment (or specimen) and it is easy to get lost and confused in the abundance of details associated with the modelling procedure. For this reason the following strategy is employed in this report. In **Part A** the techniques, and the results therefrom, are presented for what is, in the opinion of the writers, the best modelling of these problems. They believe that the results form these analyses permit an affirmative response to the question in the above paragraph. Therefore, **Part A** describes implicitly the procedures and modelling techniques that the authors would recommend for the analysis of similar pipe problems.

Part B then examines the effects of variations to individual modelling parameters. The reader may use these results to form judgments as to the importance of the individual features of the recommended model and the sensitivity of the solutions with respect to deviations from the recommended procedures.

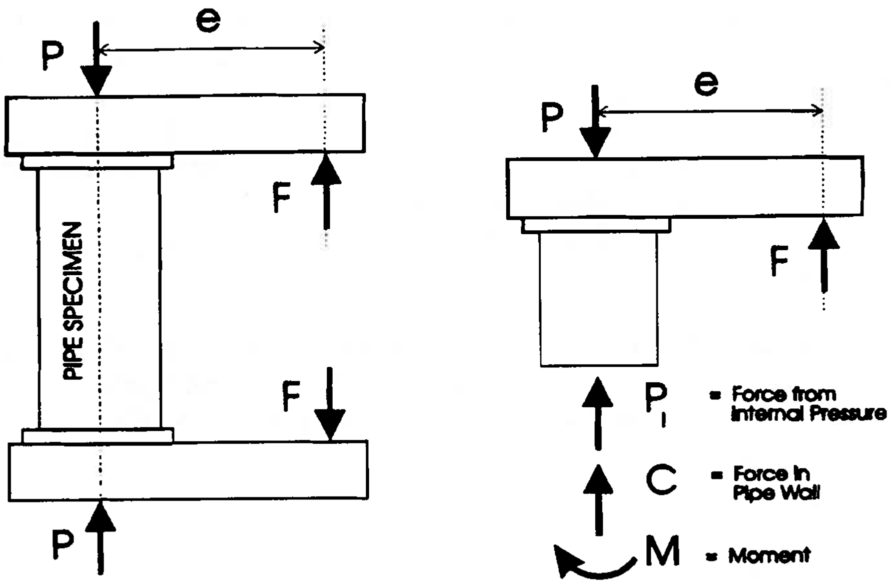

(a) Specimen (b) Free Body Diagram

Fig. 1.1.1
Schematic of Test Set-Up and Load Definition

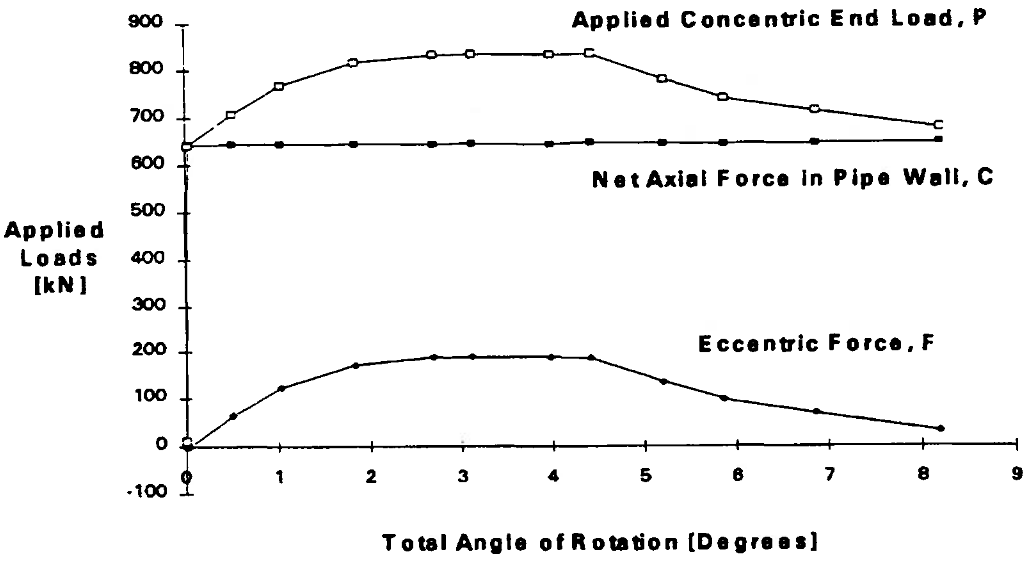

Fig. 1.1.2
Applied Load vs. Rotation for UGA12

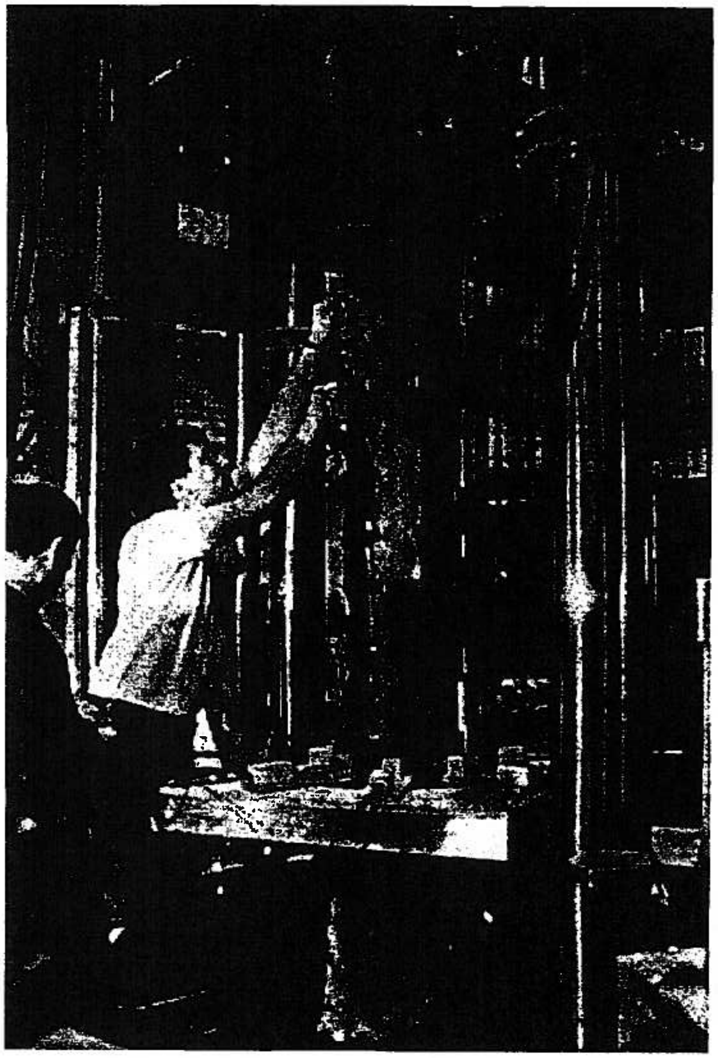

Figure 1.1.3. Pipe test in progress for 12inch specimen

Table 1.1
Experimental Specimens : 1992 Test Series

TEST	PIPE LOADING			END LOADING	
NAME	*VARIABLE M*	*CONSTANT P FOR σ_θ of*	*C_A=ACTIVE C_R=REACTIVE*	*P_I*	*$P= C + P_I + F$*
1 : UGA20	e F		$C_A=0.27\ C_Y$		$0.27C_Y+ F$
2 : UGR20	e F		$C_A=0.27\ C_Y$		$0.27C_Y+ F$
3 : DGA20	e F	$0.8\ \sigma_y$	$C_A=0$	$0.4\ C_Y$	$0.4C_Y+ F$
4 : DLR20	e F	$0.8\ \sigma_y$	$C_A= -0.24C_Y$	$0.4\ C_Y$	$0.16C_Y+ F$
5 : UGA12	e F		$C_A=0.29\ C_Y$		$0.29C_Y+ F$
6 : HGA12	e F	$0.36\ \sigma_y$	$C_A=0.18\ C_Y$	$0.18\ C_Y$	$0.36C_Y+ F$
7 : DGA12	e F	$0.72\ \sigma_y$	$C_A=0.08\ C_Y$	$0.36\ C_Y$	$0.44C + F$

NOTES TO TABLE 1.1

Pipe Specimens:

All are of 66.5 inch (1690 mm) length.

20 inch =20.0 ID x 0.312 inch DSAW X56 Grade =508 ID x 7.9 mm DSAW Grade 386 MPa

12 inch = 12.75 OD x 0.25 inch ERW X52 Grade = 324 OD x 6.4 mm ERW Grade 358 MPa

TEST DESIGNATIONS:

The tests are denoted by an **XYZnn(W)** specimen descriptor where:

X = either **U**, **D**, or **H** in which **U** = Upstream (or empty), **D** = Downstream (or fully pressurized) and **H** = Halfway between U and **D**. Upstream and downstream refer to the location of the pipe relative to the pumping station. The downstream pressure is approximately 9.65 MPa for the 20-inch pipe. The upstream pressure is approximately 0.34 MPa for the same pipe. Consequently, there is no essential difference between an empty and an upstream condition, and a zero pressure will be used to represent both of these conditions.

Y = either **G** or **L** where **G** = Greatest thermal effect and **L** = Least thermal effect.

Z = either **A** or **R** where **A** = Active axial force (or constant force) and **R** = Reactive axial force (or constant end location).

nn = nominal diameter of the pipe in inches.

W = indicates the existence of a girth weld at the midheight of the specimen (**W** = Weld).

NOTES TO DETERMINE TEST LOADINGS:

(For Grade 386 material, σ_y=56 ksi = 386 MPa)

1. Temperature Differential (C^t)
   $\sigma^t = 11.7\text{x}10^{-6}\text{x}45\text{x}200000 = 105$ MPa
   $= 0.27\ \sigma_y$ or $C^t=0.27\ C_y$
2. Poisson Effect (C^v)
   $\sigma^v= 0.3\ (0.8\ \sigma_y) = 0.24\ \sigma_y$
   $C^v= 0.24\ C_y$
3. Downstream Condition (maximum p_i)
   $\sigma_\theta = 0.8\ \sigma_y$ (for maximum p_i)
   $C^{vt} = (0.27 - 0.24)\ C_y = 0.03\ C_y \cong 0$
4. Upstream Condition (for minimum p_i)
   $\sigma_\theta = 0 \qquad p_i = 0$
   $C = 0.27\ C_y$
5. End Pressure Load (for maximum p_i)
   $P_i = A\ \sigma_\theta/\ 2 = 0.4\ C_y$
6. For 12-inch pipe, downstream pressure corresponds to $\sigma_\theta = 0.72\ \sigma_y$ and σ_y= 52 ksi= 358 MPa. This changes the above values to those listed in the table for tests 5, 6 and 7.

Table 1.2
Experimental Girth-Welded Specimens : 1993 Test Series

TEST	PIPE LOADING			END LOADING	
NAME	*VARIABLE M*	*CONSTANT p FOR* σ_θ *of*	C_A*=ACTIVE* C_R*=REACTIVE*	P_l	$P = C + P_l + F$
1 : UGA20W-1	e F		C_A=0.27 C_Y		0.27C_Y+ F
2 : UGA20W-2	e F		C_A=0.27 C_Y		0.27C_Y+ F
3 : HGA20W	e F	0.4 σ_y	C_A=0.15 C_Y	0.2 C_Y	0.35C_Y+ F
4 : DGA20W	e F	0.8 σ_y	C_A=0	0.4 C_Y	0.4 C_Y+ F
5 : UGA12W	e F		C_A=0.29 C_Y		0.29C_Y+ F
6 : HGA12W	e F	0.36 σ_y	C_A=0.18 C_Y	0.18 C_Y	0.36C_Y+ F
7 : DGA12W	e F	0.72 σ_y	C_A=0.08 C_Y	0.36 C_Y	0.44C + F

NOTES TO TABLE 1.2

Pipe Specimens:

All are of 66.5 inch (1690 mm) length.

20 inch= 20.0 ID x 0.312 inch DSAW X56 Grade= 508 ID x 7.9 mm DSAW Grade 386 MPa
12 inch = 12.75 OD x 0.25 inch ERW X52 Grade = 324 OD x 6.4 mm ERW Grade 358 MPa

TEST DESIGNATIONS:

The tests are denoted by an **XYZnn(W)** specimen descriptor where:

X = either **U**, **D**, or **H** in which **U** = Upstream (or empty), **D** = Downstream (or fully pressurized) and **H** = Halfway between U and D. Upstream and downstream refer to the location of the pipe relative to the pumping station. The downstream pressure is approximately 9.65 MPa for the 20-inch pipe. The upstream pressure is approximately 0.34 MPa for the same pipe. Consequently, there is no essential difference between an empty and an upstream condition, and a zero pressure will be used to represent both of these conditions.

Y = either **G** or **L** where **G** = Greatest thermal effect and **L** = Least thermal effect.

Z = either **A** or **R** where **A** = Active axial force (or constant force) and **R** = Reactive axial force (or constant end location).

nn = nominal diameter of the pipe in inches.

W = indicates the existence of a girth weld at the midheight of the specimen (W = Weld).

NOTES TO DETERMINE TEST LOADINGS:

(For Grade 386 material, σ_y=56 ksi = 386 MPa)

1. Temperature Differential (C^t)
   σ^t = 11.7x10^{-6}x45x200000 = 105 MPa
   = 0.27 σ_y or $C^t = 0.27\, C_y$
2. Poisson Effect (C^ν)
   σ^ν = 0.3 (0.8 σ_y) = 0.24 σ_y
   $C^\nu = 0.24\, C_y$
3. Downstream Condition (maximum p_i)
   σ_θ = 0.8 σ_y (for maximum p_i)
   $C^{\nu t} = (0.27 - 0.24)\, C_y = 0.03\, C_y \cong 0$
4. Upstream Condition (for minimum p_i)
   $\sigma_\theta = 0$ $p_i = 0$
   $C = 0.27\, C_y$
5. End Pressure Load (for maximum p_i)
   $P_i = A\, \sigma_\theta / 2 = 0.4\, C_y$
6. For 12-inch pipe, downstream pressure corresponds to σ_θ = 0.72 σ_y and σ_y= 52 ksi= 358 MPa. This changes the above values to those listed in the table for tests 5, 6 and 7.

2.0 MODELLING

2.1 - THE FINITE ELEMENT MODEL

2.1.1 Computer Programs and Platforms for Analysis

In the Department of Civil Engineering of the University of Alberta there are a number of computer programs that can be used for the nonlinear large displacement postbuckling finite element analysis of shells. Some of the programs available have been developed for academic research, but academic versions of commercial programs are also available. Of the latter type, ABAQUS version 5.2 (Hibbitt, Karlson & Sorensen, Inc. 1992a-c) and ANSYS version 4.4 (Swanson Analysis System, Inc. 1989a-b) for the SUN SPARCstation and ELC workstations, and for the MS-DOS platforms, respectively, are operational. The use of non commercial programs has the advantage of accessibility of the source code. In-depth knowledge of the algorithms and techniques for these programs is available to the user. On the other hand, their use in this particular study of the prediction of wrinkling behavior of line pipes would require additional development. For example, in the case of the NISA program (Stegmüller 1984; Ramm 1980), the consideration of displacement boundary conditions is necessary, and for the SYNAS program (Souza 1991,1994), the insertion of plasticity and follower forces is required. In addition, the implementation of a finite strain element would be required for each of these programs.

Among the commercial programs available in the department, ABAQUS represents a very appropriate choice because of its robustness, extensive library of elements and excellent efficiency in terms of speed, capability to pass limit points, and capacity to follow the descending branch of the load-deflection response. ABAQUS performs this latter function very smoothly and with virtually no oscillation in the solution. Another important feature that places ABAQUS in an advantageous position when compared to ANSYS is that there is no limitation of any kind with respect to the problem size that can be analyzed in terms of wave front, bandwidth, or number of equations. This is unlike ANSYS for which an additional license has to be paid as the limit of each of these parameters is increased. Both ABAQUS and ANSYS excel in the interactive graphical post processing, providing a very useful tool for the interpretation of results and making the preparation of output a simple task. Taking all of these aspects into account, ABAQUS was selected for use at this stage of the study. In addition to the ABAQUS post processor, the interactive graphical post processor POSTSYNAS (Souza 1994) was used, after being adapted in order to make it possible for ABAQUS output files to be imported. The photo-realistic renderings of the pipes were performed using Stephen Coy's Ray Tracer VIVID 386 v. 2.0 (Coy 1992) for the MS/DOS platform. The MS/DOS platform input files corresponding to the pipe's geometric modelling were exported from POSTSYNAS. The analyses were performed on a SUN SPARCstation ELC computer which has a clock rate of 33 MHz, has 24 Mbytes of RAM, and a performance of 23.7 Mips. The post processing was carried out on a SUN SPARCstation 2+, with a clock rate of 40 MHz and a performance of 35 Mips .

2.1.2 Symmetry in the Model

The pipe specimens considered in this study are those associated with the experimental program described in Sect. 1.1.3. They are made up of two cans of equal lengths which are joined by the girth-weld. Due to the symmetry of the pipe and of the load cases, only one half of the pipe is modelled. The pipe geometry and the boundary conditions at the plane of symmetry, which coincides with the plane of bending, are shown in Fig. 2.1.1. The penalty associated with the adoption of this model is that it eliminates the possibility of nonsymmetric buckling modes about the plane of symmetry (Brush 1975; Timoshenko and Gere 1961; Bushnell 1985). Therefore, it is implicitly assumed that the most representative buckling modes, i.e. those associated with lower energy states, are symmetric with respect to the bending plane. In order to assess this assumption, a model considering the full cross section was analyzed for the 20-inch unpressurized pipe, and its final buckling shape and load-displacement behavior were compared with those resulting from the half-pipe model. The results of this analysis, which is presented in Part B of the report, validate the symmetry assumption since no noticeable difference could be detected between the response of the two models. Perhaps better corroboration of this boundary condition, however, is the fact that discernible lack of symmetry in the response about the bending plane was not observed in any of the experimental specimens in either the 1992 or the 1993 test series.

2.1.3 Boundary Conditions and Loading

In the experimental test the axial loads are applied at the knife edges, and the bending moment arises from the eccentric loads applied to the loading arms, as shown in Fig. 1.1.1. To simulate the boundary conditions of the experimental test setup in the analysis, and to account for the eccentricity, the supports are modelled with the aid of geometric constraint conditions. The constraint condition may be visualized as a rigid block which connects the nodes on the pipe end to the hinge support that simulates the pivot point represented by the knife edge in the experimental test (see Fig. 2.1.1). Only the degrees of freedom corresponding to rotation about the x-axis, and the displacement in the z direction at the support where the axial load is applied, are free. The end row of elements on each pipe end, that forms an 'end ring', are restricted to elastic behavior. The elastic rings are included in the model in order to avoid plastic response due to stress concentration in the neighborhood of the supports. These end rings are the regions where the loads are applied and the rotation increments are prescribed, and constraints at these locations exist against ovalization and Poisson's ratio expansion.

Consequently, the end rings are regions where it is possible to trigger early plastification and local buckling unless some precautions are taken, as described above. In addition, on each end of the pipe a closure cap is introduced. This permits the axial force from the internal pressure to be modelled as a follower force normal to the end surface.

The axial load, P, delivered by the testing machine is applied at the (one) pivot point which is free to move longitudinally. The moments at the pipe ends are applied through the prescription of displacement boundary conditions (rotations) at the pivot points, where rotation increments are prescribed during the incremental analysis. In this case the moments associated with a given increment, or the conjugate flux (Hibbitt, Karlson & Sorensen, Inc. 1992a), are reactive (unknown) forces that are determined after the system of nonlinear equations is solved for displacements and rotations. The incremental analysis using this approach produces a much smoother load-deflection curve than one for which eccentric forces or moments are applied at the supports, as was the case for the results of local buckling of pipes presented by Zhou and Murray (B1993a), and by Hu (1991).

2.1.4. Mesh Considerations for the Girth Weld

The finite element modelling of the girth-welded pipes incorporates the girth-weld at mid-length through a row of elements whose longitudinal dimension is set approximately equal to the pipe thickness. This is done in order to facilitate the modelling of the changes in properties for the weld metal and of the base metal in the neighborhood of the weld due to the welding process. The girth-weld elements are all located on the same can and introduce a lack of symmetry in the longitudinal direction. In Part B some comparisons are presented involving several discretizations in order to evaluate the influence of the method of mesh discretization on the predicted analytical results. Some consideration of longitudinal and circumferential symmetries are also examined there.

In order to model the girth weld properly and to avoid high aspect ratios and excessively elongated elements, a mesh which is refined in the central region of the pipe was adopted. The refined region is graduated longitudinally such that the longitudinal element dimension changes with each row of elements and the mesh becomes finer towards the girth-weld row of elements. The finite element mesh used in Part A of this study was selected from a series of different meshes which were tested for their capacity to adequately model the girth-welded pipe both in terms of moment curvature behavior and in terms of their capacity to predict the buckling mode shape for all load cases considered in the experimental tests.

The finite element mesh adopted throughout Part A is shown in Fig 2.1.2. The mesh contains 1440 quadrilateral finite strain S4RF elements, 36 triangular STRI3 elements, 36 rigid constraint elements, and 1535 nodal points. The total number of degrees of freedom is equal to 8883. The academic version of ABAQUS available in the Department of Civil Engineering at U of A lacks an interactive graphical preprocessor. The input data preparation is done in an alternative manner through an input file containing keywords corresponding to commands for the generation of rows of nodes and elements, as well as for the definition of other attributes such as boundary conditions or material properties.

2.1.5 Element Selection

ABAQUS's four-node, doubly curved, reduced integration, finite membrane strain S4RF shell element was adopted to model the pipe. The element has six degrees of freedom per nodal point (three displacements and three rotations). The formulation of this element takes into account the thickness change, transverse shear constraints, and in-plane and rotational hourglass control (Hibbitt, Karlson & Sorensen, Inc. 1992a-b). The choice of this element is due to the high strain levels that occur after the initiation of buckling in the regions of the pipe located in the neighborhood of the wrinkle. The strains and rotations for this element can be arbitrarily large. The default number of integration points through the thickness is five, which is considered appropriate for simple nonlinear problems. However, seven integration points were used for all analyzes. The stress and strain fields from the analyses of the pipe segments in this study, corresponding to their final load step, are presented in Section 3. The adequacy of this finite element model is discussed in Part B, where other elements were also used in the comparison with the experimental results for some load cases.

The three-node facet (STRI3) shell elements were used to model the caps. One of the nodal points is common to all of the elements in a cap and is located on the pipe axis on the cross section that coincides with the end of the pipe. The remaining nodal points are located on the pipe ends, and are common to the rings. The STRI3 element has six degrees of freedom per node (three displacements and three rotations) and transverse shear deformation is not included in its formulation.

2.1.6 Other Modelling Details

The geometric constraint elements that are used to simulate the experimental end conditions are introduced in the model as part of the definition of boundary conditions which, in ABAQUS, correspond to boundaries of the type 'multi-point constraint' (MPC) using BEAM elements (Hibbitt, Karlson & Sorensen, Inc. 1992b). These elements are rigid and are all subjected to the same rotation as prescribed for the supports at the pivot points.

On the boundary between the coarse region of the mesh and the refined region there are circumferential rows of incompatible elements, where the number of longitudinal rows are doubled from 18 rows in the coarse region to 36 rows in the refined region, as illustrated in Fig. 2.1.2(b). A QUADRATIC MPC (Hibbitt, Karlson & Sorensen, Inc.

1992c) was used to enforce continuity along the sides of the incompatible elements located on the transition boundary. The quantities associated with the degrees of freedom related to the corresponding nodal points are interpolated from the nodes adjacent to the coarse region by using quadratic interpolation. As an example, in Fig. 2.1.3 the degrees of freedom of the nodal points **a**,**b**,**c** are used in the interpolation for nodal point $\mathbf{p}_1$.

In the visualization of stress and strain fields the finite element local coordinate system is used. The local *1*-direction is determined by the projection of the global x-axis onto the surface. If the angle between the global x-axis and the normal is less than 0.1 degrees, then the local *1*-direction is set equal to the projection of the z-axis onto the surface. The local *3*-direction coincides with the direction of the positive normal to the surface at the point. Finally, the local *2*-direction is at right angles to the local *1* and *2*-directions so that the three axes form a right-handed triad (Hibbitt, Karlson & Sorensen, Inc. 1992b).

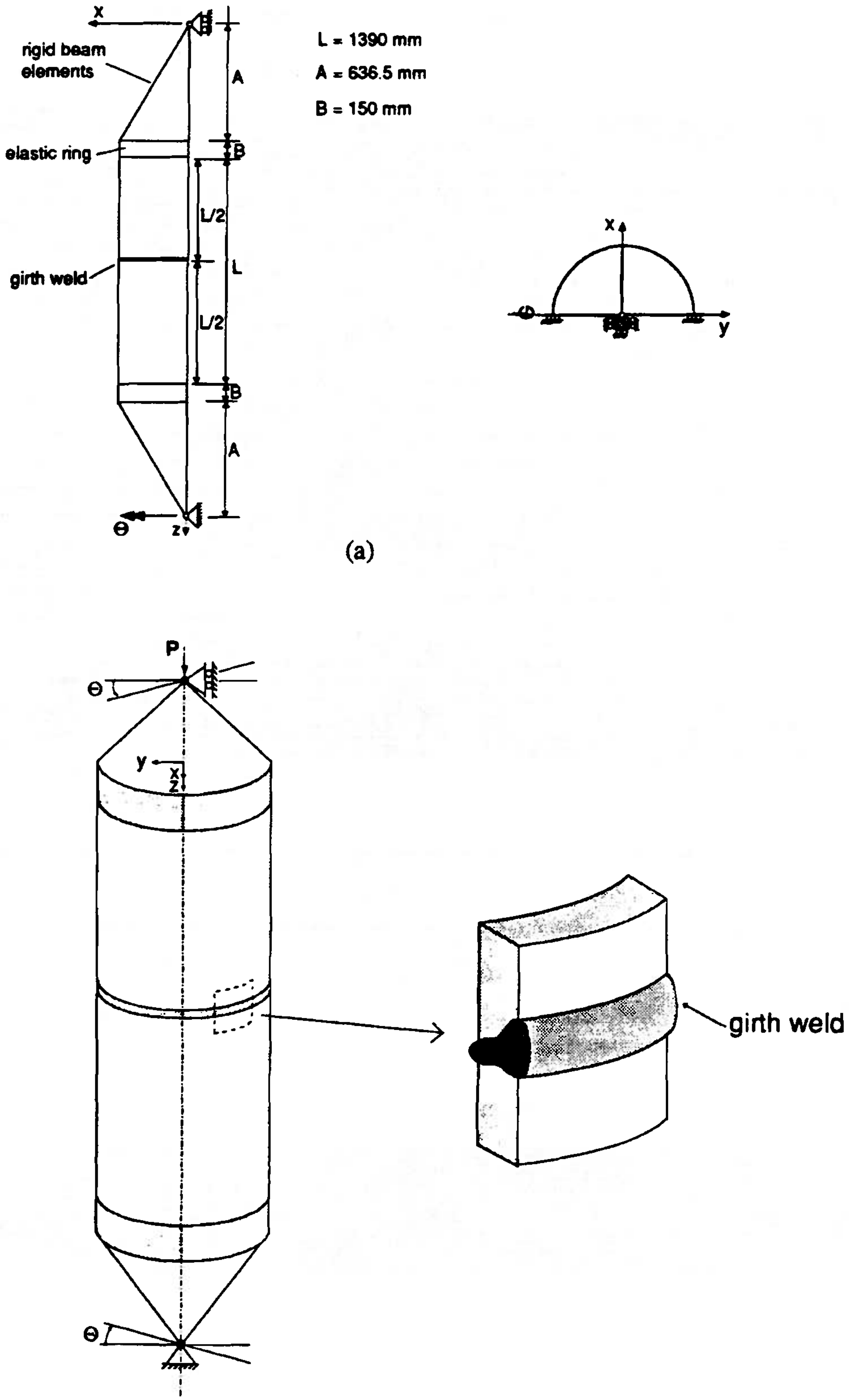

(a)

(b)

Figure 2.1.1. Pipe geometry, boundary conditions and geometric constraints of the model.

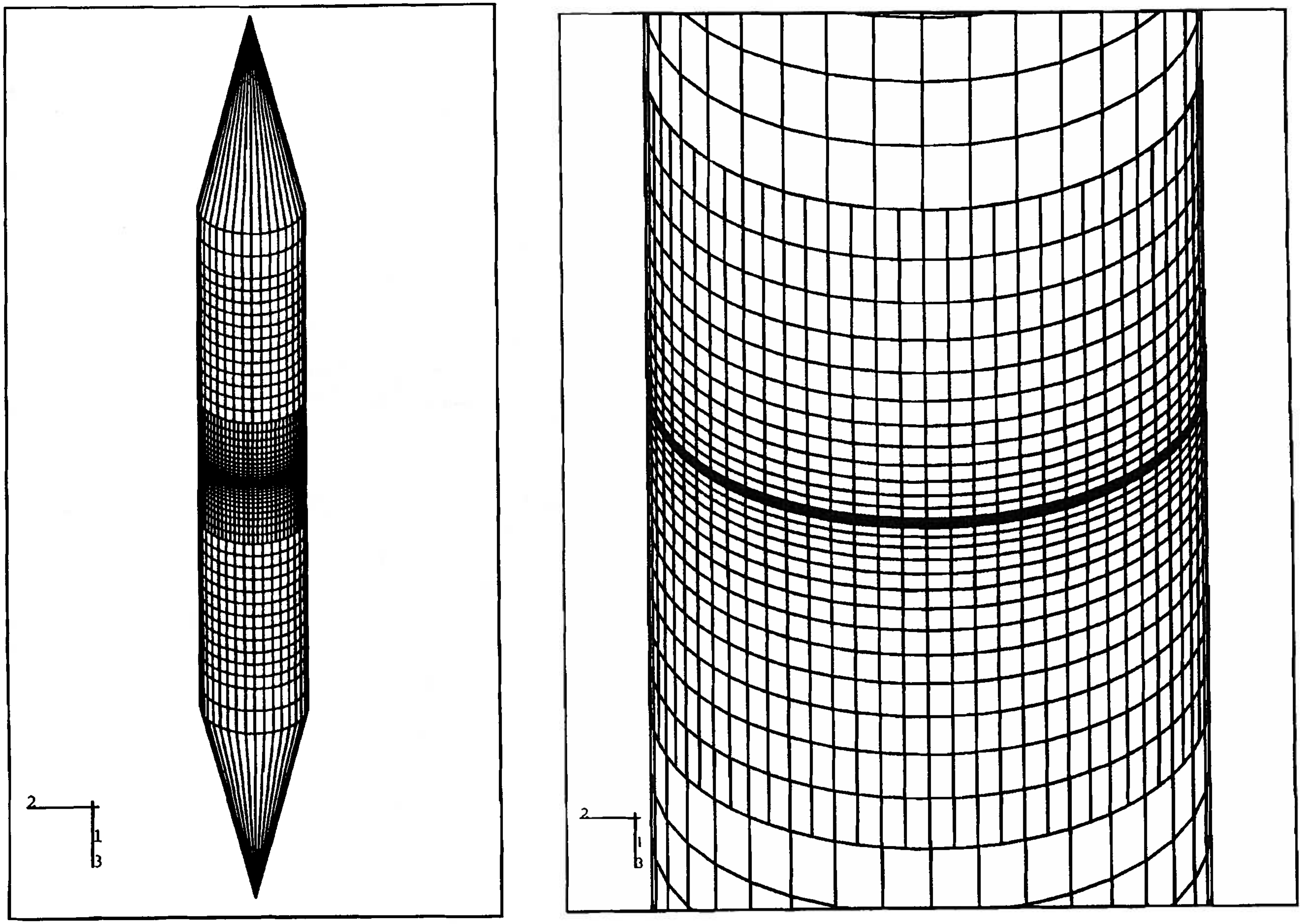

(a) Finite-strain finite element mesh and rigid beam elements.

(b) Refinement region and girth-weld elements.

Figure 2.1.2. Finite-strain finite element mesh for the girth-welded pipes.

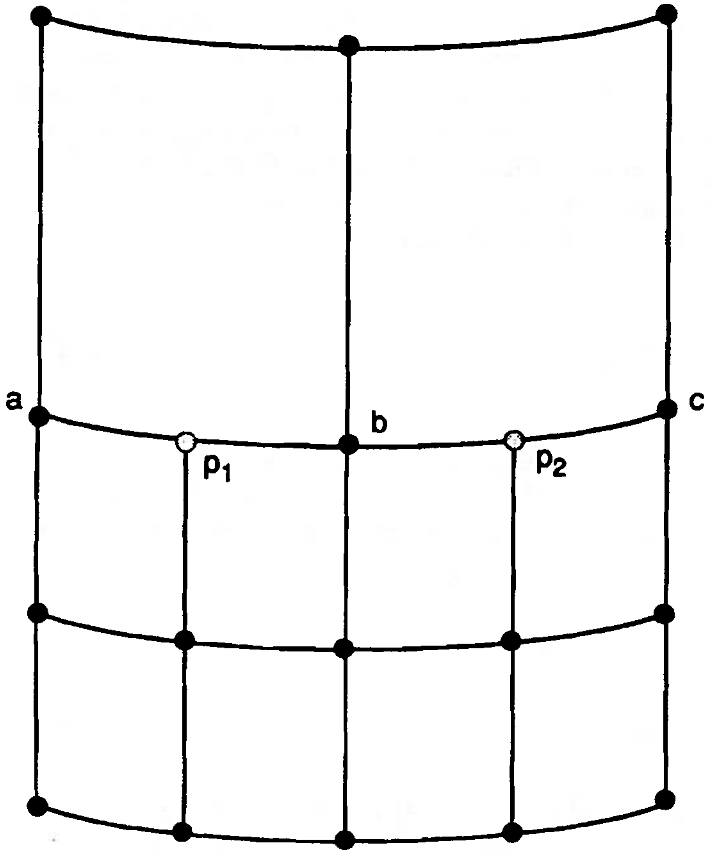

Figure 2.1.3. Example of quadratic multi-point constraint at nodal points of incompatible elements.

2.2 - MATERIAL PROPERTIES

In the formulation of the finite strain element, it is assumed that the material to be modelled is capable of exhibiting large inelastic strains (ductile behavior). In ABAQUS the stress-strain relationships are to be supplied as a function of the plastic strain. In the definition of the material properties of finite strain elements in ABAQUS, the relation between true (Cauchy) stress (force per current area) and the logarithmic plastic strain must be supplied (Hibbitt, Karlson & Sorensen, Inc. 1992a), whereas for the other element types the nominal stress - nominal strain relationships are used instead. The logarithmic strain is defined by:

$$\varepsilon_{\ln} = \int \frac{dl}{l} = \ln(\frac{l}{l_0}) \qquad (2.2.1)$$

The material properties for the pipes used in the experimental tests were determined by the tension tests conducted by Mohareb , *et al,* (B1993, B1994). The nominal stress-strain data obtained from this test can be converted to true stress and logarithmic plastic strain according to (Hibbitt, Karlson & Sorensen, Inc. 1992a):

$$\sigma_{true} = \sigma_{nom}(1+\varepsilon_{nom}) \qquad (2.2.2)$$

$$\varepsilon_{\ln} = \ln(1+\varepsilon_{nom}) \qquad (2.2.3)$$

The true stress - logarithmic strain values adopted in this study are presented in Tables 2.2.1 and 2.2.2. In Fig. 2.2.1 the true stress vs. logarithmic strain curve and the nominal stress vs. nominal strain curve are shown.

The material properties for the girth weld and the neighboring region at mid-length of the model to take into account the dependence on the temperature due to the welding process were taken from the experimental tests performed at the Centre for Frontier Engineering Research (C-Fer), for the Algoma Steel Corporation's MN-80 casing (Marion 1989). These properties are presented in Table 2.2.3 and plotted in Fig. 2.2.2 as functions of the temperature, in which a bilinear stress-strain curve is assumed. Although the material is not the same, in the absence of temperature-dependent experimental data for the pipe and girth weld, these properties were used to produce residual stresses by the scheme for thermal modelling presented in Sec. 2.3.

Table 2.2.1 - Material Properties for the 12-inch pipe

True Stress in MPa	Logarithmic Strain
203.5	0.0
328.7	0.385×10^{-3}
373.2	0.117×10^{-2}
383.0	0.212×10^{-2}
392.0	0.308×10^{-2}
404.7	0.799×10^{-2}
417.1	1.783×10^{-2}
434.5	3.724×10^{-2}
449.0	5.629×10^{-2}
461.8	7.501×10^{-2}
519.0	1.805×10^{-1}

E = 203500 MPa
$\nu = 0.264$
$\alpha = 1.2\times10^{-5}/^{\circ}C$

Table 2.2.2 - Material Properties for the 20-inch pipe

True Stress in MPa	Logarithmic Strain
203.5	0.0
329.3	0.200×10^{-2}
373.9	0.300×10^{-2}
383.7	0.399×10^{-2}
392.8	0.499×10^{-2}
405.5	0.995×10^{-2}
417.9	0.198×10^{-1}
435.1	0.392×10^{-1}
449.2	0.583×10^{-1}
461.5	0.770×10^{-1}
512.4	1.800×10^{-1}

E = 203500 MPa
$\nu = 0.26$
$\alpha = 1.2\times10^{-5}/^{\circ}C$

Table 2.2.3 - Temperature-dependent Properties for the girth-weld

(a) Elastic Range

E in MPa	Temperature
206000	0.0
206000	21.0
203300	93.0
196000	204.0
184000	316.0
164000	427.0

$\nu = 0.30$

$\alpha = 1.2 \times 10^{-5}/^{\circ}C$

(b) Plastic Range

Nominal Stress in MPa	Plastic Strain	Temperature in ° C
622.0	0.0	0.0
627.0	0.500×10^{-2}	0.0
609.8	0.0	21.0
620.0	0.500×10^{-2}	21.0
567.7	0.0	93.0
595.0	0.500×10^{-2}	93.0
487.0	0.0	204.0
550.0	0.500×10^{-2}	204.0
377.3	0.0	316.0
510.0	0.500×10^{-2}	316.0
303.2	0.0	427.0
445.0	0.500×10^{-2}	427.0

$\nu = 0.30$

$\alpha = 1.2 \times 10^{-5}/^{\circ}C$

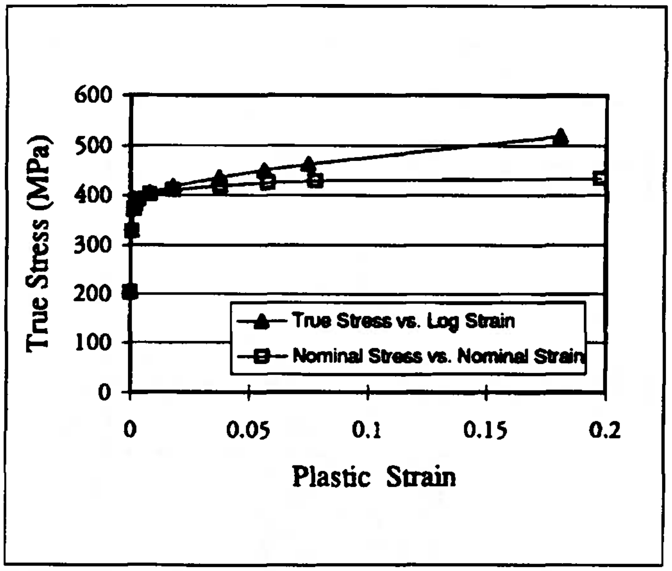

(a) 12-inch pipes

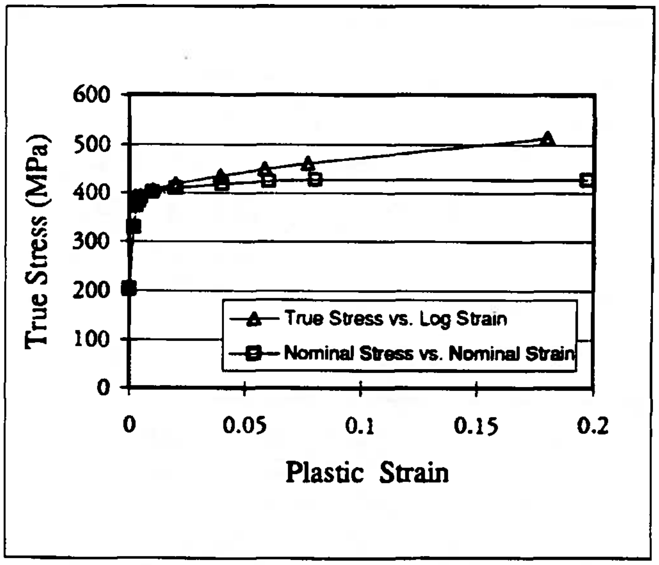

(b) 20-inch pipes

Figure 2.2.1. Material Properties

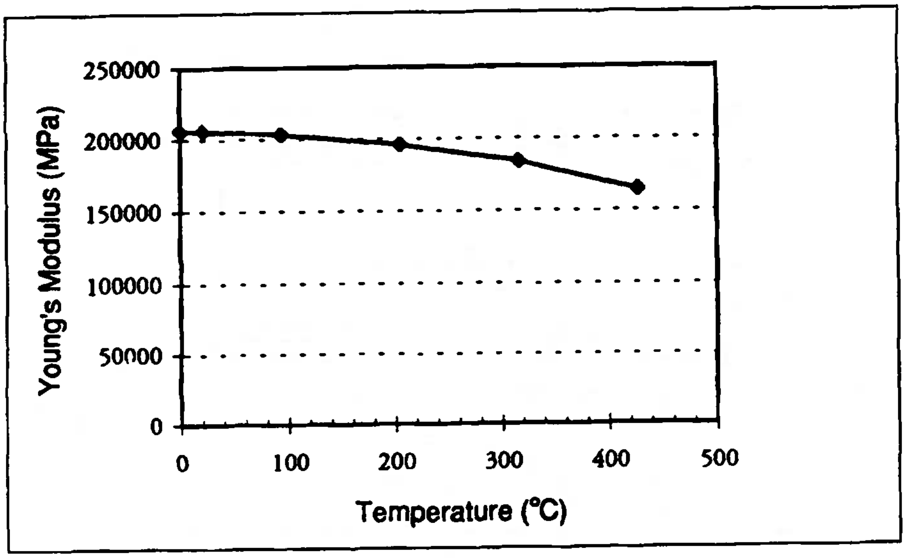

(a) Effect of temperature on moduli at zero strain

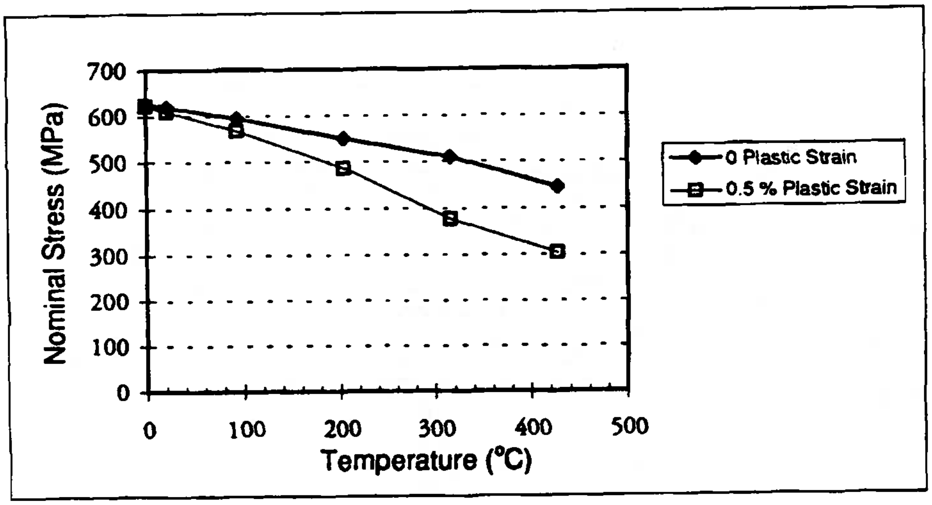

(b) Effect of temperature on stress at selected strain values

Figure 2.2.2 - Temperature-dependent Properties for the girth-weld

2.3 - THERMAL MODELLING

The simulation of weld residual stresses and deformations adopted in this study follows a procedure adopted by Hu (1991) for the investigation of the compressive behavior of fabricated steel tubes. The welding residual stresses are generated through a thermal cycle, while the pipe geometry remains nearly unchanged. The temperature increments are applied as one-step loads. The resulting residual stresses are not greatly altered when the temperature increments are applied in steps. The procedure used is illustrated in Fig. 2.3.1, which consists of the following steps:

1) Generate the finite element mesh for the half-pipe including the out-of-roundness and mismatch-type imperfections in the original geometry (see Sect. 2.4), denoted by $\underline{X}_0$.

2) Increase the reference temperature and produce reversal residual stresses. The temperature increment for this effect was set equal to +300 degrees Celsius, the same adopted in Hu's procedure. This temperature increment is applied only to the nodal points on the girth-weld elements (i.e.- the shaded elements in Fig. 2.1.2b). The boundary conditions adopted are such that the pipe is allowed to move longitudinally, but the pipe ends are prevented from moving transversally. An ABAQUS run is performed for this load case and the displacements at the nodal points, denoted by $\underline{d}$, are stored. The displacement field introduced by the temperature is shown in Fig. 2.3.1(a) using a magnification factor equal to 1000.

3) The deformed geometry, denoted by $\underline{X}$, is determined by superimposing the nodal displacements determined in step 2 on the original geometry, i.e., $\underline{X} = \underline{X}_0 + \underline{d}$. A new stress-free model is generated in this shape to incorporate the deformation due to the temperature increase. But no residual stresses are present at this stage.
A new uniform reference temperature is set at this stage.

4) The referenced temperature is decreased by applying -300 degrees Celsius to the imperfect geometry generated in step 3. As the deformation produced in the previous step was incorporated into the original geometry, the current load step is the initial step of the incremental analysis to follow, and the one which will produce the residual stresses. This temperature reduction is applied only to the nodal points on the girth-weld elements. In this step all the nodal points

contain the deformed geometry, i.e., the components of $\underline{\mathbf{X}}$, are supplied in the ABAQUS input file and no automatic generation of nodal points is performed. In Fig. 2.3.1(b) the corresponding displacement field is shown, using a magnification factor equal to 1000. The results after the load step is applied correspond to a pipe with residual stresses of the order of 50% of the yield stress and whose imperfections are approximately the same as those produced in step 1 for the imperfect model. That is, the welding cycle produces little residual displacement relative to the initial geometry. The norm of the difference between the geometry at this step and the initial geometry is no larger than 0.173 mm, or 0.046 % of the diameter, for the pipes tested.

5) The model now incorporates the residual stresses. In Fig. 2.3.1(c) the displacement field is shown after the thermal cycle, using a magnification factor equal to 5000. As one can notice, the imperfections produced are very small. The circumferential residual stress (S11) and the longitudinal residual stress (S22) are shown in Figs. 2.3.2 and 2.3.3, respectively. The analysis can now proceed by applying the axial load, pressure and the prescribed rotation increments to the imperfect model obtained by the above procedure.

In order to simulate field welding, the thickness of the girth-weld elements was considered to be two times the pipe thickness. The material properties for the weld, taken from actual temperature-dependent stress-strain curves, were presented in the Sect. 2.2.3

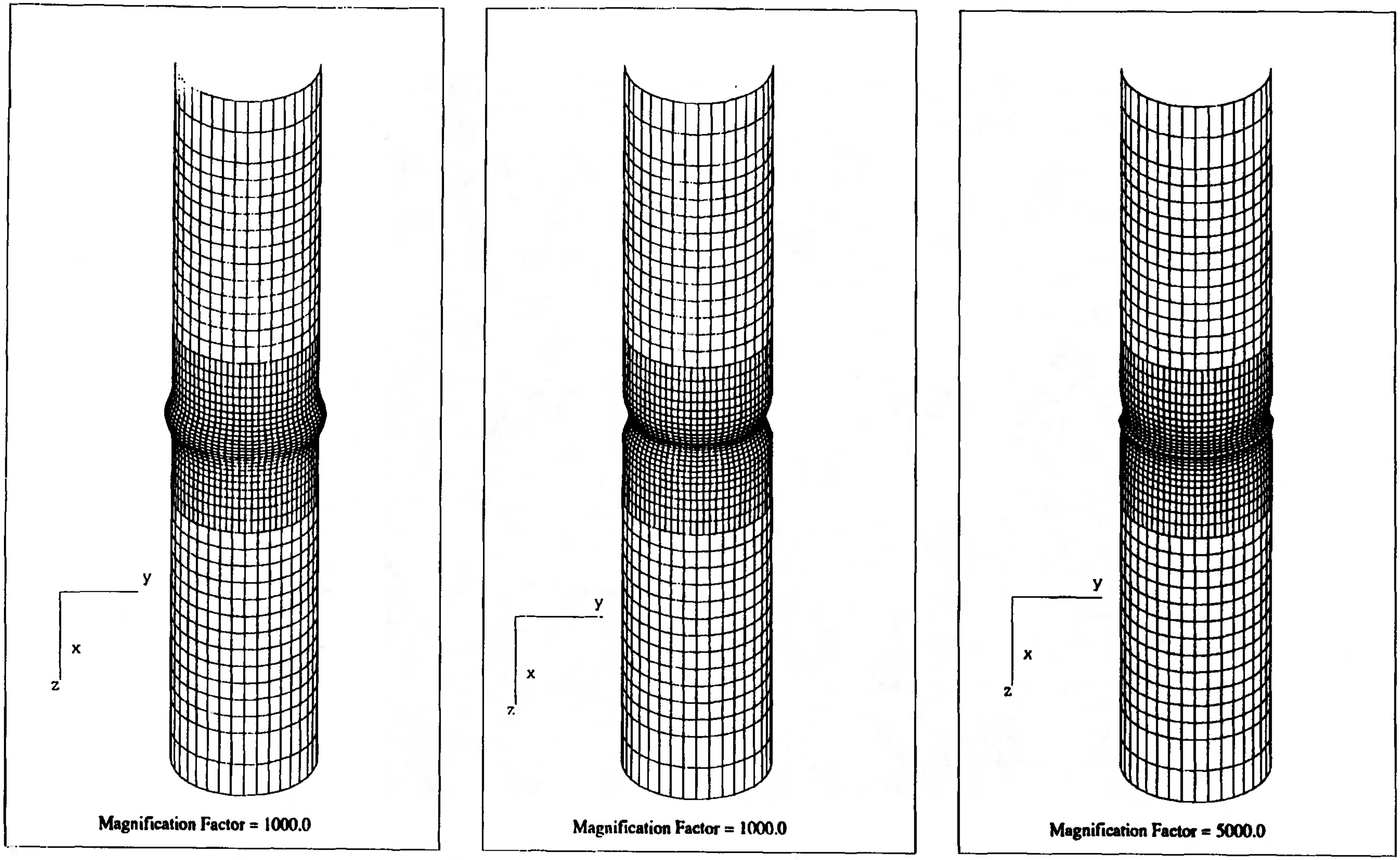

(a) (b) (c)

Figure 2.3.1. Simulation of weld residual stresses and deformations through a thermal cycle. (a) Reference Temperature is increased by 300 degrees Celsius. (b) Reference temperature is decreased by 300 degrees Celsius. (c) Imperfect geometry incorporating the residual stresses.

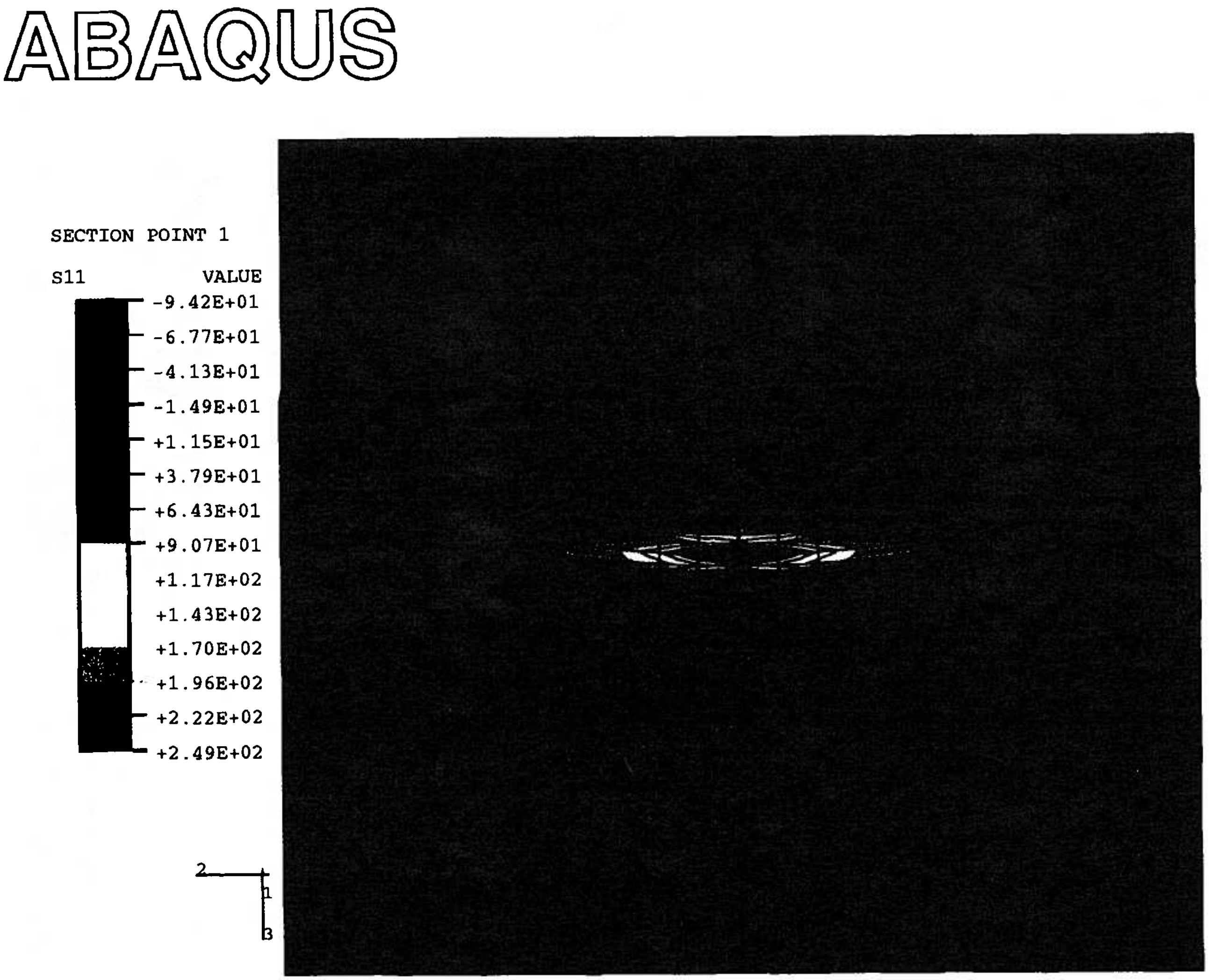

Figure 2.3.2. Circumferential Residual Stress (S11) at Section Point S1 for specimen UGA20WEF3.

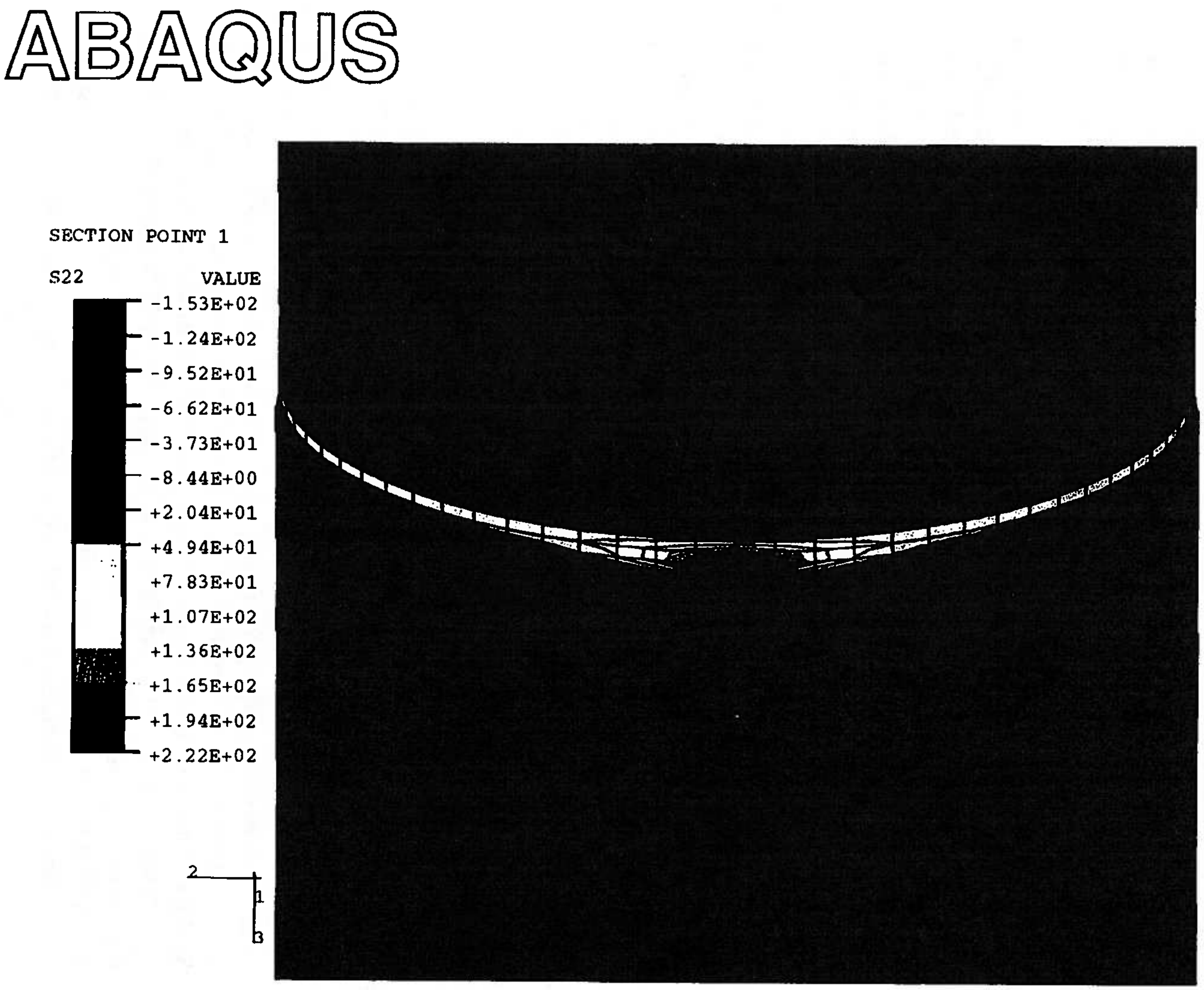

Figure 2.3.3. Longitudinal Residual Stress (S22) at Section Point S1 for specimen UGA20WEF3.

2.4 - INITIAL IMPERFECTIONS, MISALIGNMENTS AND SPECIMEN IDENTIFICATION SYSTEM

The types of imperfections related to girth-welded pipes may be considered to be: (i) out of straightness, (ii) out of roundness, and (iii) mismatch. The tolerance limits for fabricated cylinders are established by API specification for fabricated structural steel pipe (API 1977). In this study only the out of roundness and mismatch are considered. The out of straightness imperfection is not considered to be relevant for the problem of local buckling of pipes with combined axial load and bending because the rotations prescribed at the pipe supports produce an effect similar to eccentricity of the axial load. The out of roundness and mismatch, on the other hand, are shown in Part B to be important aspects of the model in order to predict a buckling shape that agrees with the results of experimental tests, particularly for the unpressurized pipe. The imperfections introduce some lack of symmetry about the normal plane at mid-length of the model and, therefore, tend to prevent the formation of symmetric buckling modes about this plane. However, such symmetric modes have not been observed in full-scale experimental testing of line pipe specimens at the U of A.

The mismatch imperfections at the girth weld considered in the analyses are illustrated in Fig. 2.4.1. The mismatch imperfections are considered to be of two types: (i) elliptical out-of roundness of the cross-sections (Fig. 2.4.1(a)), or (ii) lateral off-set of the two cans (Fig. 2.4.1(b)). The magnitudes of the lack of fit at the weld, used in this investigation, are given in Table 2.4.1. There is little justification for these numerical values other than a judgment by the authors that they are reasonable and the evidence that the numerical solutions using them display characteristics consistent with the experimental observations. Some insight into the importance of these effects is contained in the solutions in Part B.

Since there are many different variations that can be built into the finite element model, and the results for each model may be different, it is necessary to specify the model in an unambiguous manner before comparisons can be made between different analyses and before judgments can be made as to the effect of variations in modelling on the predicted behavior. Therefore, Table 2.4.2 introduces an identification system that will be used throughout this study to identify the girth-welded pipe models for which results are presented. Each model is identified by a string code of the type XGAnnWIMN. This notation is an extension of the identification system presented in Sect. 1.1.3. Therefore, although the definition of each character is contained in Table 2.4.2, the reader is already familiar with the codification associated with the interpretation of the first 6 characters of the code, and may concentrate, at this stage, only on the symbology associated with the last three characters as specified in the table.

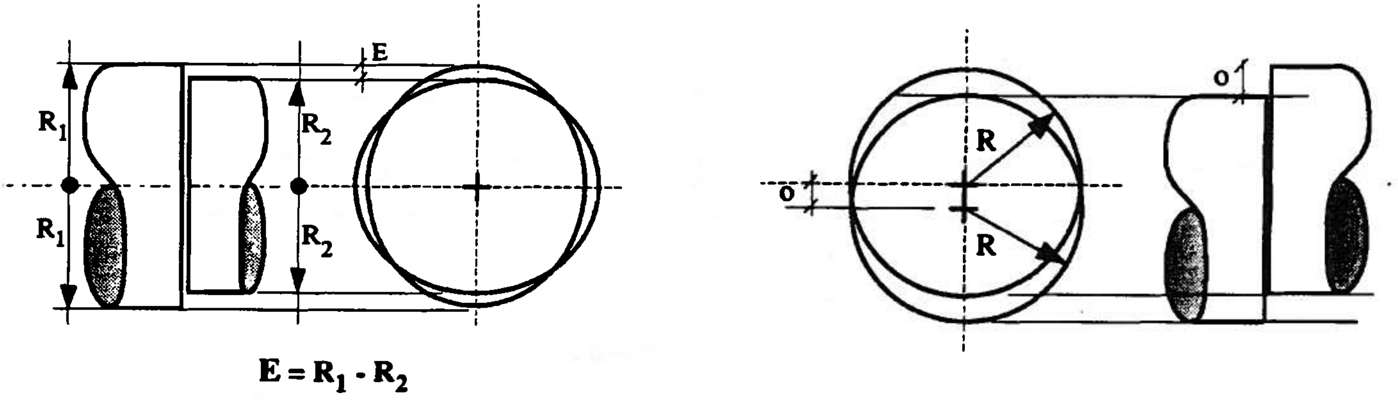

(a) Elliptical out of roundness

(b) Lateral offset

Figure 2.4.1. Mismatch imperfections at the girth-weld section

Table 2.4.1 - Magnitude of lack of fit at the weld for the specimens tested

Pipe Diameter	Misalignment Type	
	Elliptical out of roundness (E)	Lateral offset (O)
12 inches	1 mm (XGA12WEMN)	1 mm (XGA12WOMN)
20 inches	2 mm (XGA20WEMN)	2 mm (XGA20WOMN)

Table 2.4.2 - Finite Element Mesh/Load Case Designations

FINITE ELEMENT MESH DESIGNATIONS - XGAnnWIMN		
X		*Pipe location (load case):*
	U	Upstream (empty)
	D	Downstream (fully pressurized)
	H	Halfway between upstream and downstream referred to the location of the pipe relative to the pumping station.
G	*Greatest thermal effect*	
A	*Active axial force (or constant force)*	
nn	12 or 20	*Nominal diameter of the pipe in inches*
W	*Denotes girth-welded pipe*	
I		*Imperfection of the section along the girth weld:*
	P	Perfect
	E	Elliptical out-of-roundness
	O	Offset mismatch
M		*Mesh Type Group:*
	U	Uniform mesh using 9-node elements with equal number of rows along the longitudinal and circumferential directions
	R	Refined mesh in the central region of the pipe in both directions using 9-node elements
	F	Finite strain 4-node elements using a refined mesh in the central region of the pipe in both directions
	Q	Refined mesh in the central region of the pipe in both directions using 4-node Quadrilateral elements
N		*Number to identify the mesh pattern within the mesh type group* (See, for example, Fig. 6.1.1 in Part B).

2.5 - INCREMENTAL ANALYSIS

2.5.1 Iteration and Convergence

The nonlinear finite element analyses carried out, herein, involve plasticity and buckling. They were carried out using the built-in automatic incremental solution strategy available in ABAQUS. ABAQUS uses Newton's method for solving the nonlinear equilibrium equations (Hibbitt, Karlson & Sorensen, Inc. 1992a). The nonlinear solution is approximated by a series of increments within each load step, with iteration to reach equilibrium within each increment. An automatic incrementation scheme is used so that the increment size is adjusted based on the convergence characteristics.

In a nonlinear post-buckling analysis the load-displacement response of the structure often exhibits a negative stiffness beyond the limit point or a bifurcation point (See Sect. 2.6). The default incremental scheme used in ABAQUS is based on a displacement control method which is capable of providing a solution corresponding to an increase in displacements even when the reactive forces decrease. In cases where displacement control cannot be used successfully, the modified Riks method (Riks 1979), that is also available in ABAQUS, can be selected by the user. All the results presented in this report were obtained using the ABAQUS default control parameters associated with the algorithm for the solution of the equilibrium equations of the nonlinear systems. The convergence of Newton's method is measured by comparing the maximum force residuals and the incremental displacements with their specified tolerances following each iteration. The default convergence tolerance for nonlinear problems is equal to 5×10^{-3} for residual forces and moments. The default value for the convergence criterion for the ratio of the largest displacement correction to the largest corresponding incremental solution value is 10^{-2}.

2.5.2 Incremental Solution Procedure

An incremental analysis in ABAQUS is performed for a given number of steps as set by the user. Each step is subdivided into increments, and a limit of 20 increments for each step was set for all cases. The initial increment size was set to be equal to 30% of the step size for all cases. The size of the remaining increments are adjusted by the automatic algorithm based on the convergence criteria throughout the incremental analysis. For each additional increment after the first increment of a step, the solution to the increment is estimated by ABAQUS by extrapolating the solution from the previous increment. This is accomplished by setting the parameter MONOTONIC=YES in the *STEP option.

For all mesh/load case combinations, the residual stresses are firstly introduced in the model, as explained in Section 2.3. The temperature loads are applied using the *TEMPERATURE option to the girth-weld elements as a single step/increment in the analysis. This is the first load step. For all load cases the axial load is applied in the second load step of the incremental analysis. This load, which is defined as a concentrated load, is applied to the support which is free to move along the z-direction (see Fig. 2.1.1) using the *CLOAD option in a single step/increment. Simultaneously with the axial load, for the mesh/load cases of the type **HGAnnWIMN** and **DGAnnWIMN**, the internal pressure is applied using *DLOAD option. In Table 2.5.1 the magnitudes of the loads used in the analyses are shown. The basis for these loads can be found in Sect. 1 in association with Tables 1.1 and 1.2.

The end bending moments arise in the model as reactive forces resulting from the prescription of rotations as boundary conditions at the pivot points. The incremental rotations at the supports are applied throughout the analysis in equal increments of 0.002 radians for each step using the *BOUNDARY option. The rotation increments are kept constant during each step, by setting AMPLITUDE=CONSTANT. The parameter TYPE=VELOCITY is set to give a velocity history, allowing the definition of the rotation in terms of angular velocity instead of total rotations. The advantage of this approach is that large prescribed rotations and/or general rotations can be prescribed to a 3-D model. In this case the rotation increments are determined as the average of the velocities at the beginning and at the end of each increment, multiplied by the time increment, which in static analysis is simply the size of the increment relative to the size of the step.

Table 2.5.1

Values of Constant Loads for Analytical Specimens

Pipe Diameter	Mesh/Load type	Axial Load	Pressure
12 inches	HGA12WIMN	0.644 kN.m	10.45 MPa
12 inches	DGA12WIMN	0.644 kN.m	10.45 MPa
20 inches	HGA20WIMN	1.303 kN.m	9.79 MPa
20 inches	DGA20WIMN	1.303 kN.m	9.79 MPa

2.6 - SOME ASPECTS OF SHELL ANALYSIS

In order to interpret the results of the analyses to follow it is useful to have some exposure to the characteristics of shell buckling behavior. For readers unfamiliar with this subject, a brief review of some of the relevant aspects of shell behavior is given in this Section.

The buckling behavior of shells, involving instability when passing a critical point, can be grouped into two categories (Brush and Almroth 1975; Bushnell 1985; Singer 1980; Souza 1991):

1.- loss of stability associated with equilibrium bifurcation; and
2.- loss of stability due to limit points.

In Fig. 2.6.1 these types of collapse are illustrated. Point A corresponds to a bifurcation point in which the equilibrium path is not uniquely defined. The branch OA of the equilibrium path prior to the buckling, referred to as the primary path, is usually considered as linear in the analytical formulations, where the bifurcation point is predicted by solving a linear eigenproblem. The eigenvalues in this case are proportional to the critical load and the eigenvectors are related to the buckling modes. In the definition of eigenproblems, the pre-buckling displacements may or may not be taken into account, according to their importance for the prediction of the buckling load.

The post-buckling equilibrium path, referred to as the secondary path, can be ascending (AC branch in Fig. 2.6.1.a), or descending (AC branch in Fig. 2.6.1.b). In the first case the bifurcation is stable. If the secondary path is descending the bifurcation is unstable. Although equilibrium bifurcation occurs only for perfect structures, the knowledge of the shape of the secondary path is of great importance in the assessment of the influence of initial imperfections on the structural behavior. Structures whose equilibrium paths are similar to the one shown in Fig. 2.6.1a are capable of reaching loads higher than the load corresponding to the bifurcation point, i.e., the critical load. In this sense, the occurrence of a bifurcation point does not produce structural collapse. Structures showing this type of behavior are considered imperfection-insensitive, and the initial imperfections do not cause a significant change in their behavior.

Imperfect structures whose secondary paths are descending, as shown in Fig. 2.6.1b, are not capable of reaching loads higher than the critical load (unless the secondary path becomes ascending for greater values of displacements and reverts to a stable equilibrium state at this time). Structures of this type for which the secondary path descends rapidly are imperfection-sensitive. Their maximum load capacity is associated with a limit point. For this type of structure, initial imperfections may substantially alter their behavior. The imperfection sensitivity is believed to be responsible for the widely scattered results from experimental tests (Singer 1980; Arbosz 1982; Elishakoff 1983). Because random initial imperfections are introduced into each specimen by the manufacturing process, and the load capacity is unfavorably affected by the initial imperfection, the experimental tests of such structures may show a different behavior for each test.

Limit points are not restricted to structures with initial imperfections. Other types of structures which have similar behavior are spherical shells and cylindrical shells loaded transversely. For cylindrical shells it is also possible that a bifurcation point associated with a buckling mode may occur beyond a limit point, in the presence of which the shell may change its deformed configuration from one buckling mode to another during the unloading branch of the load-displacement curve.

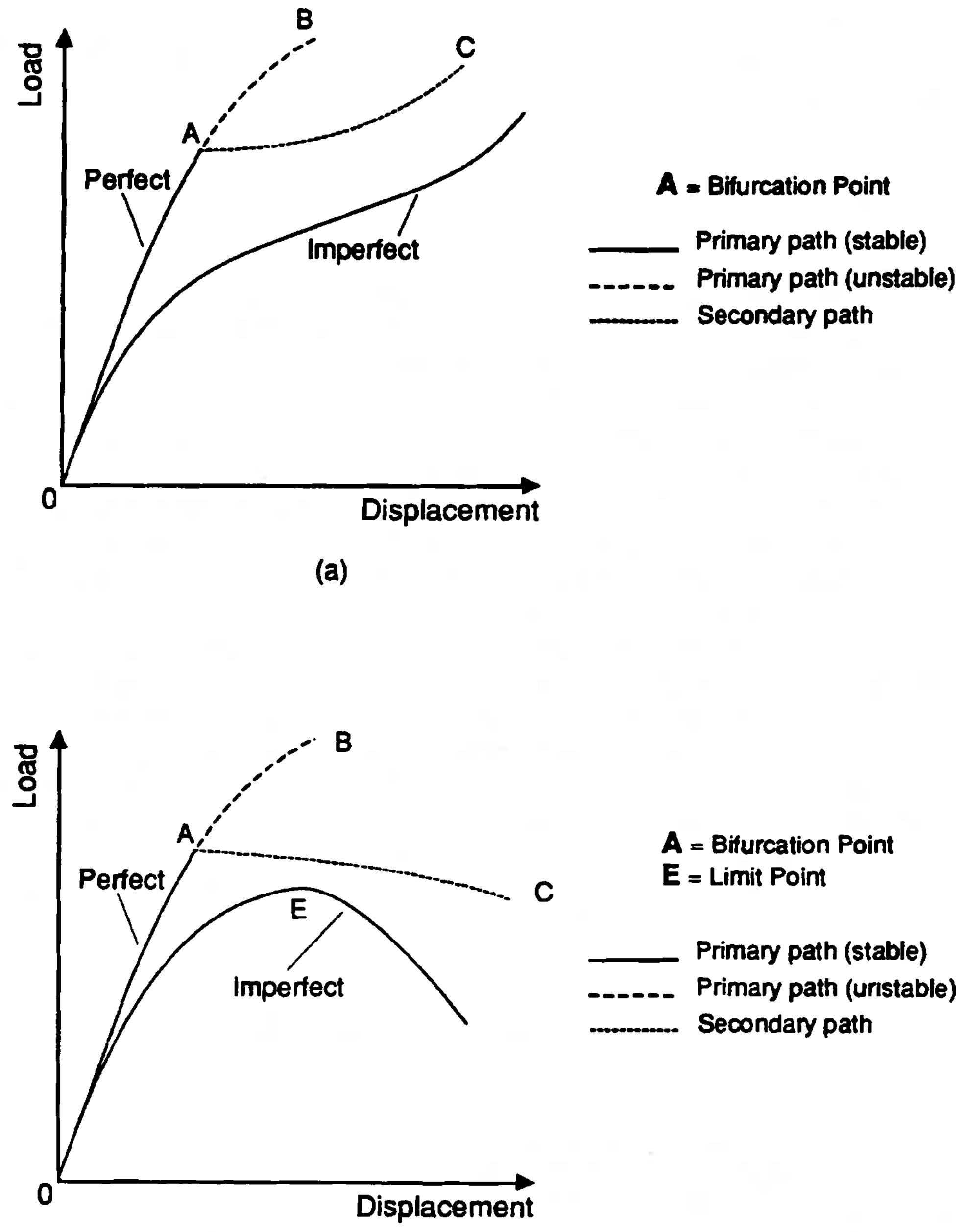

(a)

(b)

Figure 2.6.1. Equilibrium paths for perfect and imperfect structures exhibiting: **(a)** stable post-buckling behavior, and **(b)** unstable post-buckling behavior.

3.0 ANALYTICAL SOLUTIONS AND COMPARISONS WITH TEST RESULTS

3.1 - INTRODUCTION

The loading sequence adopted in the analytical solutions coincides with that of the loading history in the experimental tests, assuming that the initial configuration is that obtained through the temperature cycle described in Sect. 2.3. This temperature cycle is intended to simulate the initial imperfections and residual stresses arising from the girth - weld welding process. The magnitudes of the axial loads and internal pressures adopted in the analytical solutions are presented in Table 3.1. These are consistent with those in Table 1.2. Initially the axial load is applied at one of the pivot points as a single-increment step for all pipes and load case combinations. For the pressurized pipes (specimens HGA12WEF3, HGA20WEF3, DGA12WEF3, DGA20WEF3) the pressure is applied in the second step. In order to simulate the follower forces associated with the internal pressures a cap was included on each pipe end. Because of the depth of the loading arms, and the fact that rotation occurs about the knife edges, the test set-up introduces an additional eccentricity between the vertical load and the pipe centerline at the end plates which connect to the pipe ends. In the analytical solutions the rotations are imposed at each pivot point, after the axial load and pressure have been applied. The moment and lateral (shear) force at the pivot points are reactive forces which are determined from the support reactions arising from the analysis.

Table 3.1. Applied loads.

Specimen	Axial Load	Internal Pressure	D/t
UGA12WEF3	322.0 kN	0	50
HGA12WEF3	399.0 kN	5.21 MPa	
DGA12WEF3	486.5 kN	10.45 MPa	
UGA20WEF3	651.5 kN	0	63
HGA20WEF3	850.0 kN	4.87 MPa	
DGA20WEF3	972.0 kN	9.74 MPa	

In order for the experimental results and the analytical results to be comparable, the moments were calculated at the ends of the pipe. The additional eccentricity due to the rotation of the loading lever arms at the end plate locations was taken into account. In the analytical solution this eccentricity was simulated by the rigid body motion constraints produced through the rigid beam elements which connect the pipe to the supports.

The rotations were imposed at each pivot point in increments of 0.02 radians per analysis step. The analysis step is, in turn, subdivided throughout the incremental analysis into three to four analysis increments. The number of increments is automatically adjusted by ABAQUS to control the convergence rate. The number of iterations per increment ranged from 2 to 11 throughout the loading history. The average execution time on the Sun ELC SPARCstation was equal to approximately 4 minutes 30 seconds for the solution of each analysis increment.

The analytical results for each of the pipes studied are described using four types of graphs and figures, as described below.

1) A plot of moment vs. average curvature between the ends of the pipe is given. (See, for example, Fig. 3.2.1.) Both the moment and the curvature vary along the pipe length because of the influence of the variation in eccentricity, as well as the plasticity and local buckling. In particular, the curvature varies substantially in the neighborhood of the local buckling (wrinkle). However, a fixed gauge length must be defined in order for values from different specimens to be comparable. In this study the average curvature ($K = \theta / L$) is adopted, in which θ is the relative rotation between the two ends of the specimens over the pipe length. The bending moment was determined as the average of the bending moments at the two end plates of the specimens.

   In the moment vs. curvature curve corresponding to the test, a point called the softening point (SP) is defined (subjectively) as that point where significant softening is initiated. Generally, this point is indicative of the initiation of wrinkling. This point will be used, in addition to the ultimate resisting moment and the corresponding average curvature, as a reference value for the comparison between the analytical and the experimental results. In the case of the pressurized pipes, in which the softening point is not well defined as the wrinkling process develops, the analytical SP will be defined as the point located beyond the limit point and at which the moment is 5% lower than the analytical ultimate resisting moment (i.e.- limit moment) for the particular pipe.

2) Plots of the deformed configuration of the specimen for a number of selected values of the curvature are shown. This enables the visualization of the evolution of the

deformed shape. (See, for example, Fig. 3.2.2.) Each deformed configuration is keyed to a point on the moment vs. curvature curve described above, in 1.

3) A photo-realistic rendered image which shows the final deformed configuration in the region of the local buckle, or wrinkle, is compared to a photograph of the test specimen taken at the end of the test. (See, for example, Fig. 3.2.3.)

4) The distributions of circumferential and longitudinal strain corresponding to the final step of the analysis over the outside surface of the pipe are presented. (See, for example, Fig. 3.2.4 and 3.2.5.) For one specimen only, namely UGA12WEF3, the stress and strain distributions along the circumferential and the longitudinal directions both for the inside and the outside surface are also given. Figure 3.1.1 defines the local coordinate system and the integration points through the thickness in order that the reader may identify the orientation of the stress and strain components and their locations.

In the following Sections 3.2 to 3.7 the presentation of results described above is given for each of the specimens of the 1993 Test Series, in turn, as identified in Table 1.2, beginning with the 12 inch specimens.

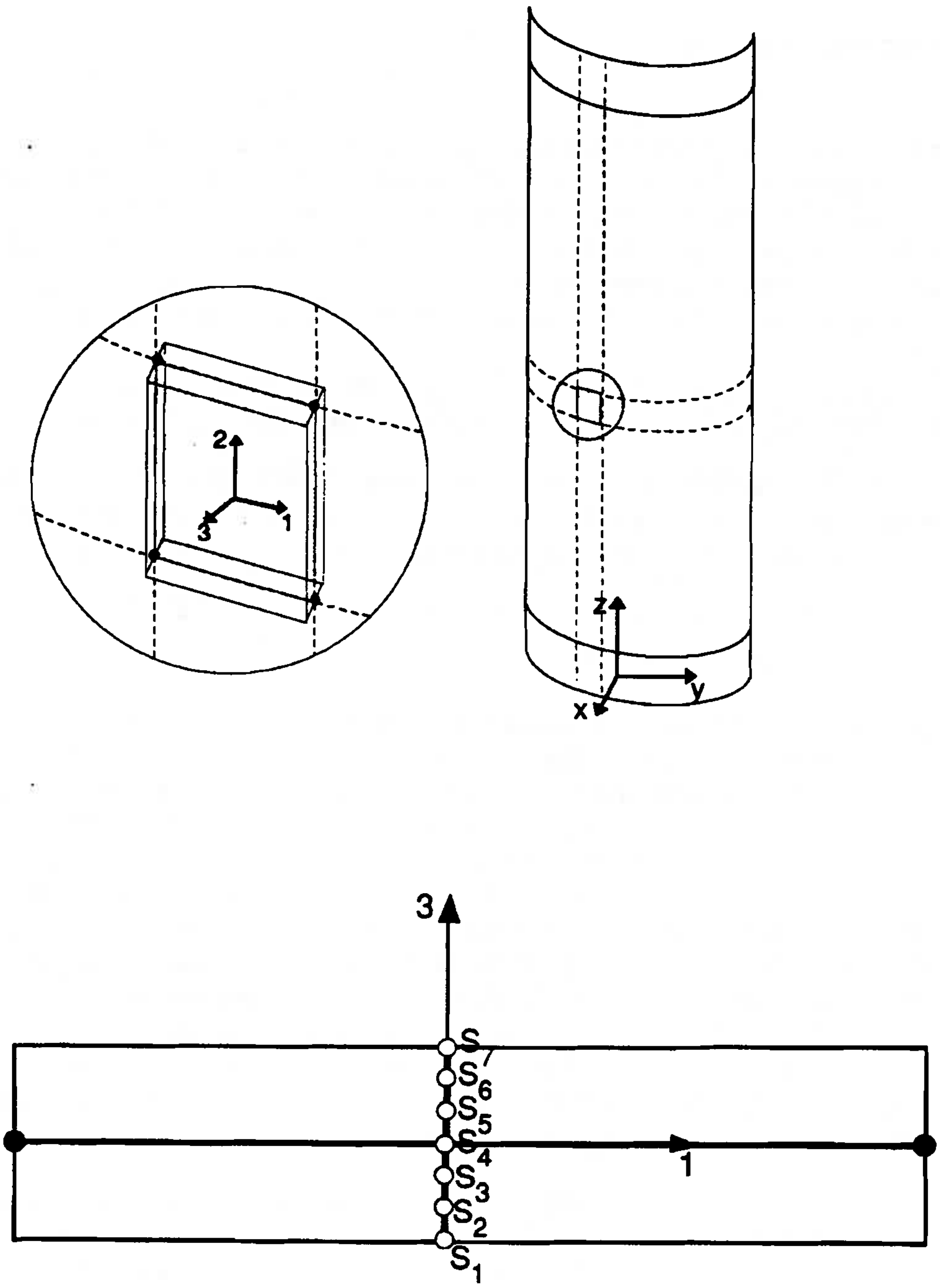

Figure 3.1.1. S4RF element local coordinate system 1,2,3 and Section Points S1,..,S7 (Gauss Points) throughout the element thickness for the representation of stresses and strains.

3.2 - SPECIMEN UGA12W

The results for the unpressurized 12-inch pipe subjected to axial load and imposed moments (imposed rotations in the analytical solution) are presented in this section. The analytical results corresponding to Specimen UGA12WEF3 (recall that the system of identifying specimen size, loading, and modelling parameters from the specimen designation was explained in association with Table 2.4.1) are compared with the ones obtained from the test by Yoosef-Ghodsi, *et al*, (B1994b) defined in Table 1.2.

In Fig. 3.2.1 the average end moment vs. average curvature curve is shown both from the test and the analytical solution. The analytical ultimate resisting moment (or limit moment), which is equal to $M_{lim} = 191$ kN. m, is 9.1% lower than the experimental ultimate resisting moment. The softening point for the analytical solution is determined by inspection to be at the limit point since significant softening begins immediately thereafter. This point occurs for an average curvature of $K_{lim} = 37.9 \times 10^{-6} mm^{-1}$ which is 25% greater than the value obtained from the test.

The evolution of the deformed configuration shown in Fig. 3.2.2 suggests that the structure undergoes a transition from one buckling mode to another along the descending (softening) branch of the moment vs. curvature curve. The configurations in Fig. 3.2.2 are keyed to the analytical curve in Fig. 3.2.1 so that each configuration in Fig. 3.2.2 may be related to its corresponding point on the moment vs. curvature curve. At point A of the moment vs. curvature curve, corresponding to $K/K_{lim}=1.06$, two bulges are developing approximately symmetrically about the middle of the pipe. From Point B ($K/K_{lim}=1.44$) to Point C ($K/K_{lim}=1.75$) the top bulge tends to disappear and the deformed configuration evolves to a one-bulge buckling deformation. At point D ($K/K_{lim}=1.87$) an inward buckle is developing and, simultaneously, the bulge is decreasing. From Point D to the end of the moment vs. curvature curve, corresponding to $K/K_{lim}=2.5$, the diamond-shape pattern develops while no increase of deformation is observed in the rest of the specimen.

In Fig. 3.2.3(a) the photo-realistic computer rendering of the final buckling configuration for one-half of the pipe is shown. The reflections in the rendering have been included because they provide some assistance in visualizing the shape of the surface. This configuration corresponds to the point F on the moment vs. curvature curve. In Figure 3.2.3(b), a photograph of the test specimen taken after the test is shown. Comparison of these two pictures indicates there is a good correspondence in the deformation patterns arising in the test and the analytical simulation. For both specimens there is an alternate inward-outward deformation along the circumferential direction in the neighborhood of the girth weld. The diamond pattern straddles the weld in the experimental specimen while it is to one side of the weld in the analytical solution.

Figures 3.2.4(a) and (b), and 3.2.5(a) and (b), show the stress distribution in the circumferential (S11) and the longitudinal (S22) directions, respectively, both for the inside surface (section point S1 through the thickness) and the outside surface (section point S7 through the thickness). The definition of the local coordinate system and the Gauss point locations are shown in Fig. 3.1.1. The stresses in the region where the wrinkle occurs reach values much greater than the yield stress which for the 12-inch specimens is equal to 358 MPa. These stresses are mostly due to the bending associated with the change of curvature of the pipe wall in the immediate neighborhood of the wrinkle in the specimen.

Figures 3.2.6 and 3.2.7 show the strain distribution in the circumferential (E11) and the longitudinal (E22) directions, respectively, both for the inside surface (section point S1 through the thickness) and the outside surface (section point S7 through the thickness). The circumferential (compressive) strain (E11) is nearly constant over the surface remote from the buckle, reaching values of 0.71% on the inside surface and 1.41% on the outside surface along the compression side of the pipe. In the neighborhood of the wrinkle the circumferential (tensile) strain reaches values of 12.4 % on the inside surface and 12.9% on the outside surface. The longitudinal (tensile) strain (E22) is also nearly constant over the surface remote from the buckle, reaching values of 4.02 % on the inside surface and 0.01 % on the outside surface along the compression side. In the neighborhood of the wrinkle the longitudinal strain reaches values ranging from -41.4 % (compression) to 24.2% (tension) on the inside surface, and values ranging from -41.0 % (compression) to 7.48% (tension) on the outside surface.

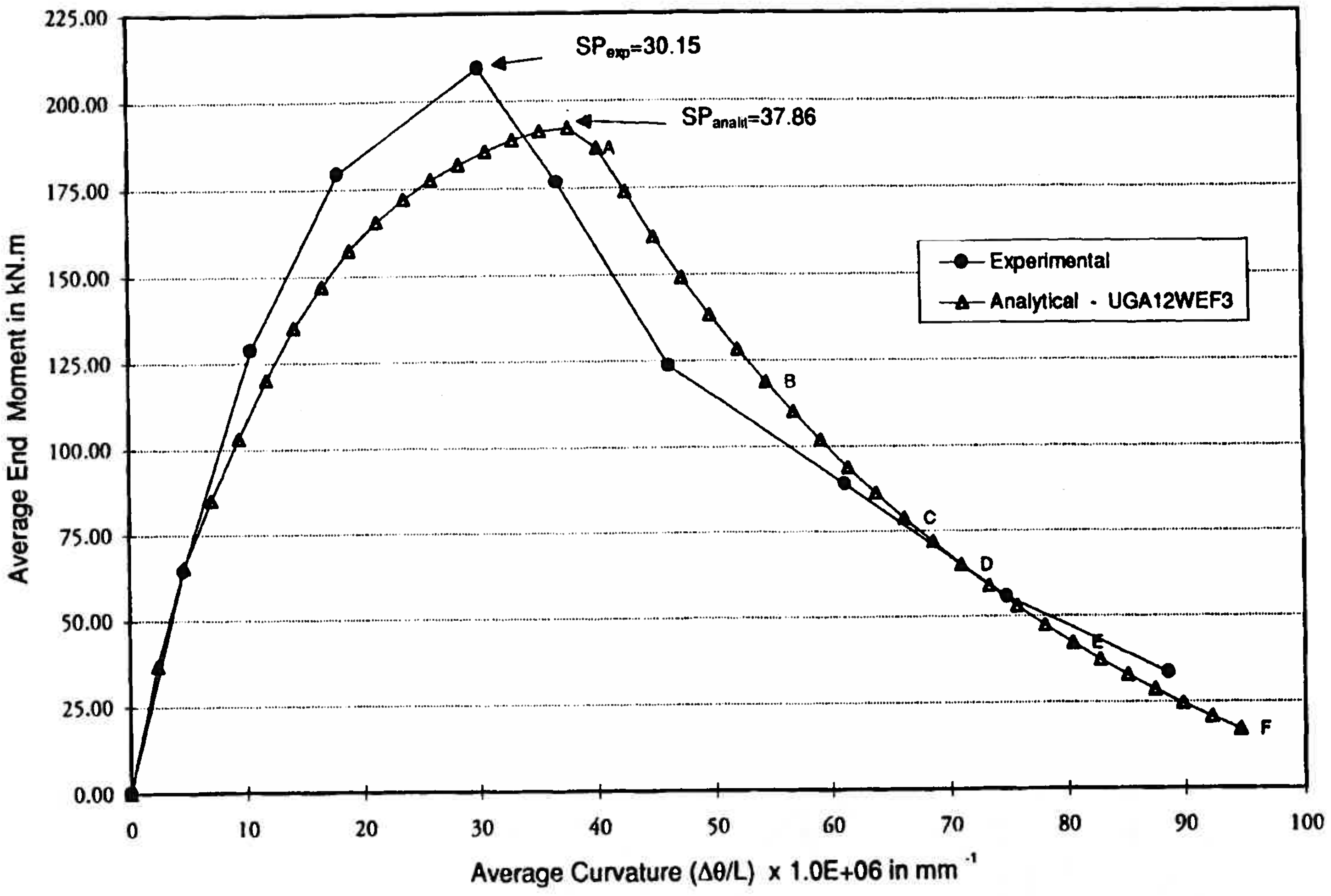

Figure 3.2.1. Average End Moment vs. Curvature for UGA12W Pipe

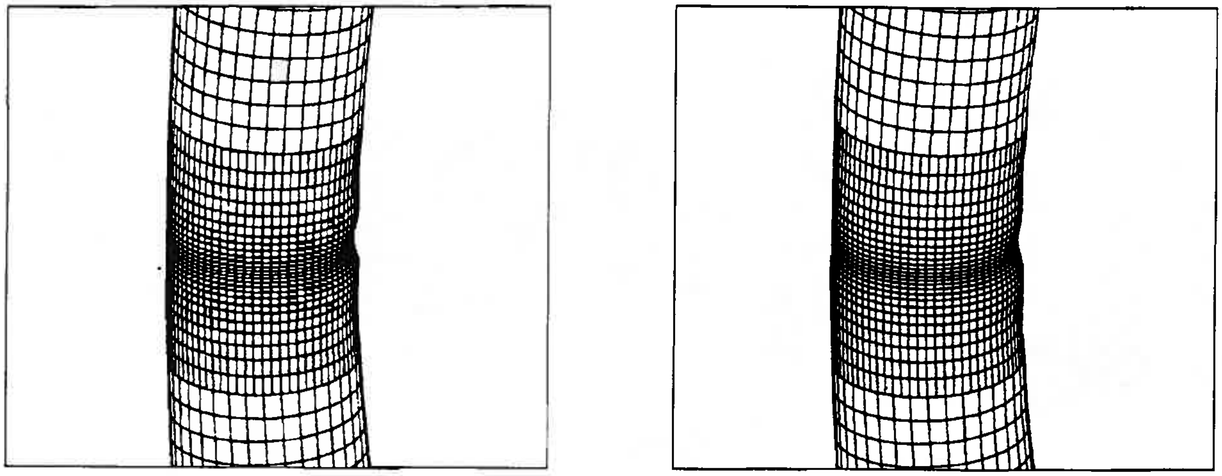

(a) Point A. K = 40.2E-06 /mm. Magnification Factor = 4.0.

(b) Point B. K = 54.4E-06 /mm. Magnification Factor = 1.0.

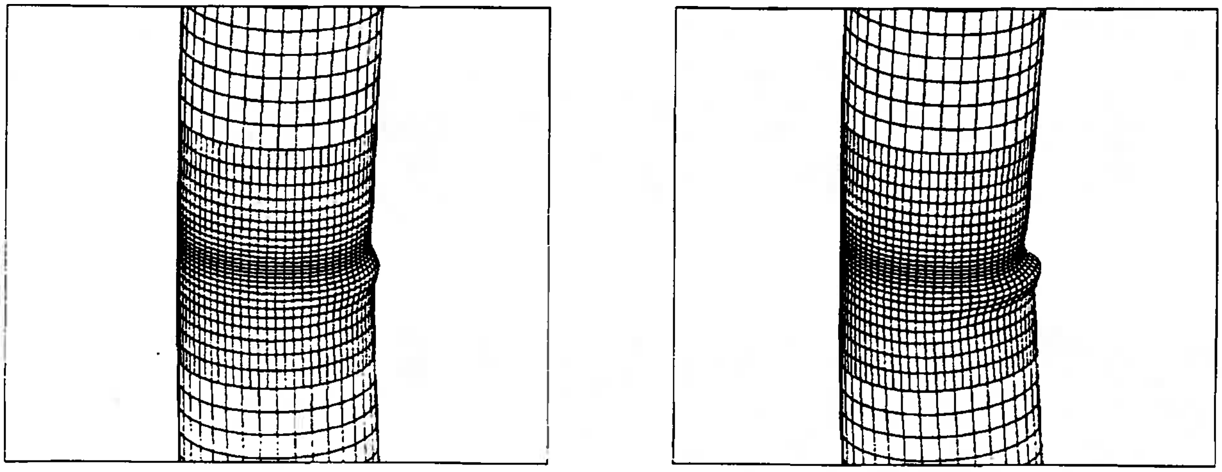

(c) Point C. K = 66.2E-06 /mm. Magnification Factor = 1.0.

(d) Point D. K = 70.9E-06 /mm. Magnification Factor = 1.0.

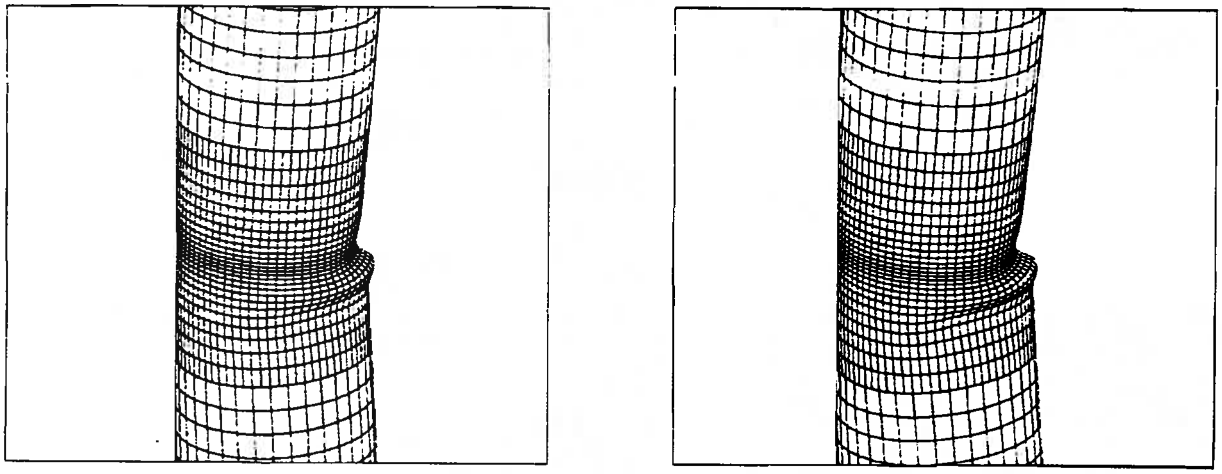

(e) Point E. K = 80.4E-06 /mm. Magnification Factor = 1.0.

(f) Point F. K = 94.5E-06 /mm. Magnification Factor = 1.0.

Figure 3.2.2. Evolution of buckling shape along the end moment vs. curvature (K) curve for specimen UGA12WEF3.

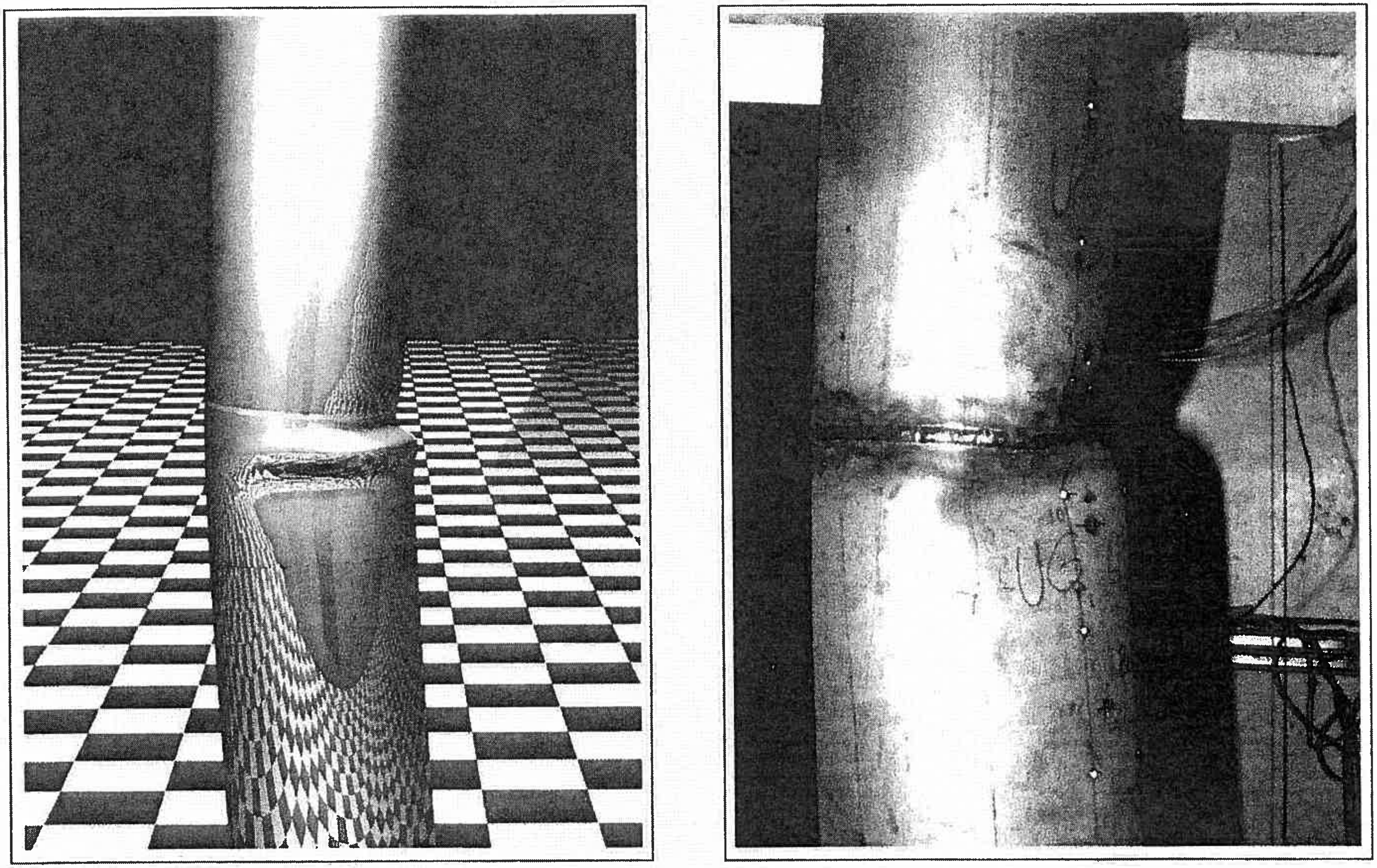

(a) Analytical Results for UGA12WEF3

(b) Experimental Test

Figure 3.2.3. Final Buckling Configuration for UGA12W pipe.

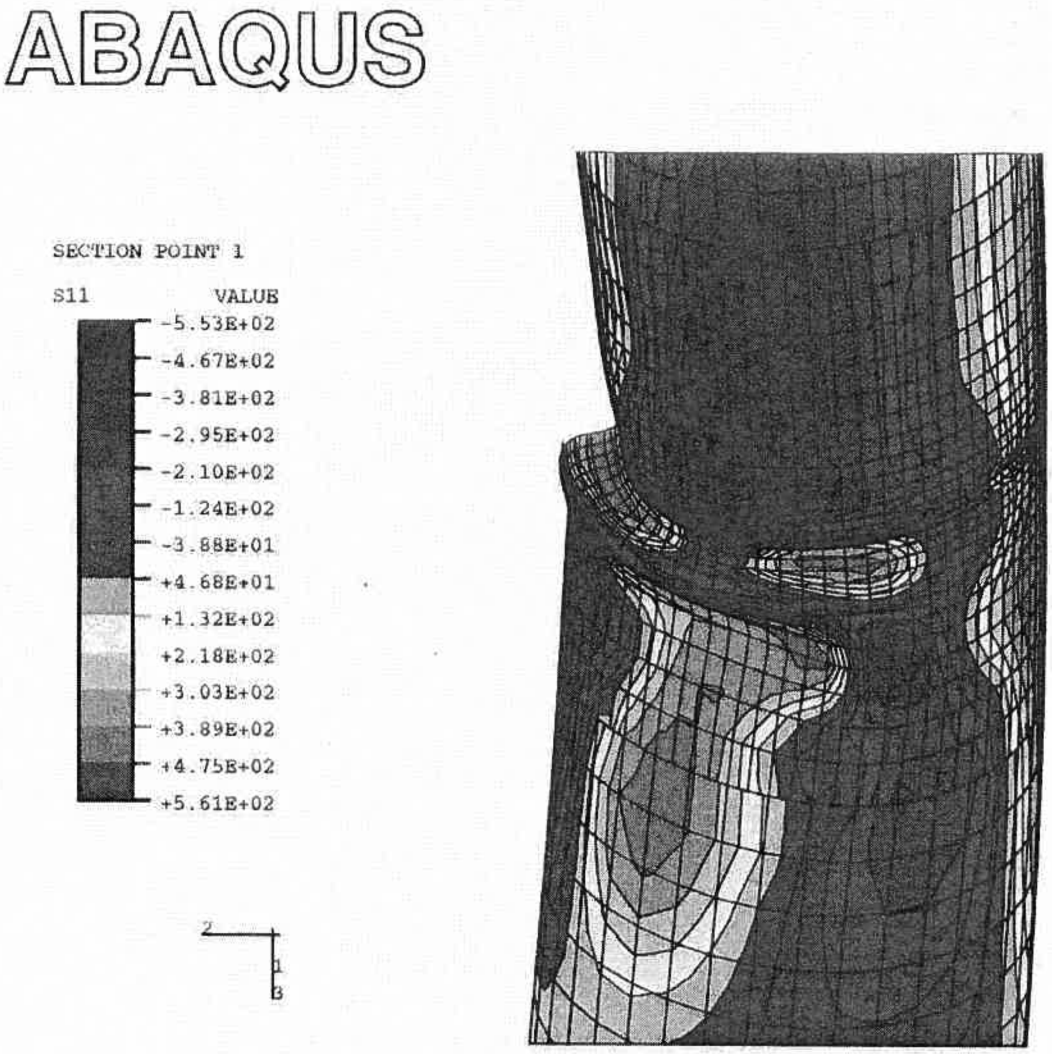

Figure 3.2.4(a). Circumferential Stress (S11) at Section Point S1 for specimen UGA12WEF3.

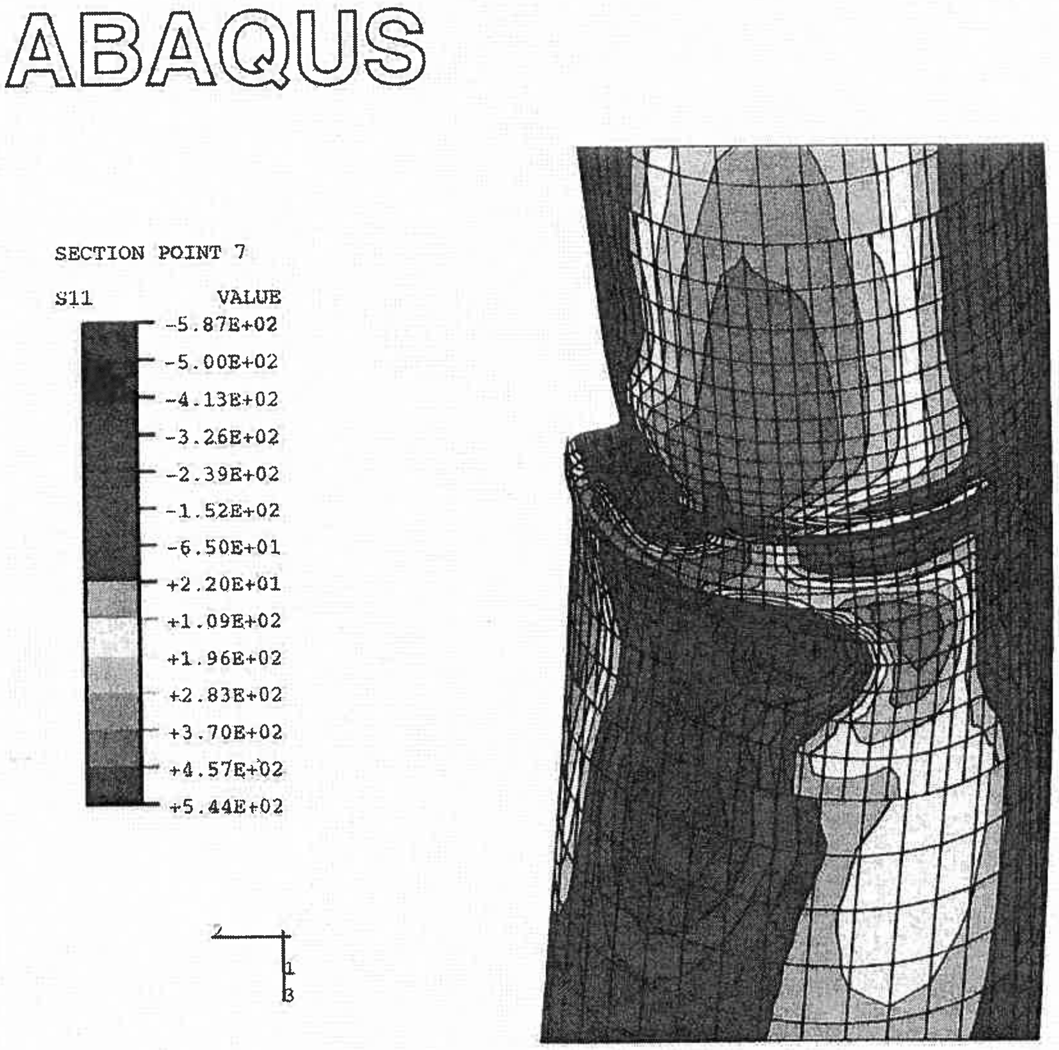

Figure 3.2.4(b). Circumferential Stress (S11) at Section Point S7 for specimen UGA12WEF3.

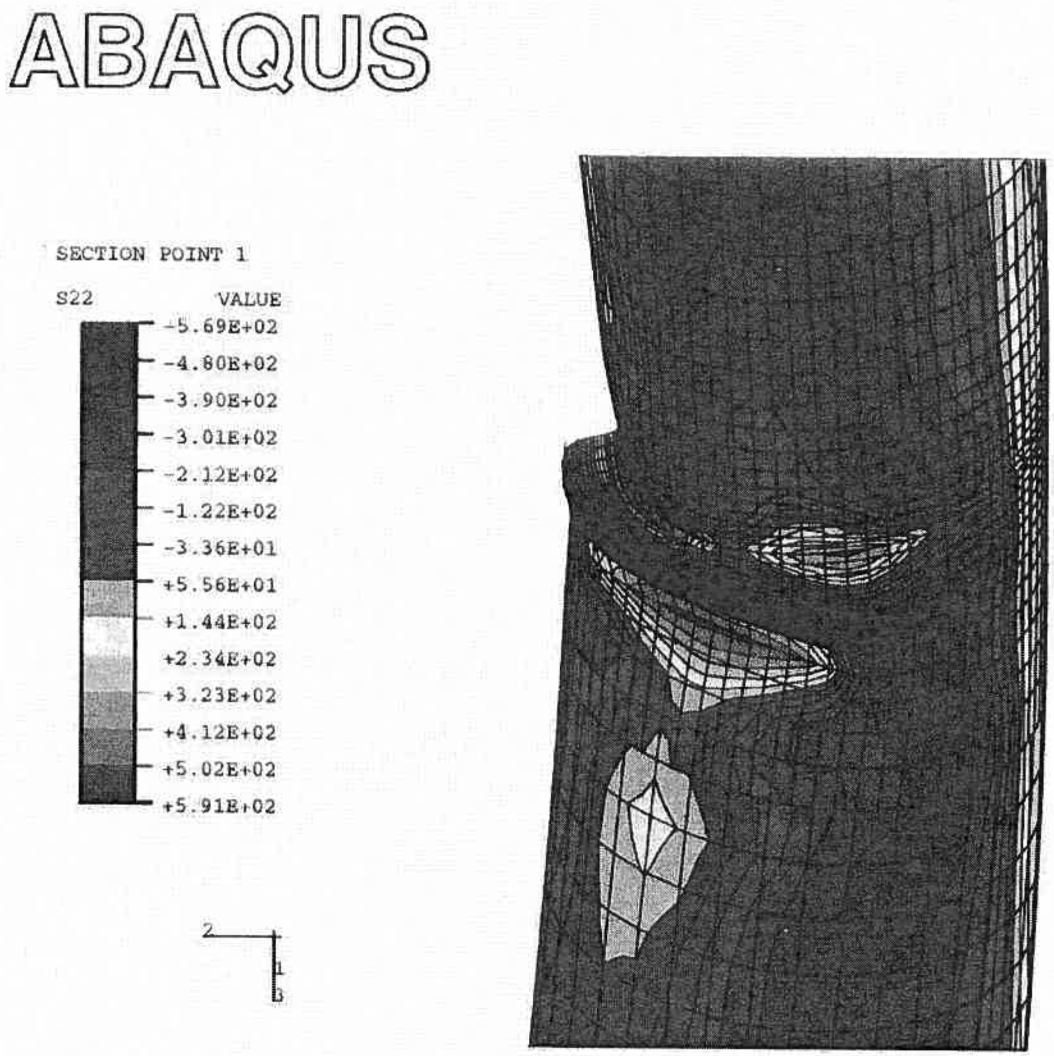

Figure 3.2.5(a). Longitudinal Stress (S22) at Section Point S1 for UGA12WEF3.

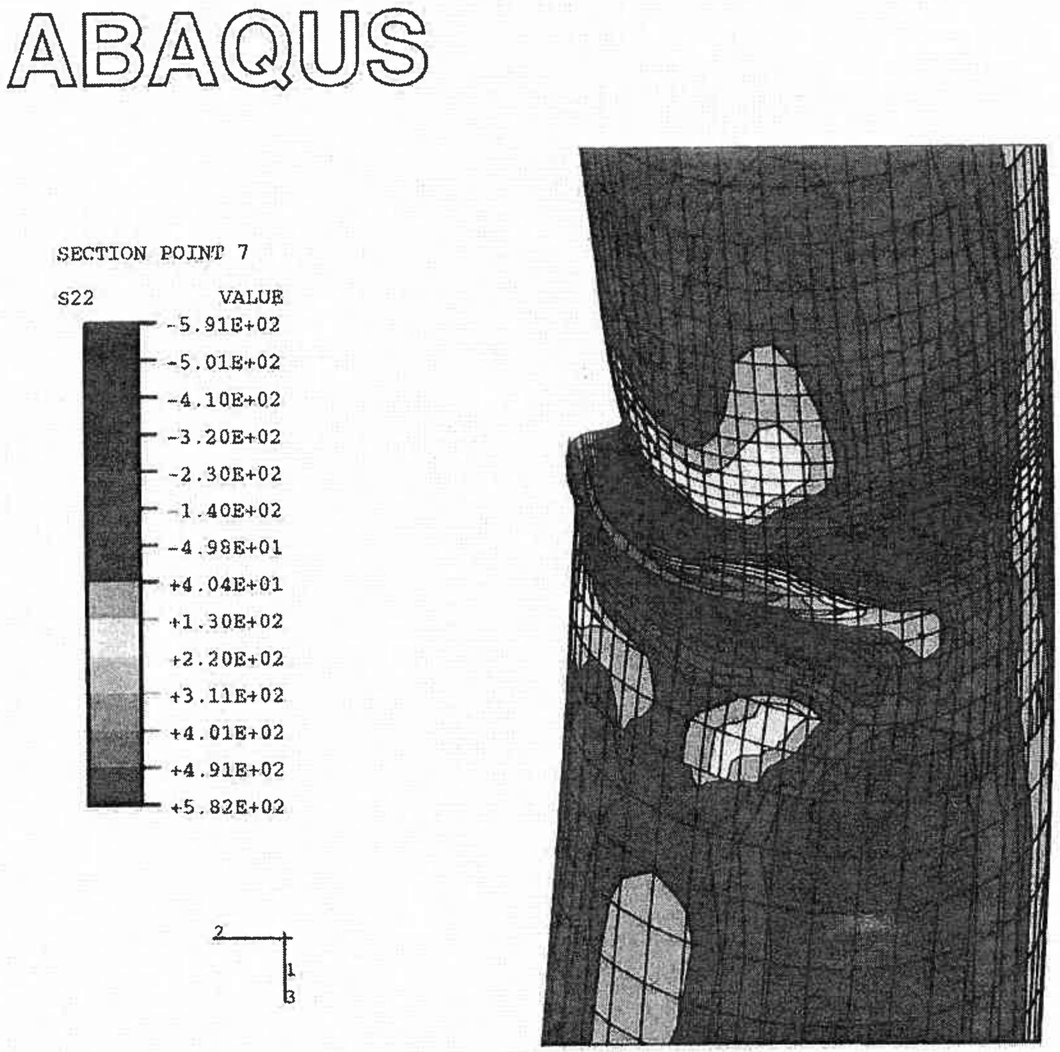

Figure 3.2.5(b). Longitudinal Stress (S22) at Section Point S7 for specimen UGA12WEF3.

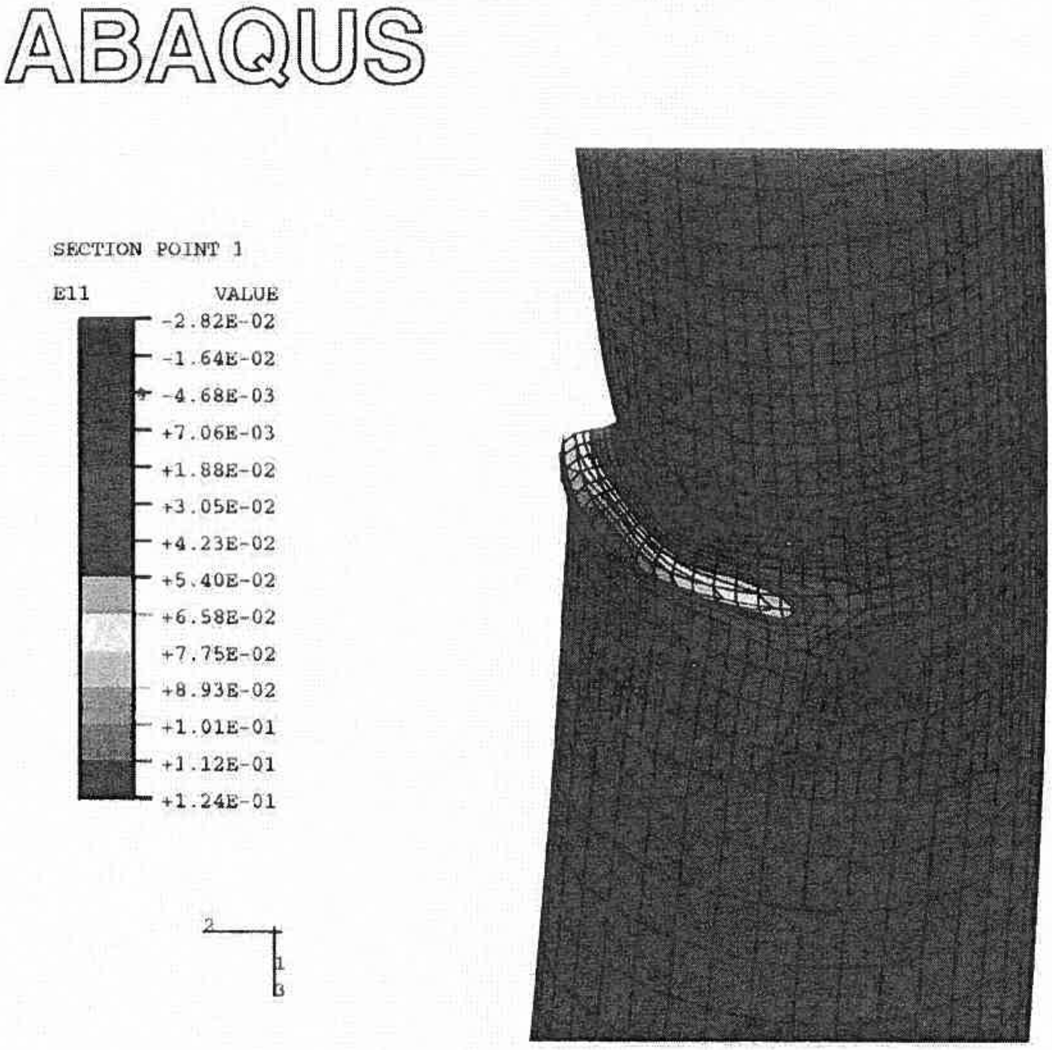

Figure 3.2.6(a). Circumferential Strain (E11) at Section Point S1 for specimen UGA12WEF3.

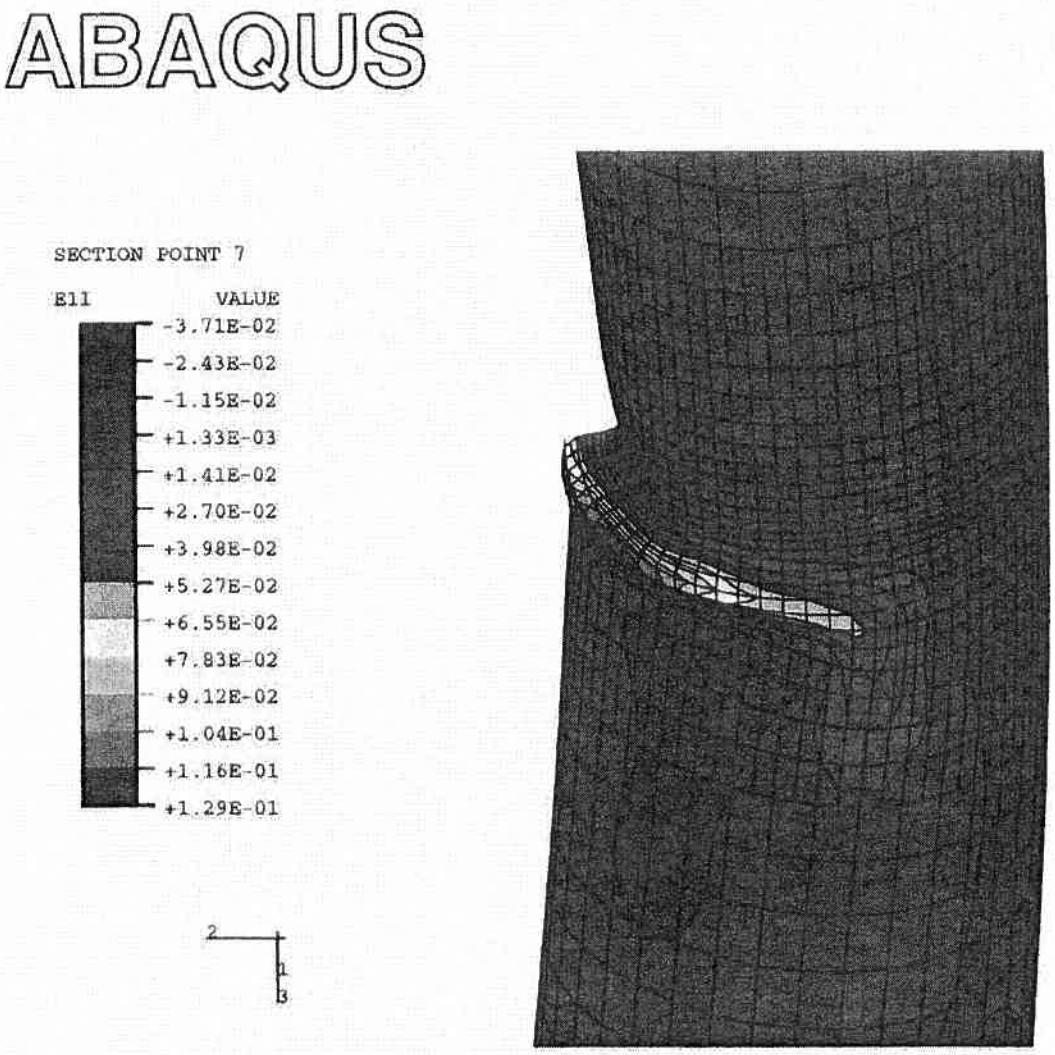

Figure 3.2.6(b). Circumferential Strain (E11) at Section Point S7 for specimen UGA12WEF3.

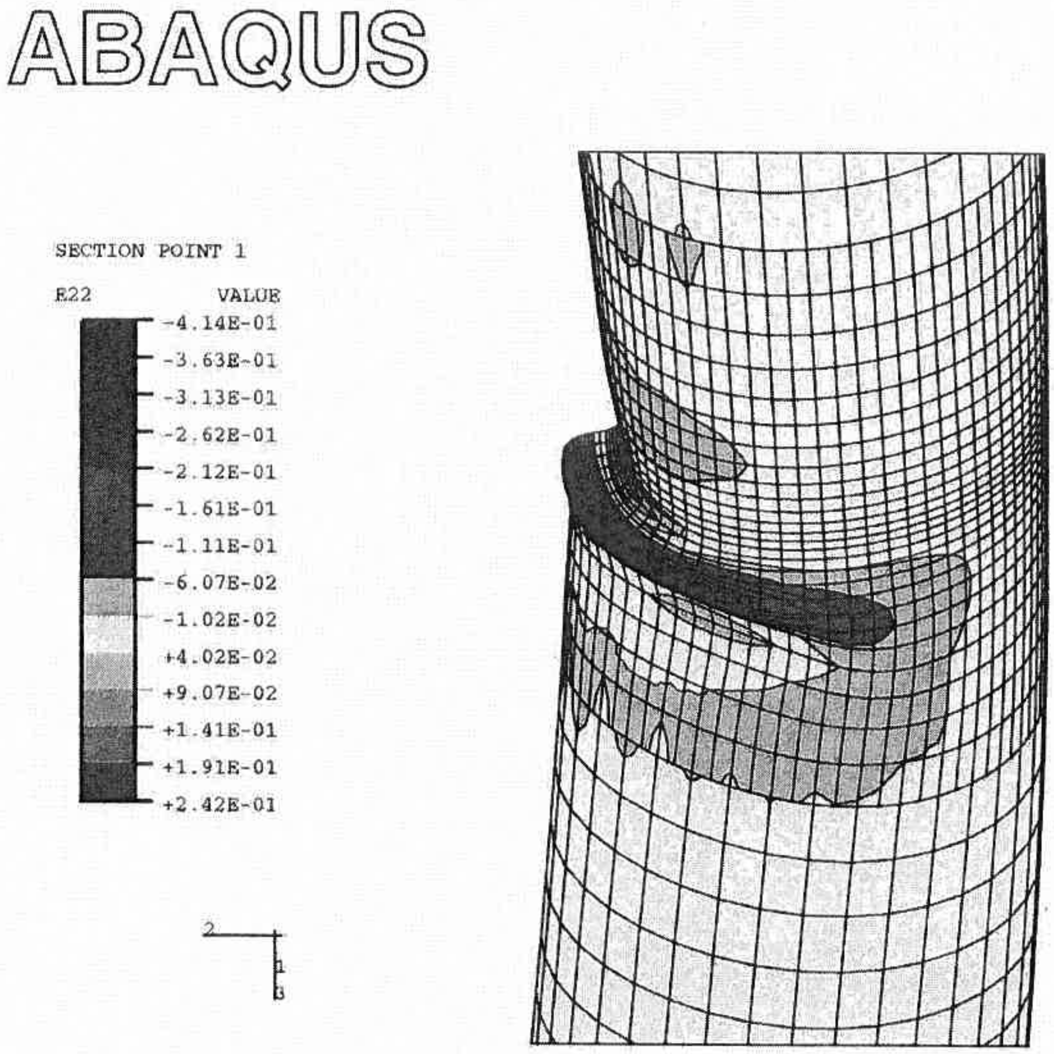

Figure 3.2.7(a). Principal Strain E22 at Section S1 for UGA12WEF3.

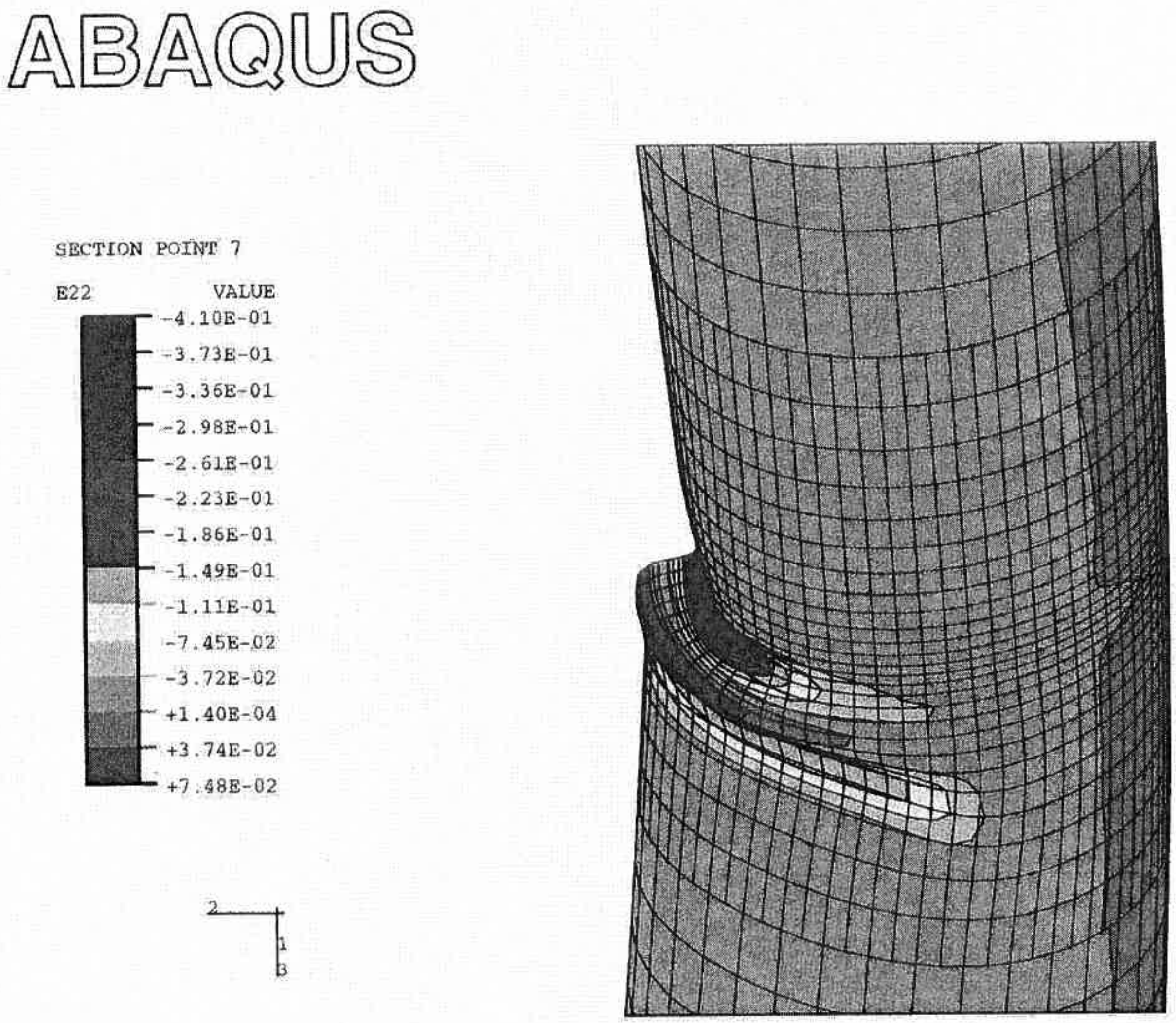

Figure 3.2.7(b). Principal Strain E22 at Section S7 for UGA12WEF3.

3.3 - SPECIMEN HGA12W

The results for the half-pressurized 12-inch pipe subjected to axial load, internal pressure and imposed moments (that result from imposed rotations in the analytical solution) are presented in this section. The analytical results corresponding to the specimen HGA12WEF3 are compared with the ones obtained from the test by Yoosef-Ghodsi, *et al*, (B1994b) defined in Table 1.2.

In Fig. 3.3.1 the average end moment vs. average curvature curve is shown both from the test and the analytical solution. The analytical ultimate resisting moment, which is equal to $M_{lim} = 179.79$ kN.m, is 6.3% lower than the experimental ultimate resisting moment. The softening point for the analytical solution is determined by inspection to be at the limit point since significant softening begins immediately thereafter. This point occurs for an average curvature of $K_{lim} = 47.3 \times 10^{-6} mm^{-1}$ which is 1.5% greater than the value obtained from the test.

The evolution of the deformed configuration along the loading history is shown in Fig. 3.3.2 for selected points on the moment vs. curvature curve. At point A of the moment vs. curvature curve, corresponding to $K/K_{lim}=1.10$ two bulges are developing approximately symmetrically about the middle of the pipe. From Point B ($K/K_{lim}=1.25$) up to the end of the moment vs. curvature curve only the lower bulge remains while the upper bulge disappears resulting in a one-bulge buckling shape that amplifies into a single outward-bulging wrinkle.

In Fig. 3.3.3(a) the realistic computer rendering of the final buckling configuration for one-half of the pipe is shown. This corresponds to the point E in the moment vs. curvature curve. In Figure 3.3.3(b), a photograph of the test specimen, taken after the test at an orientation of 90° from the orientation of Fig. 3.3.3(a), is shown. (Generally, photographs of the tests were taken with the camera located in the plane of symmetry rather than normal to this plane.) Comparison of these two pictures indicates that, also for this load case, there is a good correspondence in the behavior between the test and the analytical simulation. For both specimens the final configuration is a one-bulge buckle.

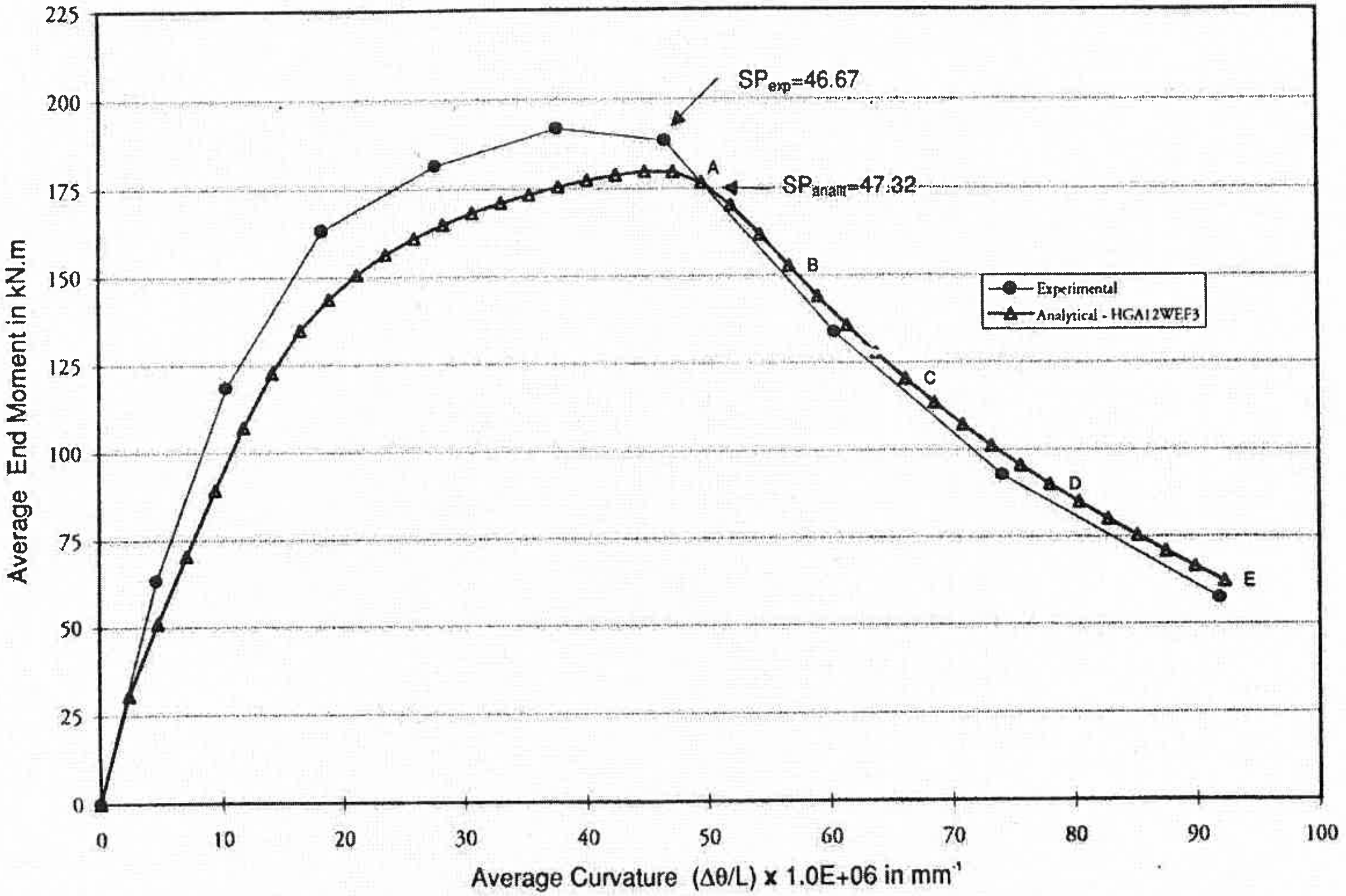

Figure 3.3.1. Average End Moment vs. Curvature for HGA12W pipe

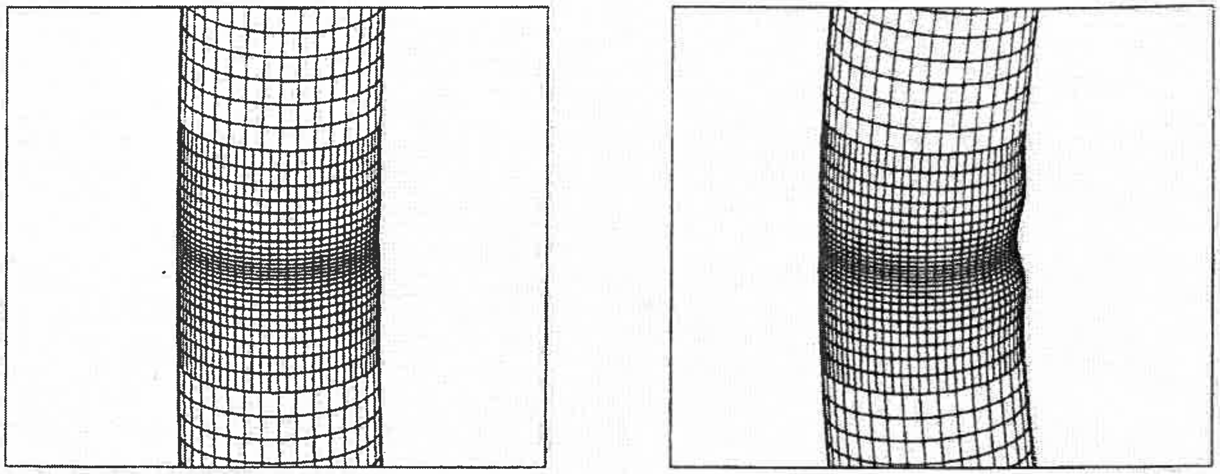

(a) Point A. K = 52.1E-06 /mm. Magnification Factor = 1.0.

(b) Point A. K = 52.1E-06 /mm. Magnification Factor = 4.0.

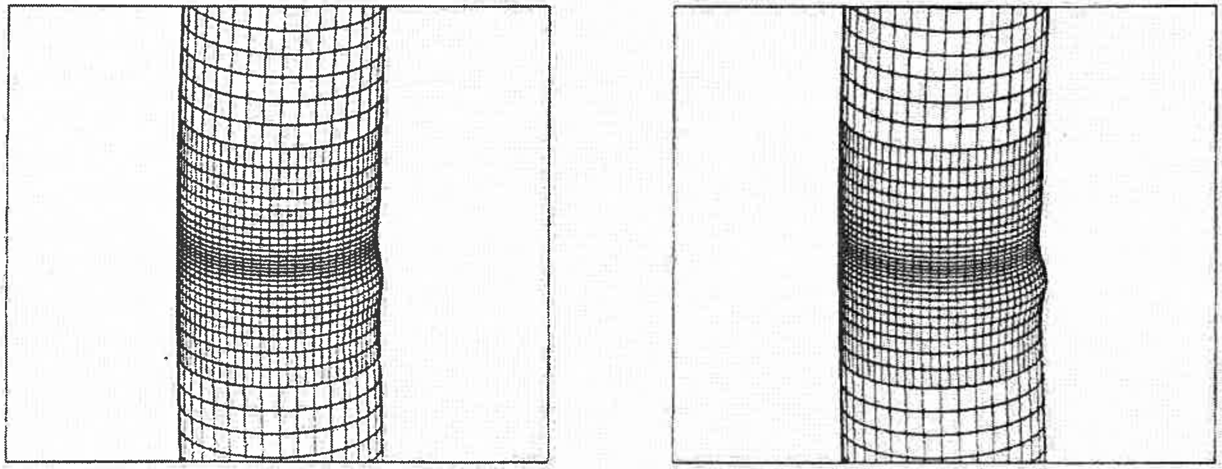

(c) Point B. K = 59.2E-06 /mm. Magnification Factor = 1.0.

(d) Point C. K = 68.6E-06 /mm. Magnification Factor = 1.0.

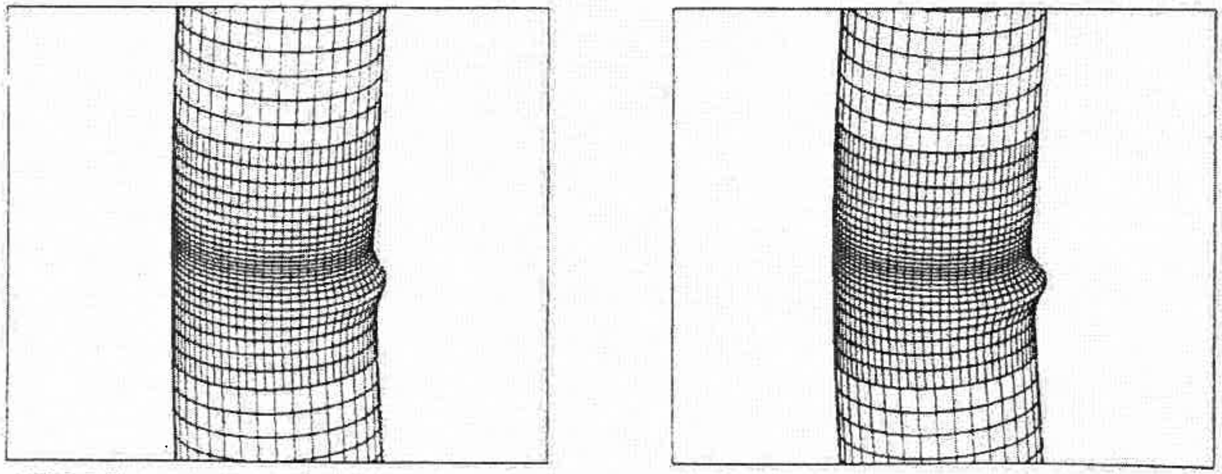

(e) Point D. K = 80.4E-06 /mm. Magnification Factor = 1.0.

(f) Point E. K = 94.5E-06 /mm. Magnification Factor = 1.0.

Figure 3.3.2. Evolution of buckling shape along the end moment vs. curvature (K) curve for specimen HGA12WEF3.

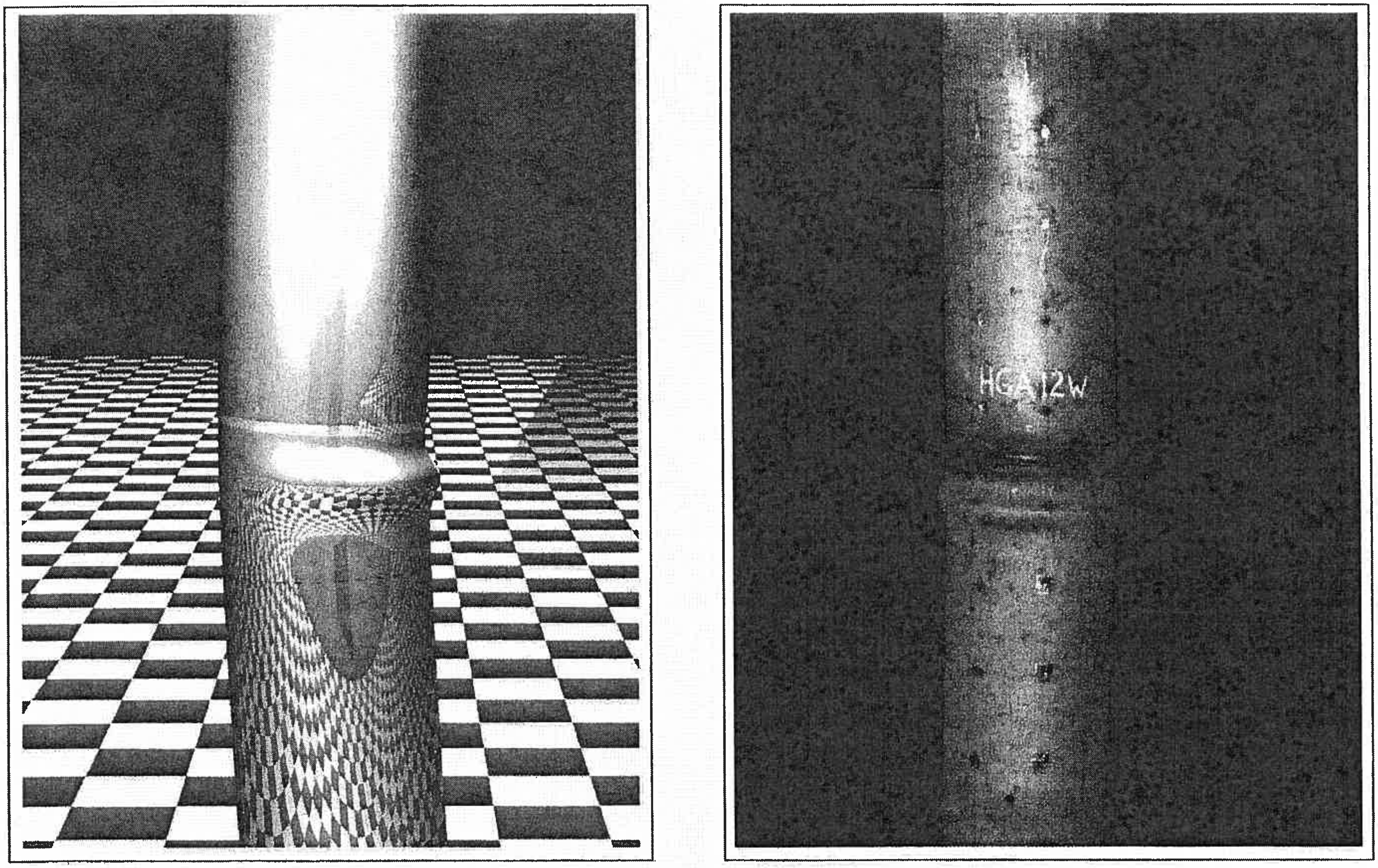

(a) Analytical Results for HGA12WEF3

(b) Experimental Test

Figure 3.3.3. Final Buckling Configuration for HGA12W pipe.

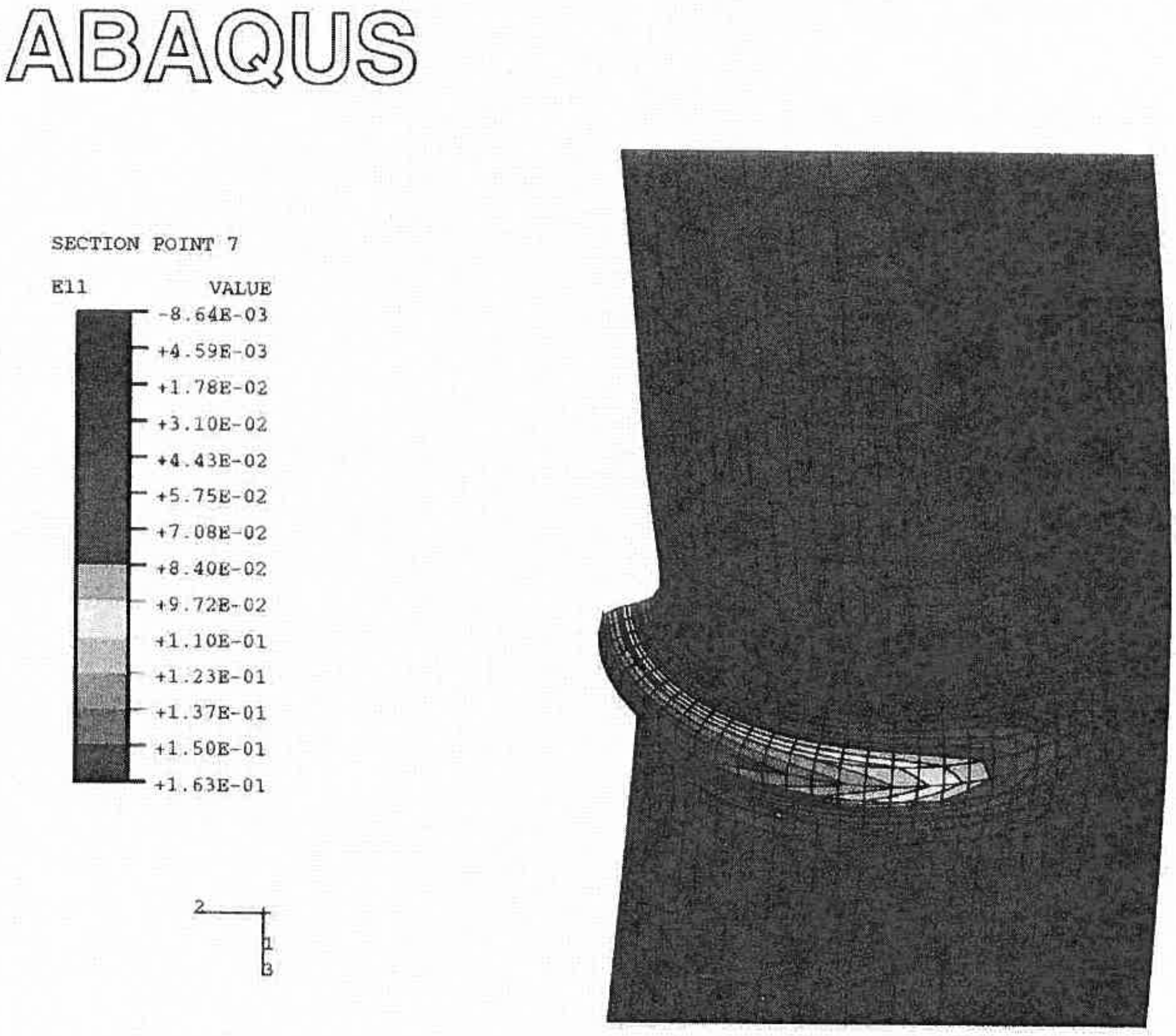

Figure 3.3.4. Circumferential Strain (E11) at Section Point S7 for specimen HGA12WEF3.

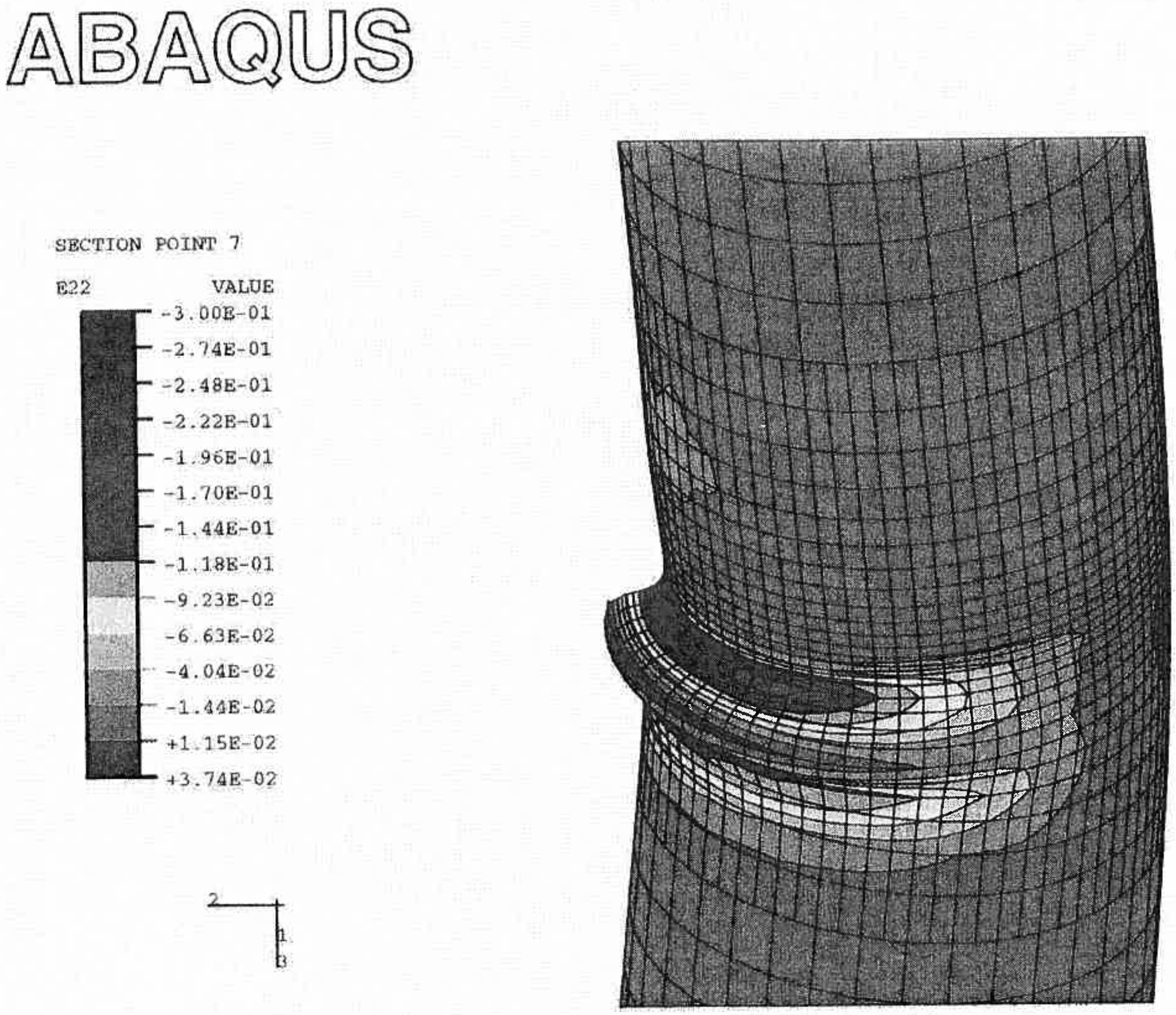

Figure 3.3.5. Longitudinal Strain (E22) at Section Point S7 for specimen HGA12WEF3.

Figures 3.3.4 and 3.3.5 show the strain distribution in the circumferential (E11) and the longitudinal (E22) directions, for the outside surface (section point S7 through the thickness). The circumferential strain (E11) is nearly constant and mostly of tension over the surface, reaching values of 1.78% (tension) on the outside surface along the compression side. On the wrinkle the circumferential strain reaches values of 16.30% (tension). The longitudinal strain (E22) is also nearly constant over the surface, reaching values of -4.04% (compression) on the outside surface along the compression side and 3.74% (tension) along the tension side. On the wrinkle the longitudinal strain reaches values of -30.00% (compression).

3.4 - SPECIMEN DGA12W

The results for the fully-pressurized 12-inch pipe subjected to axial load, internal pressure and imposed moments (imposed rotations in the analytical solution) are presented in this section. The analytical results corresponding to the specimen DGA12WEF3 are compared with the ones obtained from the test by Yoosef-Ghodsi, *et al*, (B1994b) defined in Table 1.2. In Fig. 3.4.1 the average end moment vs. average curvature curve is shown both from the tests and the analytical solution.

The analytical ultimate resisting moment, which is equal to $\mathbf{M}_{\lim} = 132.12$ kN m is 7.8% lower than the experimental ultimate resisting moment. In contrast to the experimental test, the analytical moment vs. curvature curve in this case does not exhibit a distinct softening point but undergoes a gradual softening with the development of a more diffuse wrinkle. This appears to be characteristic behavior for the analytical solutions of the local buckling and subsequent wrinkling in highly pressurized pipe. Consequently, the softening point is defined as that point at which the moment has decreased by 5% from the limit value, as discussed in Sect. 3.1. This point corresponds to an average curvature of $\mathbf{K}_{\lim} = 61.5 \times 10^{-6} mm^{-1}$ which is 19.3% lower than the value obtained from the test.

The evolution of the deformed configuration along the loading history is shown in Fig. 3.4.2 for selected points on the moment vs. curvature curve. At point A of the moment vs. curvature curve, corresponding to $K/K_{\lim}=0.85$ two bulges are developing approximately symmetrically about the middle of the pipe. This trend continues along the softening branch of the moment vs. curvature curve, up to point D ($K/K_{\lim}=1.50$) after which the top bulge stays unchanged while the lower bulge continuously increases. The upper bulge does not, however, disappear as it did for specimen HGA12WEF3 even though the final buckling configuration, corresponding to point F ($K/K_{\lim}=1.92$), contains only one dominant wrinkle.

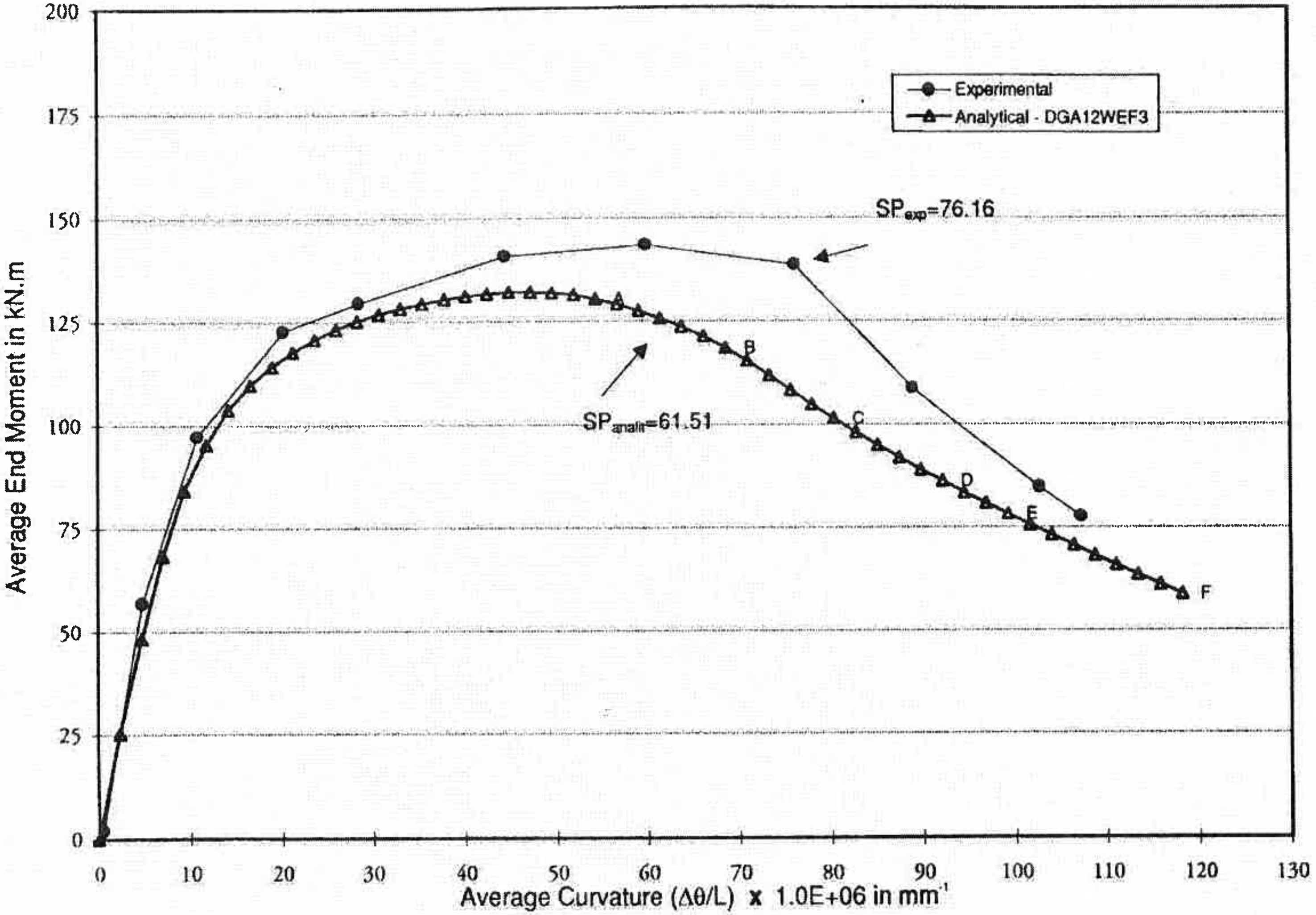

Figure 3.4.1. Average End Moment vs. Curvature for DGA12W pipe

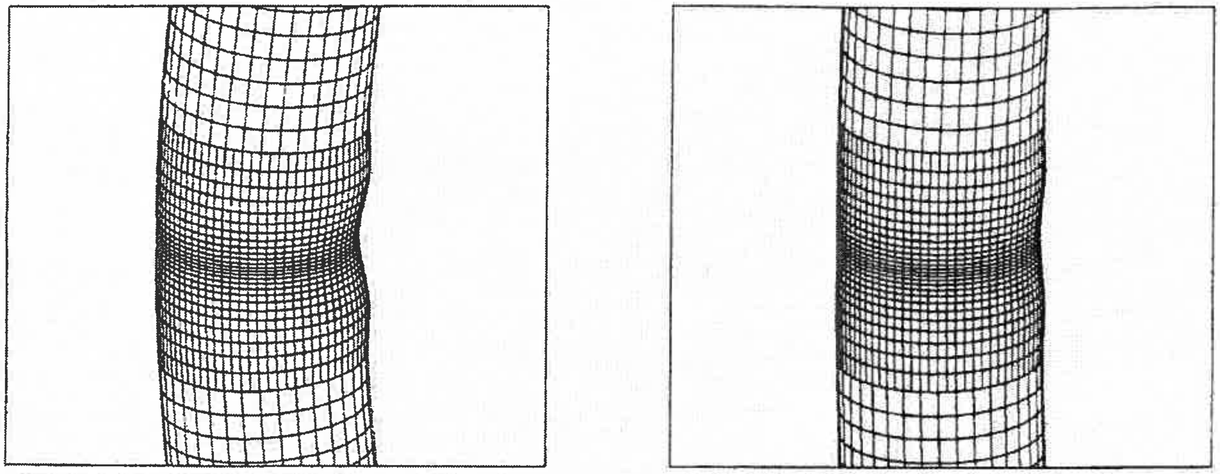

(a) Point A. K = 52.5E-06 /mm. Magnification Factor = 4.0.

(b) Point B. K = 66.2E-06 /mm. Magnification Factor = 1.0.

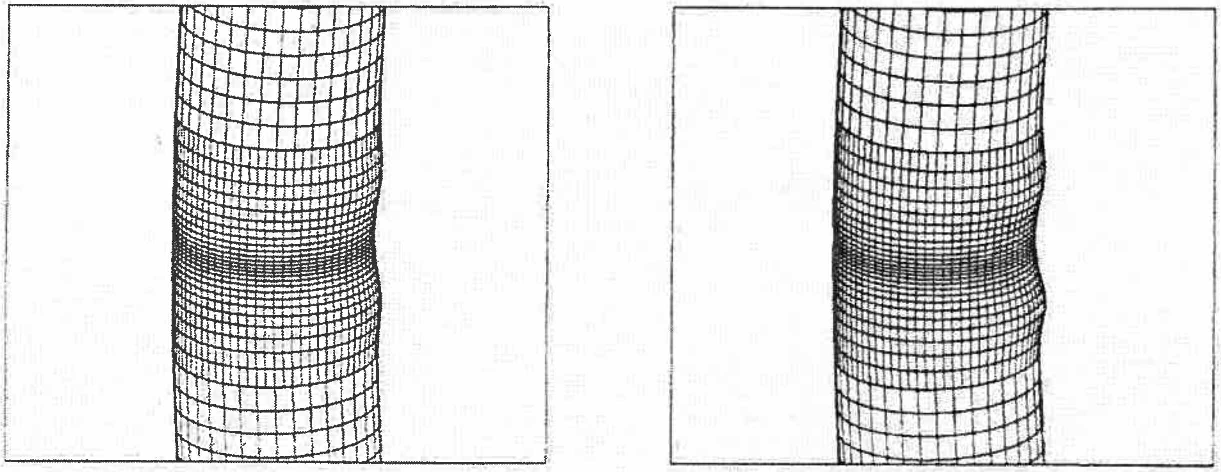

(c) Point C. K = 80.4E-06 /mm. Magnification Factor = 1.0.

(d) Point D. K = 92.2E-06 /mm. Magnification Factor = 1.0.

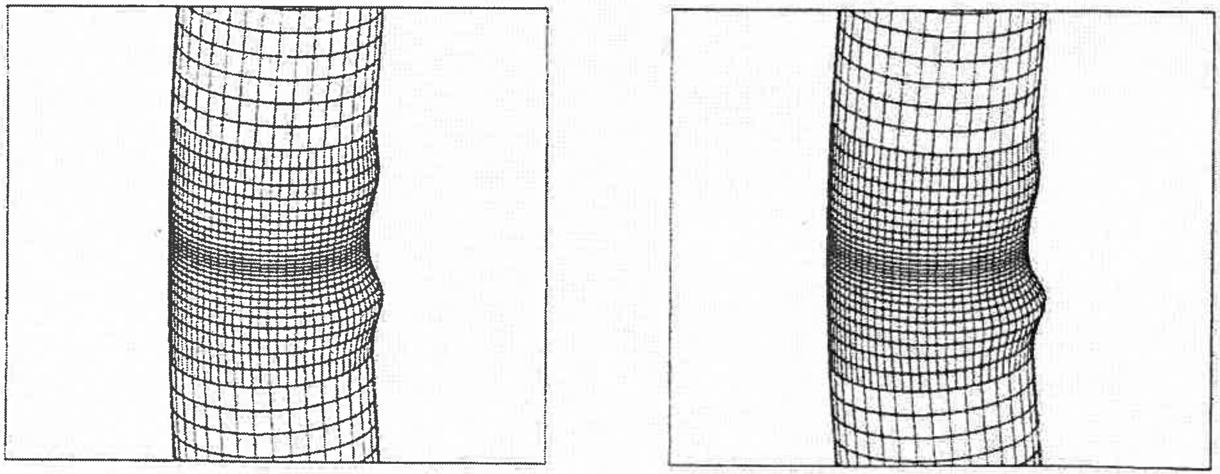

(e) Point E. K = 99.3E-06 /mm. Magnification Factor = 1.0.

(f) Point F. K = 118.1E-06 /mm. Magnification Factor = 1.0.

Figure 3.4.2. Evolution of buckling shape along the end moment vs. curvature (K) curve for specimen DGA12WEF3.

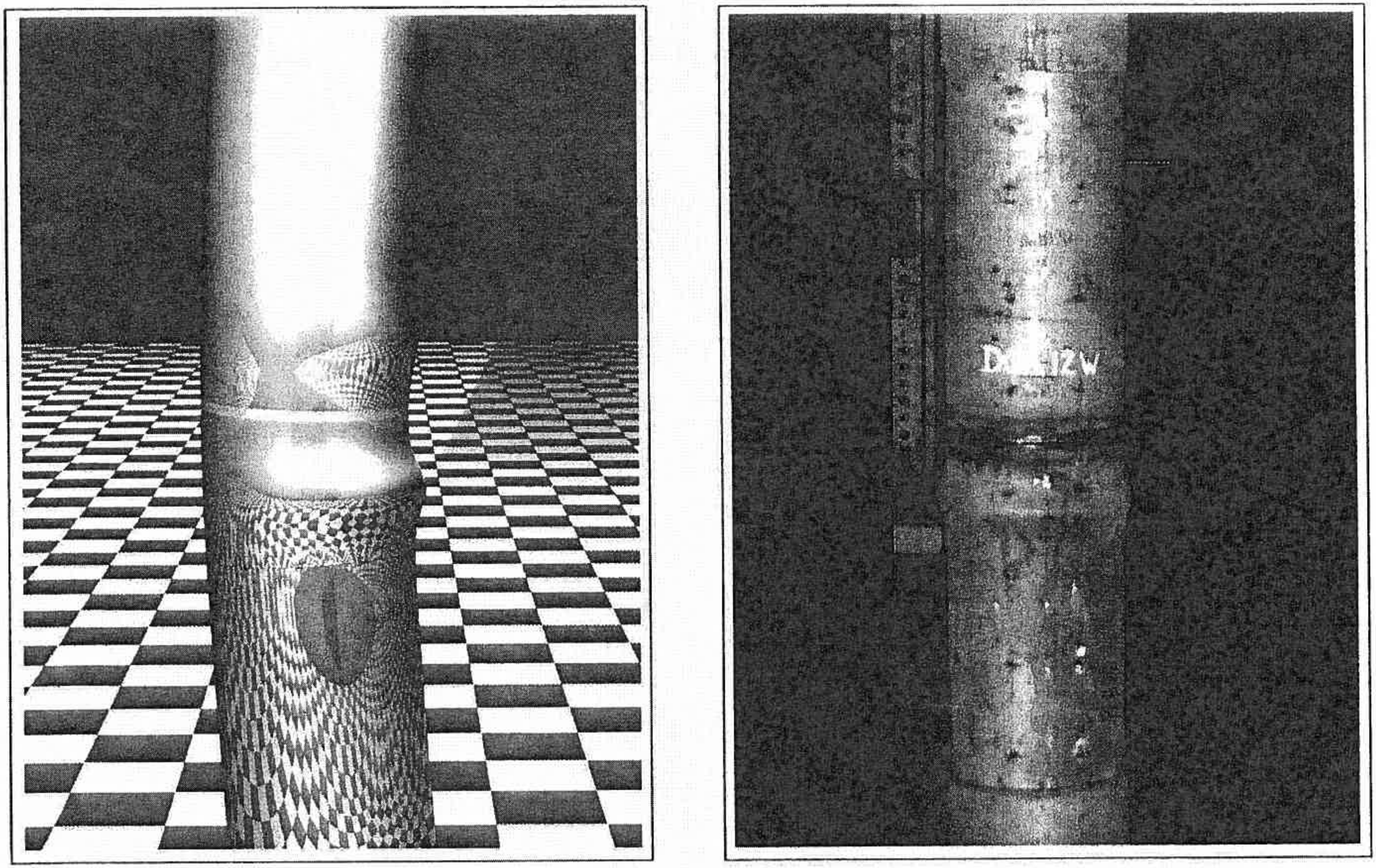

(a) Analytical Results for DGA12WEF3

(b) Experimental Test

Figure 3.4.3. Final Buckling Configuration for DGA12W pipe.

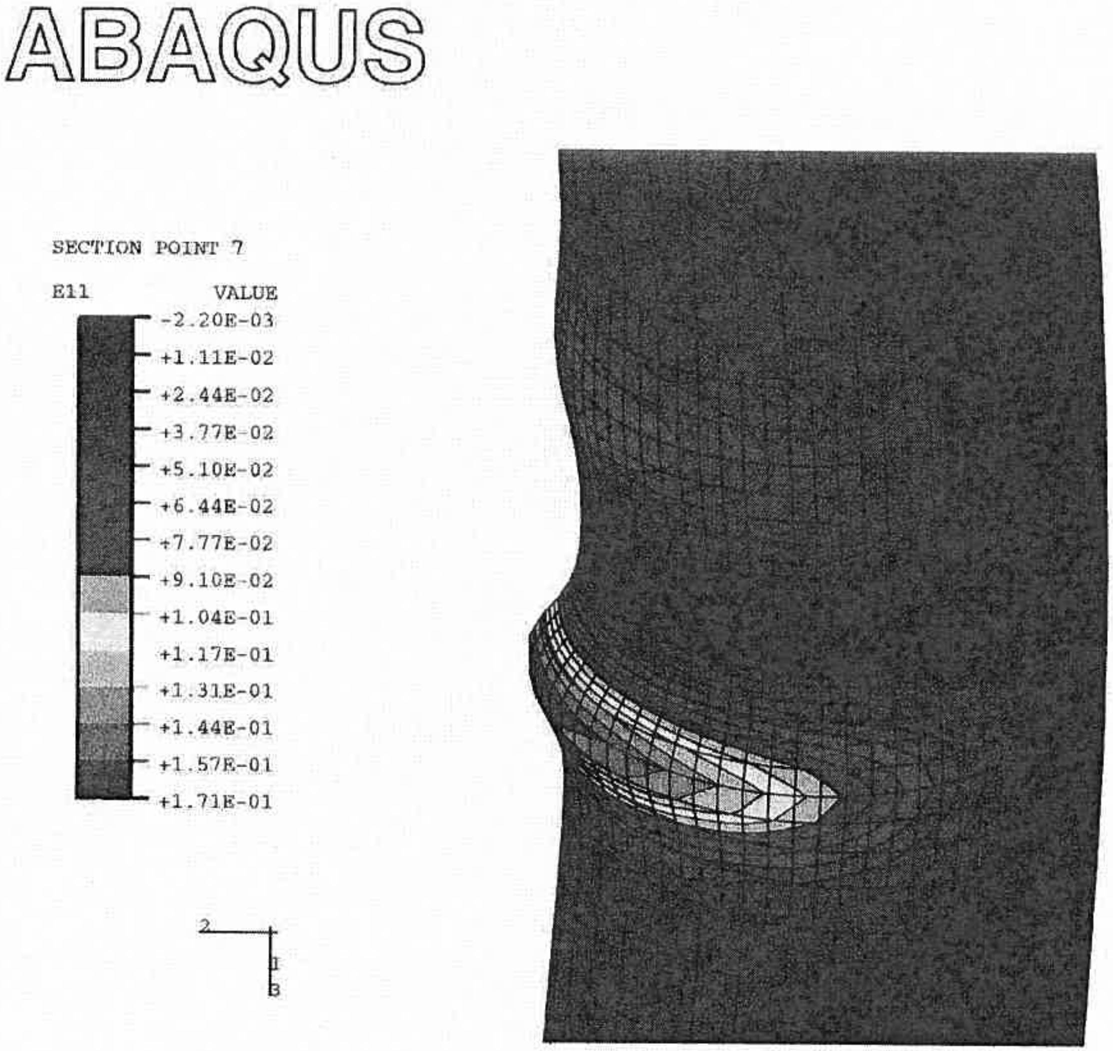

Figure 3.4.4. Circumferential Strain (E11) at Section Point S7 for specimen DGA12WEF3.

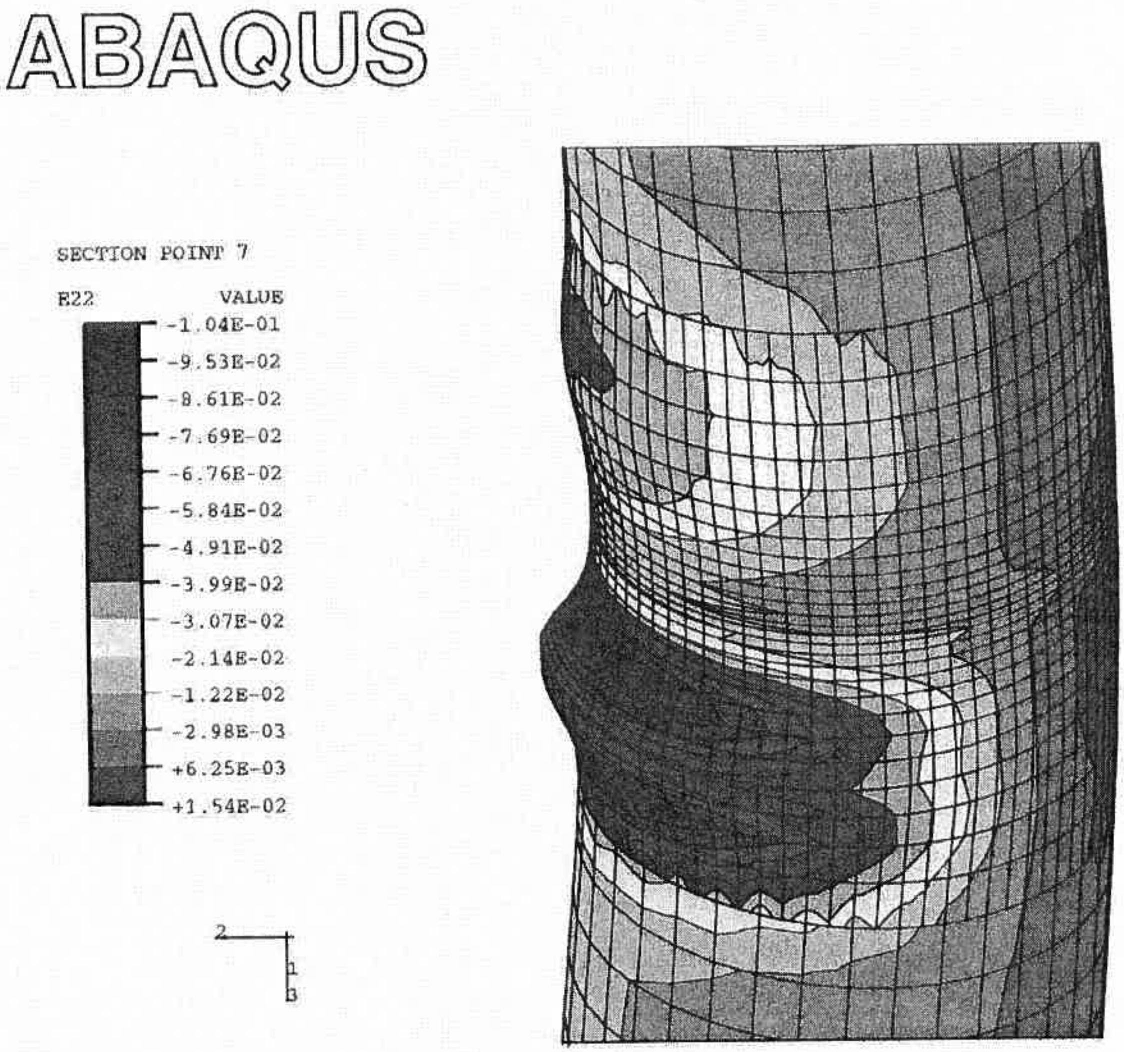

Figure 3.4.5. Longitudinal Strain (E22) at Section Point S7 for specimen DGA12WEF3.

In Fig. 3.4.3(a) the realistic computer rendering of the final buckling configuration for one-half of the pipe is shown. This corresponds to the point F in the moment vs. curvature curve. In Figure 3.4.3(b), a photograph of the test specimen, taken after the test at an orientation of 90 ° from the orientation of Fig. 3.4.3(a), is shown. Comparison of these two pictures indicates that, also for this load case, there is a good correspondence in the behavior between the test and the analytical simulation. For both specimens the final configuration contains one bulge whose distance to the girth weld is approximately one-third of the pipe diameter.

Figures 3.4.4 and 3.4.5 show the strain distribution in the circumferential (E11) and the longitudinal (E22) directions, for the outside surface (section point S7 through the thickness). The circumferential strain (E11) varies mostly in the regions where the wrinkles are developed, reaching values in tension which greatly exceed the yield strain, and whose maximum value is equal to 17.1% (tension) on the outside surface along the compression side, on the crest of the lower wrinkle. Unlike the half-pressurized specimen, the longitudinal strain (E22) for this specimen varies over the outside surface, reaching values of -10.40% (compression) along the compression side in the neighborhood of the lower wrinkle and 1.54% (tension) along the tension side.

3.5 - SPECIMENS UGA20W-1 AND UGA20W-2

The results for the unpressurized 20-inch pipe subjected to axial load and imposed moments (imposed rotations in the analytical solution) are presented in this section. The analytical results corresponding to the specimen UGA20WEF3 are compared with the ones obtained from the tests by Yoosef-Ghodsi, *et al*, (B1994b) defined in Table 1.2.

In Fig. 3.5.1 the average end moment vs. average curvature curve is shown both from the test and the analytical solution. The analytical ultimate resisting moment, which is equal to $\mathbf{M}_{\text{lim}}$ = 527.97 kn., is 11.5% higher than the experimental ultimate resisting moment for the specimen UGA20W-1 and 17.5% lower than the experimental ultimate resisting moment for the specimen UGA20W-2. The comparison with the experimental results for these specimens is somewhat uncertain because, in both cases, difficulties in carrying out the tests resulted in prior plastic strains being introduced as a result of a loading-unloading cycle without proper measurements being recorded. The softening point for the analytical solution is apparent from the shape of the curve and occurs for the average curvature $\mathbf{K}_{\text{lim}} = 14.2 \times 10^{-6} mm^{-1}$. In order for comparisons with the experimental results to be possible, the softening points from the tests have first been determined from moment vs. curvature curves which have been translated away from the curvature origin so as to compensate for the initial deformation. The values for the experimental softening points were then corrected by subtracting the offset at which the curve intersects the horizontal axis. The analytical softening point obtained is then 46.5% greater than the approximate SP value from specimen UGA20W-1 and 28.4% lower than the approximate SP value from specimen UGA20W-2. The experimental softening points are identified by inspection as those at the peak of the curves, as these are the first points on the descending branch of the moment vs. curvature curves.

The evolution of the deformed configuration along the loading history is shown in Fig. 3.5.2 for selected points on the moment vs. curvature curve. Initially, one bulge starts to develop in the neighborhood of the girth weld (point A, for $K/K_{lim}=1.0$). At point B ($K/K_{lim}=2.0$) no additional deformation occurs to the bulge and an inward buckle starts to develop right above the girth weld. This progresses up to point C ($K/K_{lim}=3.0$), and the bulge disappears. At point D ($K/K_{lim}=3.8$) a diamond-shape pattern develops. It increases continuously up to the end of the moment vs. curvature curve, corresponding to point F ($K/K_{lim}=5.8$).

In Fig. 3.5.3(a) the realistic computer rendering of the final buckling configuration for one-half of the pipe is shown. This corresponds to point F on the moment vs. curvature curve. In Figure 3.5.3(b) a photograph of the test specimen, taken after the test at an orientation of 90 ° from the orientation of Fig. 3.5.3(a), is shown. Comparison of these two pictures indicates that, also for this load case, there is a good correspondence in the behavior between the test and the analytical simulation. For both specimens the final buckling configuration contains a diamond-shape pattern along the circumferential direction in which the dimples alternate on opposite sides of the girth weld.

Figures 3.5.4 and 3.5.5 show the strain distribution corresponding to the final analysis step along the circumferential (E11) and the longitudinal (E22) directions, respectively, for the outside surface (section point S7 through the thickness). The circumferential strain (E11) is mostly compressive over the outside surface reaching values of -3.48% (compression). On the wrinkle crest the circumferential strain reaches values of 13.40% (tension). The longitudinal strain (E22) is nearly constant reaching values of 3.91% (tension) on the outside surface both along the compression side and the tension side of the pipe. On the wrinkle crest the circumferential strain reaches values of 20.10% (tension) and -50.10% (compression) in the wrinkle depression.

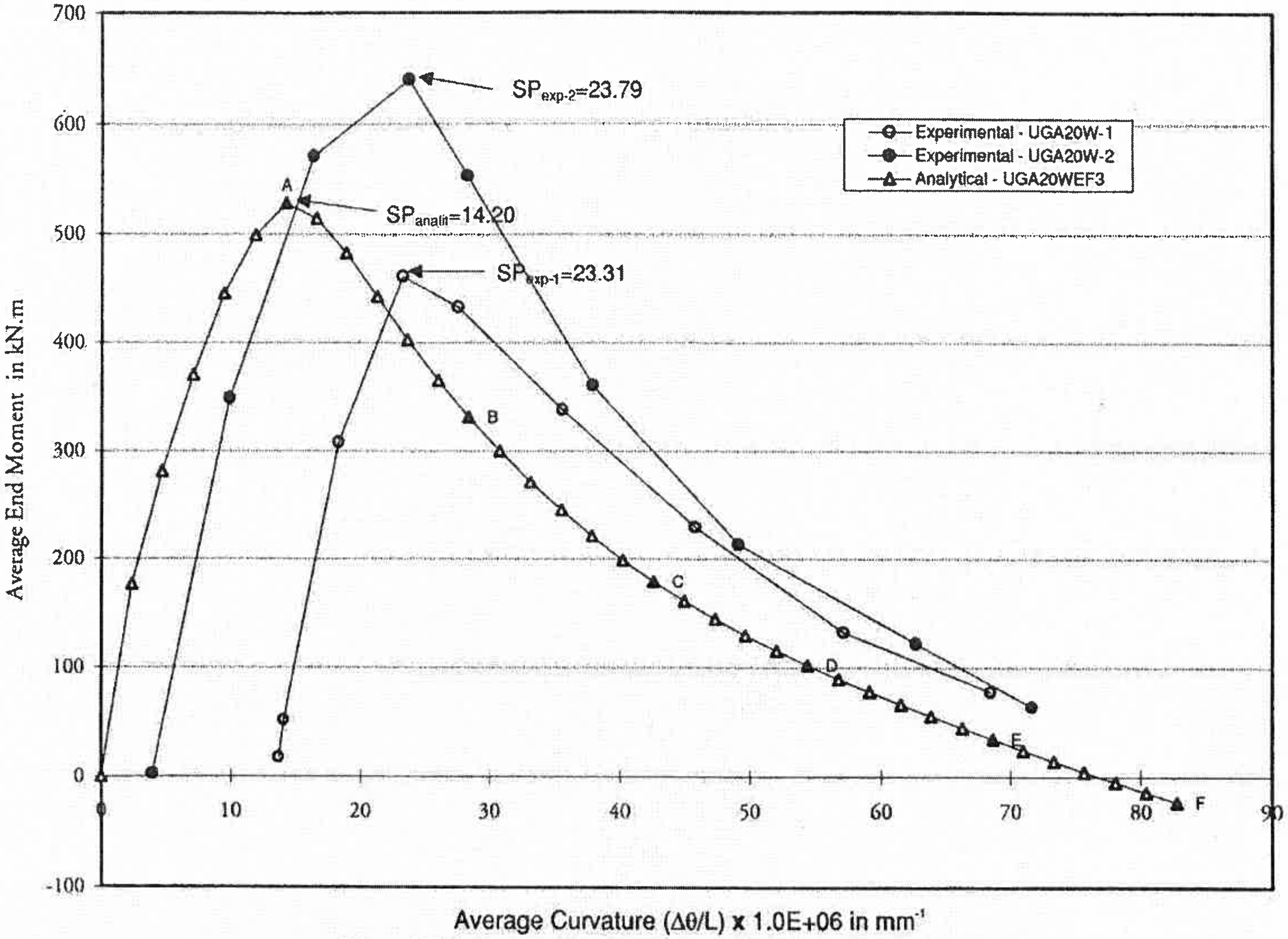

Figure 3.5.1. Average End Moment vs. Curvature for UGA20W pipe

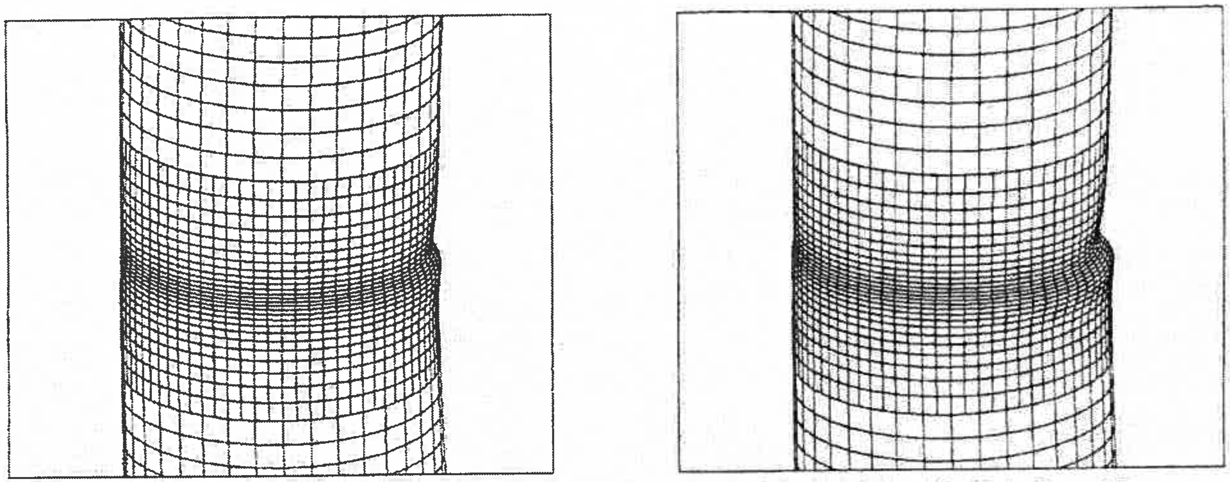

(a) Point A. K = 14.2E-06 /mm. Magnification Factor = 4.0.

(b) Point B. K = 28.4E-06 /mm. Magnification Factor = 1.0.

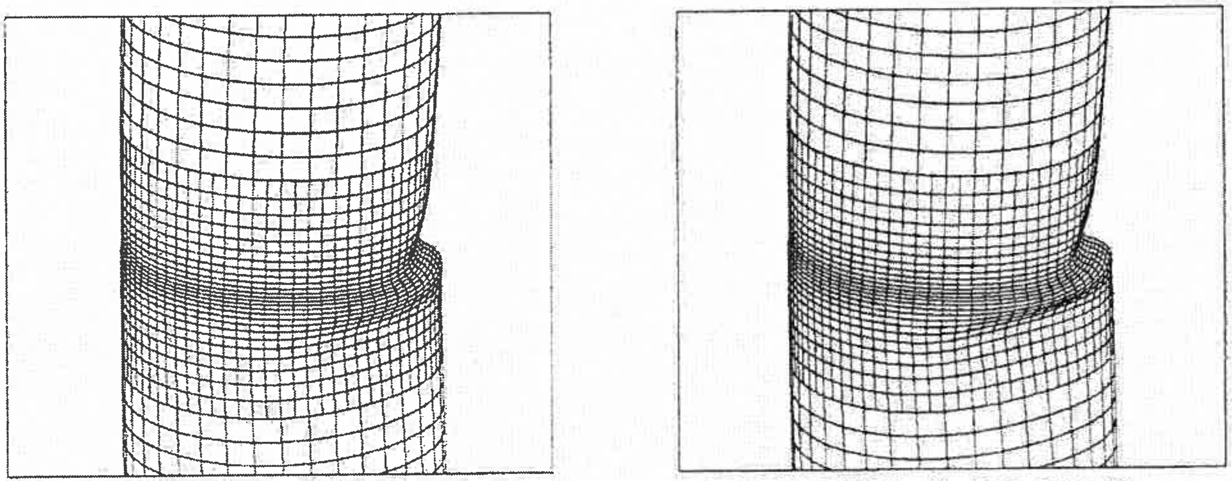

(c) Point C. K = 42.6E-06 /mm. Magnification Factor = 1.0.

(d) Point D. K = 54.4E-06 /mm. Magnification Factor = 1.0.

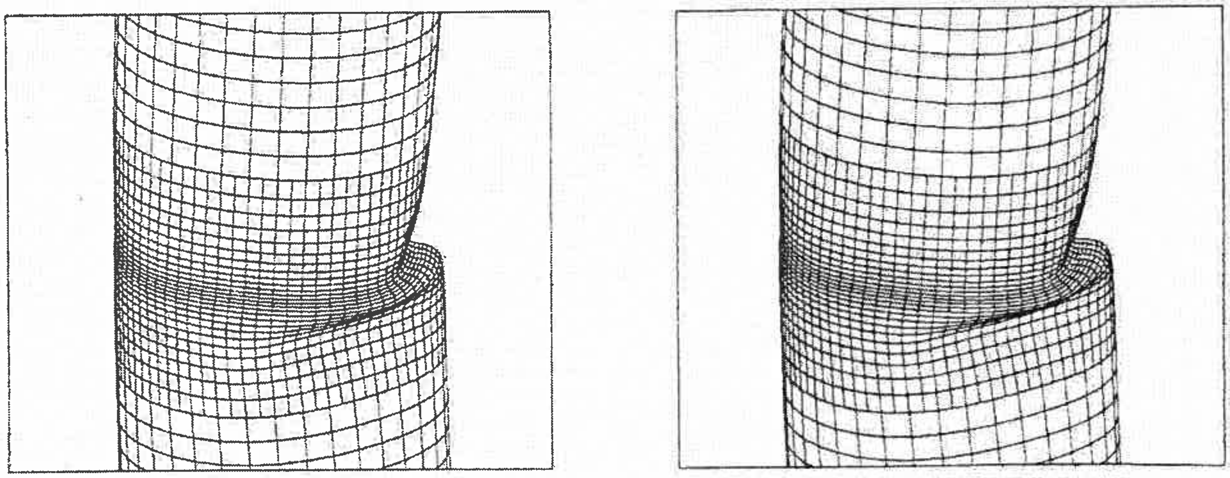

(e) Point E. K = 68.6E-06 /mm. Magnification Factor = 1.0.

(f) Point F. K = 82.8E-06 /mm. Magnification Factor = 1.0.

Figure 3.5.2. Evolution of buckling shape along the end moment vs. curvature (K) curve for specimen UGA20WEF3.

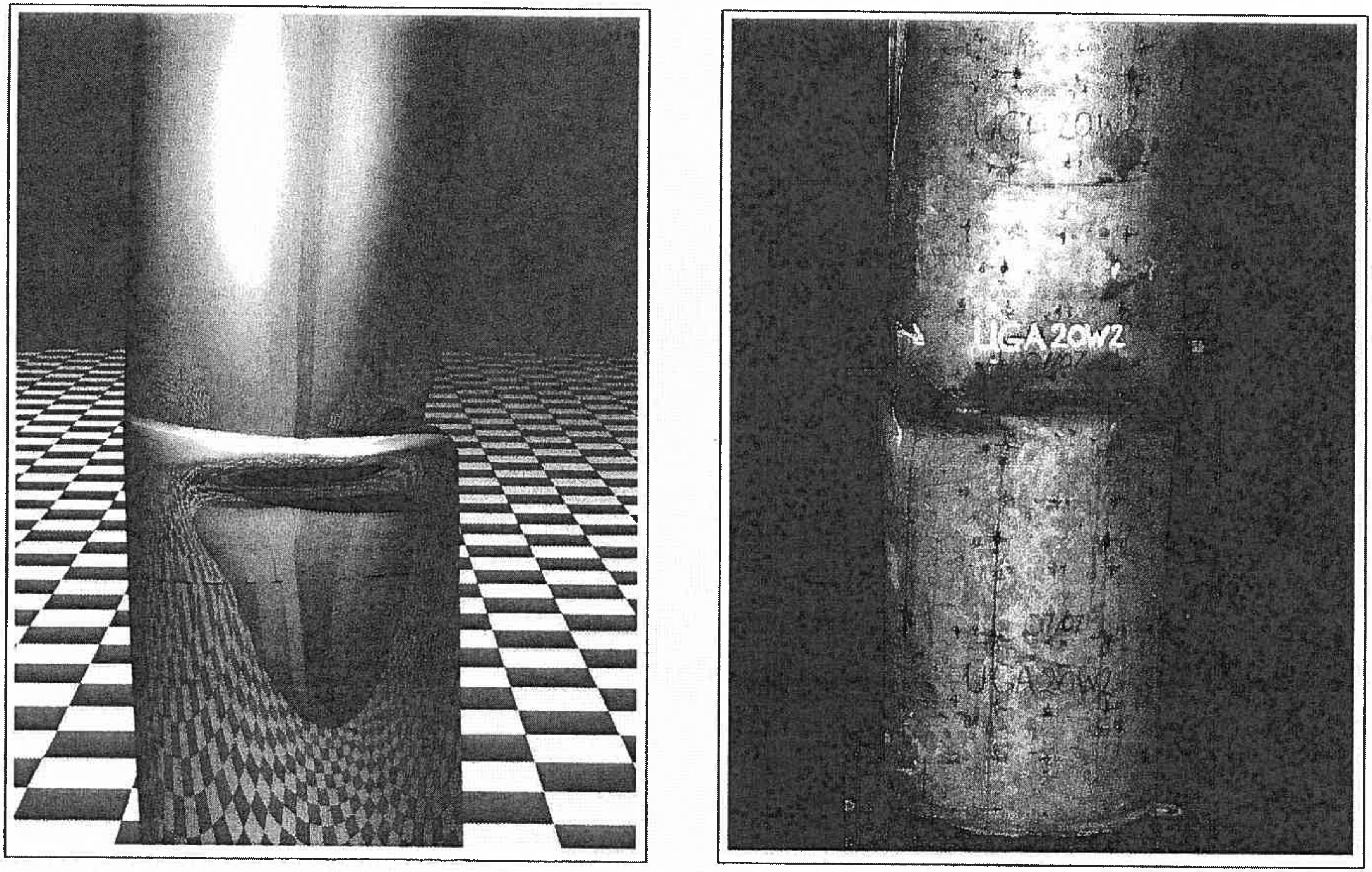

(a) Analytical Results for UGA20WEF3

(b) Experimental Test

Figure 3.5.3. Final Buckling Configuration for UGA20W pipe.

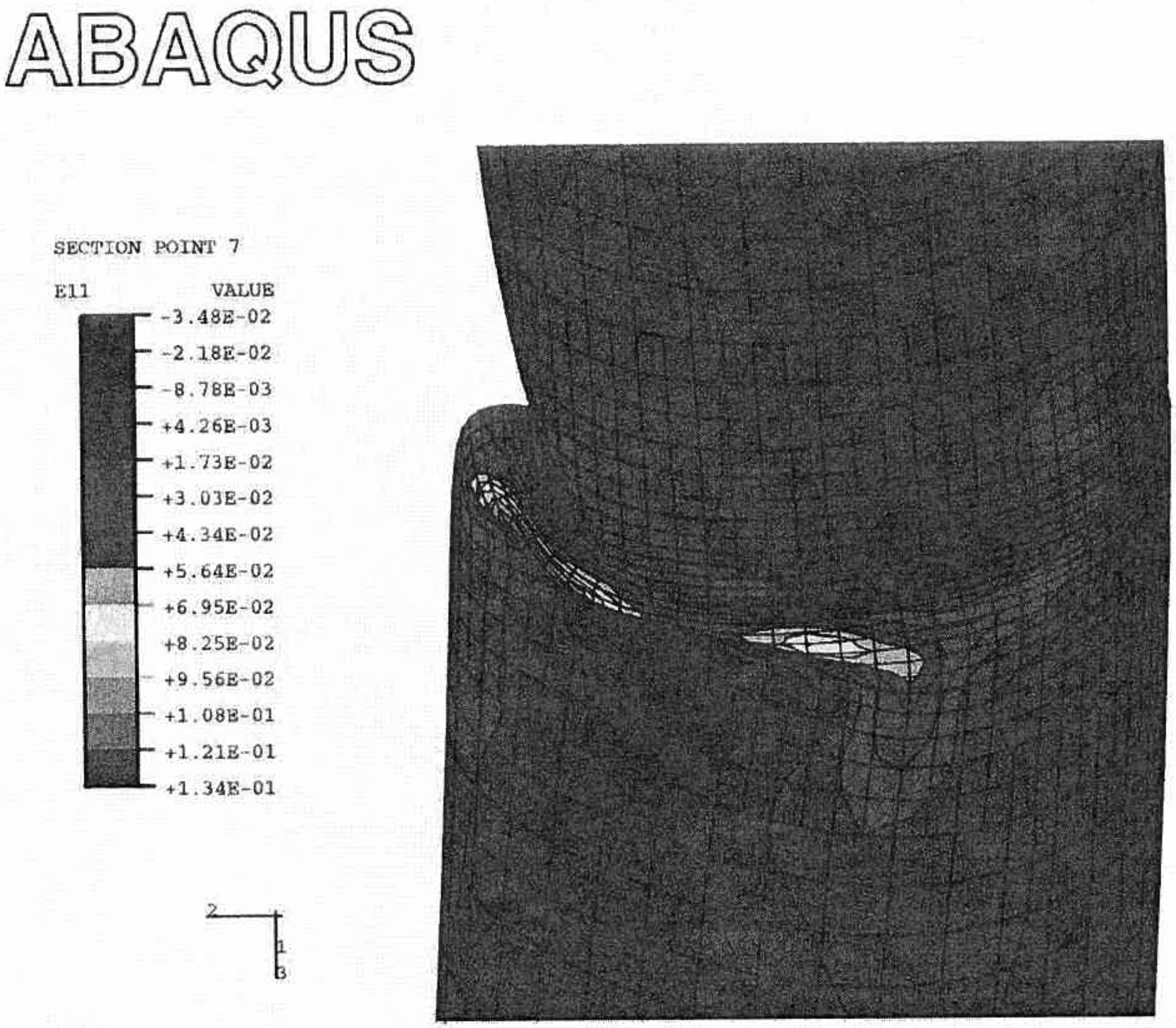

Figure 3.5.4. Circumferential Strain (E11) at Section Point S7 for specimen UGA20WEF3.

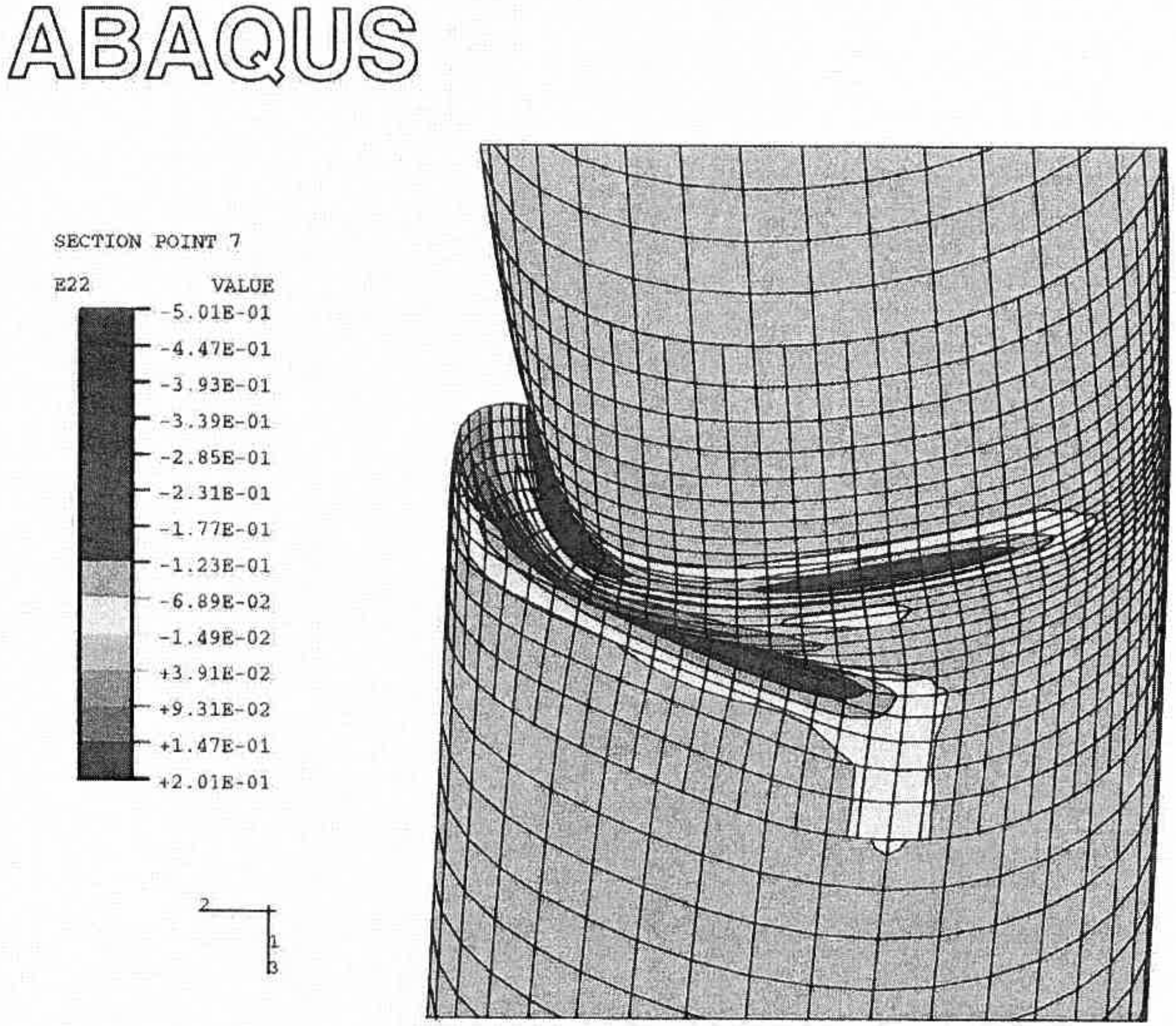

Figure 3.5.5. Longitudinal Strain (E22) at Section Point S7 for specimen UGA20WEF3.

3.6 - SPECIMEN HGA20W

The results for the half-pressurized 20-inch pipe subjected to axial load, internal pressure and imposed moments (rotations) are presented in this section. The analytical results corresponding to the specimen HGA20WEF3 are compared with the ones obtained from the test by Yoosef-Ghodsi, *et al*, (B1994b) defined in Table 1.2.

In Fig. 3.6.1 the average end moment vs. average curvature curve is shown both from the tests and the analytical solution. The analytical ultimate resisting moment, which is equal to $\mathbf{M}_{\text{lim}} = 533.25$ kN. m, is 8.9% lower than the experimental ultimate resisting moment. The softening point for the analytical solution is determined by inspection to be at the limit point since significant softening begins immediately thereafter. This point occurs for an average curvature of $\mathbf{K}_{\text{lim}} = 26.0 \times 10^{-6} mm^{-1}$ which is 5.4% lower than the value obtained from the test.

The evolution of the deformed configuration along the loading history is shown in Fig. 3.6.2 for selected points on the moment vs. curvature curve. The behavior of specimen HGA20WEF3, with D/t = 63, is practically identical to that of specimen HGA12WEF3, with D/t = 50, analyzed in Sec. 3.3.

In Fig. 3.6.3(a) the realistic computer rendering of the final buckling configuration for one-half of the pipe is shown. This corresponds to the point E in the moment vs. curvature curve. In Figure 3.6.3(b) a photograph of the test specimen, taken after the test at an orientation of 90 ° from the orientation of Fig. 3.6.3(a), is shown. Comparison of these two pictures indicates that, also for this load case, there is a good correspondence in the behavior between the test and the analytical simulation. For both specimens the final configuration is a one-bulge wrinkle.

Figures 3.6.4 and 3.6.5 show the strain distribution in the circumferential (E11) and the longitudinal (E22) directions, for the outside surface (section point S7 through the thickness). The circumferential strain (E11) is nearly constant and mostly compressive across the surface, reaching values of -1.02% (compression) on the outside surface both along the compression side and the tension side of the pipe. On the wrinkle crest the circumferential strain reaches values of 15.40% (tension). The longitudinal strain (E22) is also nearly constant over the surface, reaching values of 0.67% (tension) on the outside surface along the compression side and 4.48% (tension) along the tension side. On the wrinkle crest the longitudinal strain reaches values of 8.29% (tension). On the wrinkle depression the longitudinal strain reaches values of -41.20% (compression).

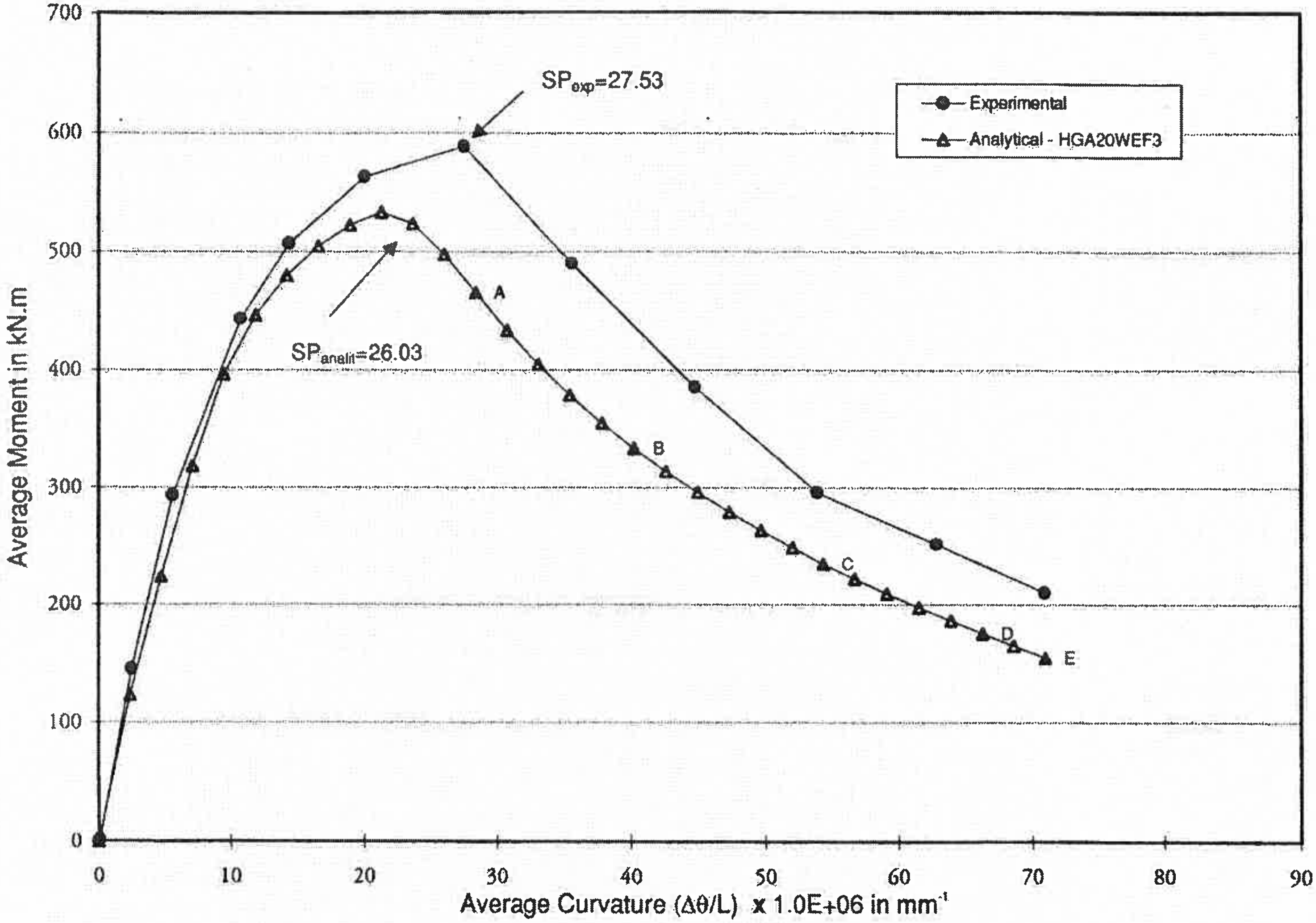

Figure 3.6.1. Average End Moment vs. Curvature for HGA20W pipe

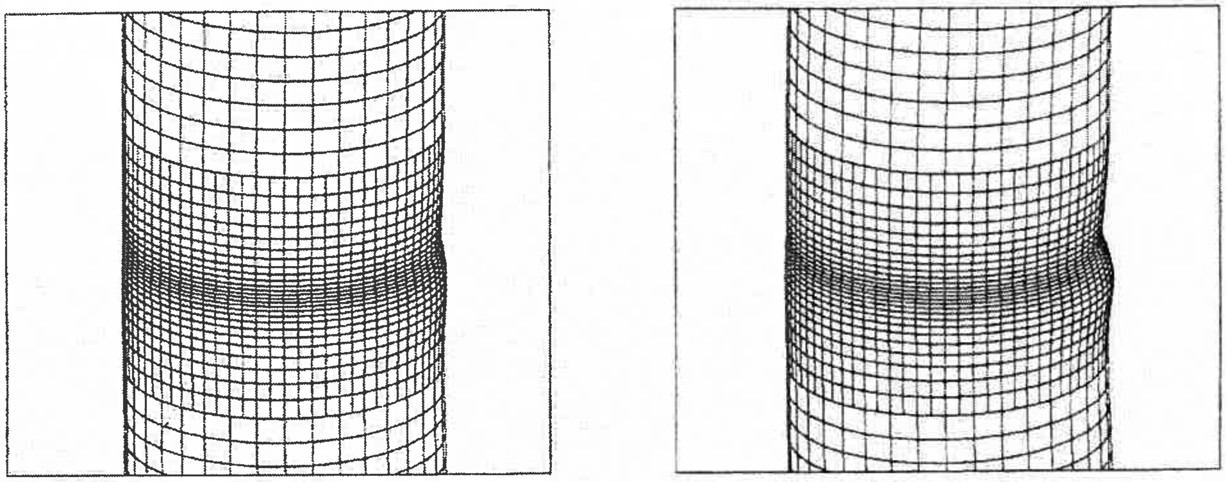

(a) Point A. K = 28.4E-06 /mm. Magnification Factor = 1.0.

(b) Point A. K = 28.4E-06 /mm. Magnification Factor = 2.0.

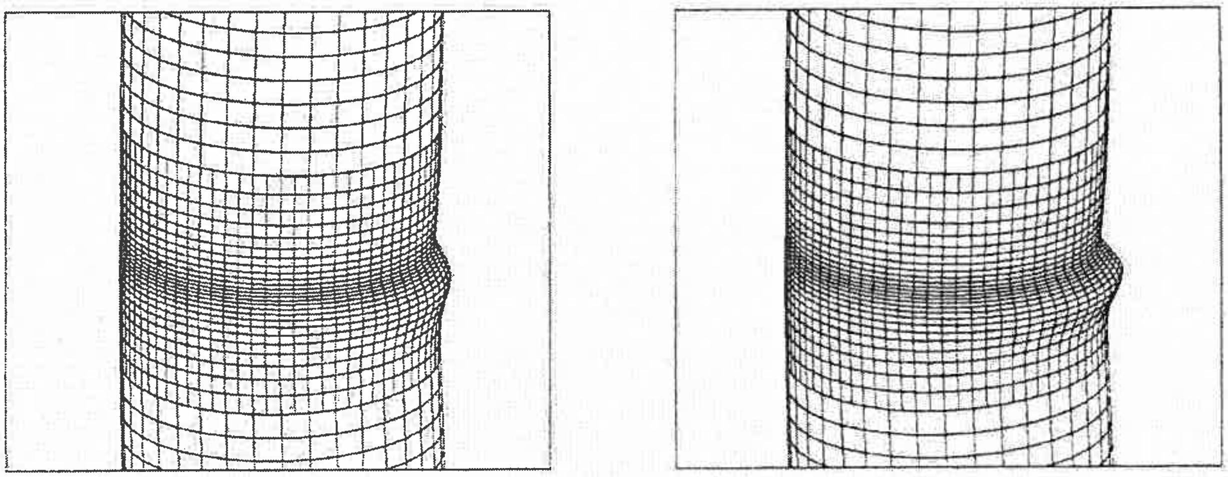

(c) Point B. K = 40.2E-06 /mm. Magnification Factor = 1.0.

(d) Point C. K = 54.4E-06 /mm. Magnification Factor = 1.0.

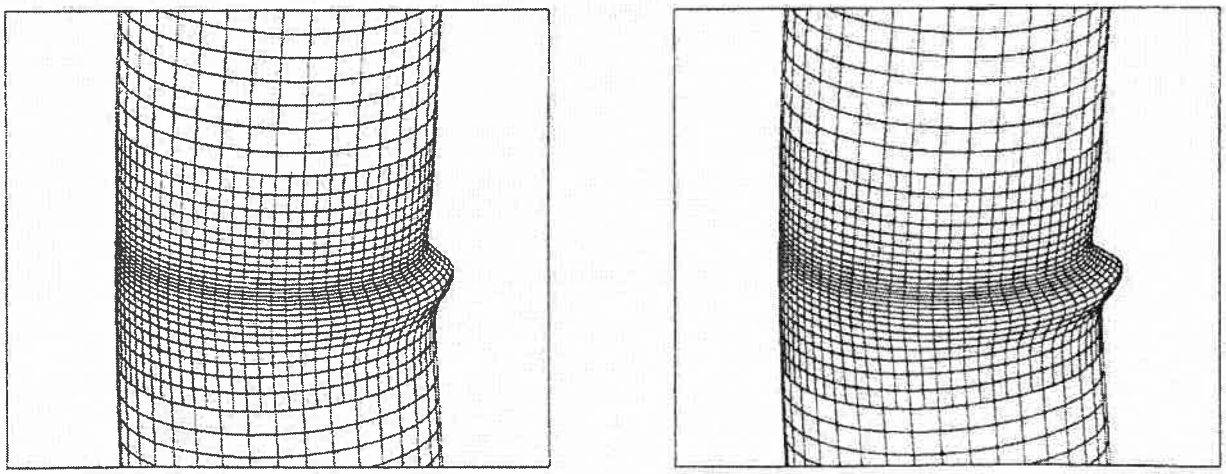

(e) Point D. K = 66.2E-06 /mm. Magnification Factor = 1.0.

(f) Point E. K = 82.8E-06 /mm. Magnification Factor = 1.0.

Figure 3.6.2. Evolution of buckling shape along the end moment vs. curvature (K) curve for specimen HGA20WEF3.

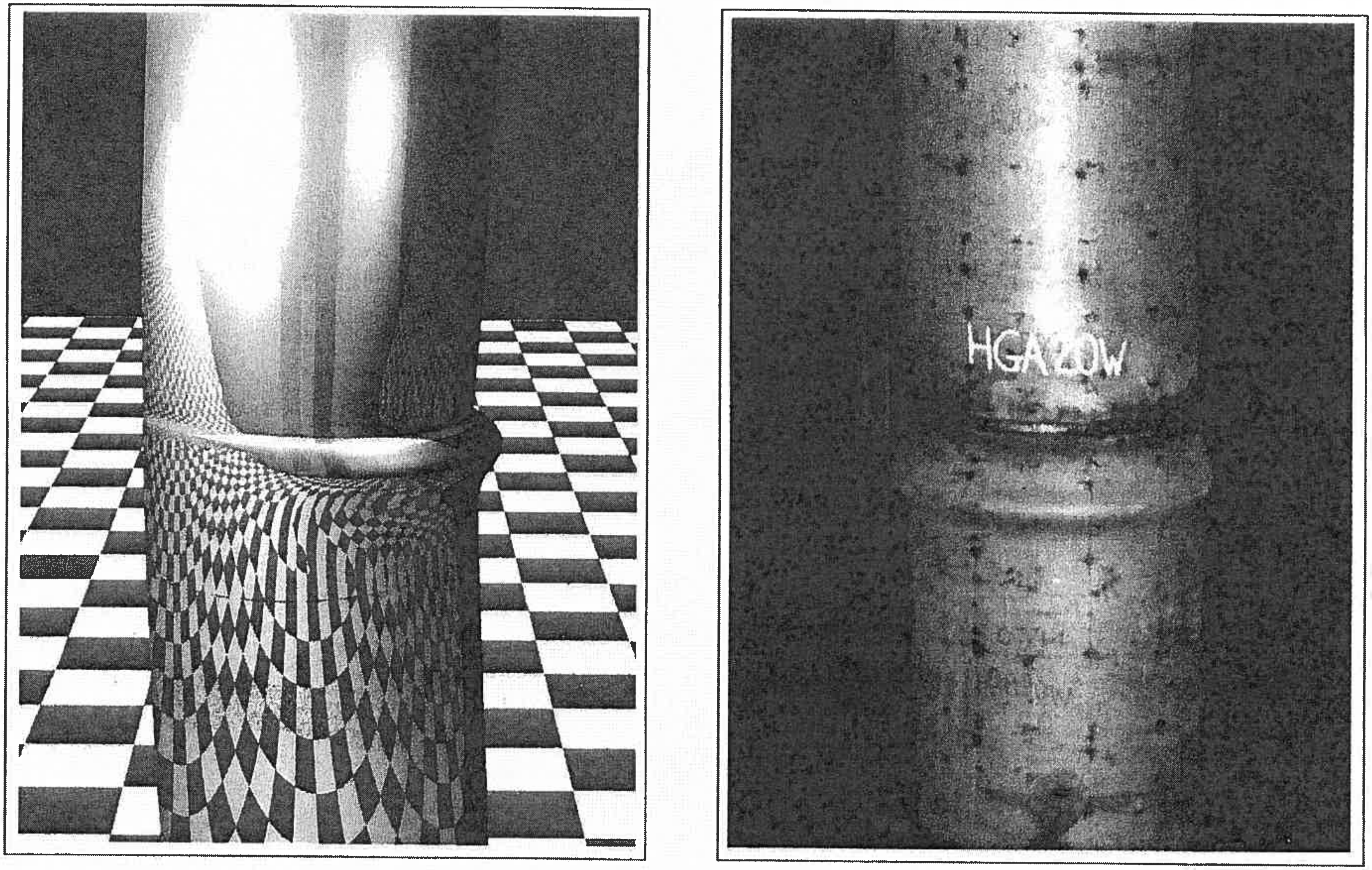

(a) Analytical Results for HGA20WEF3

(b) Experimental Test

Figure 3.6.3. Final Buckling Configuration for HGA20W pipe.

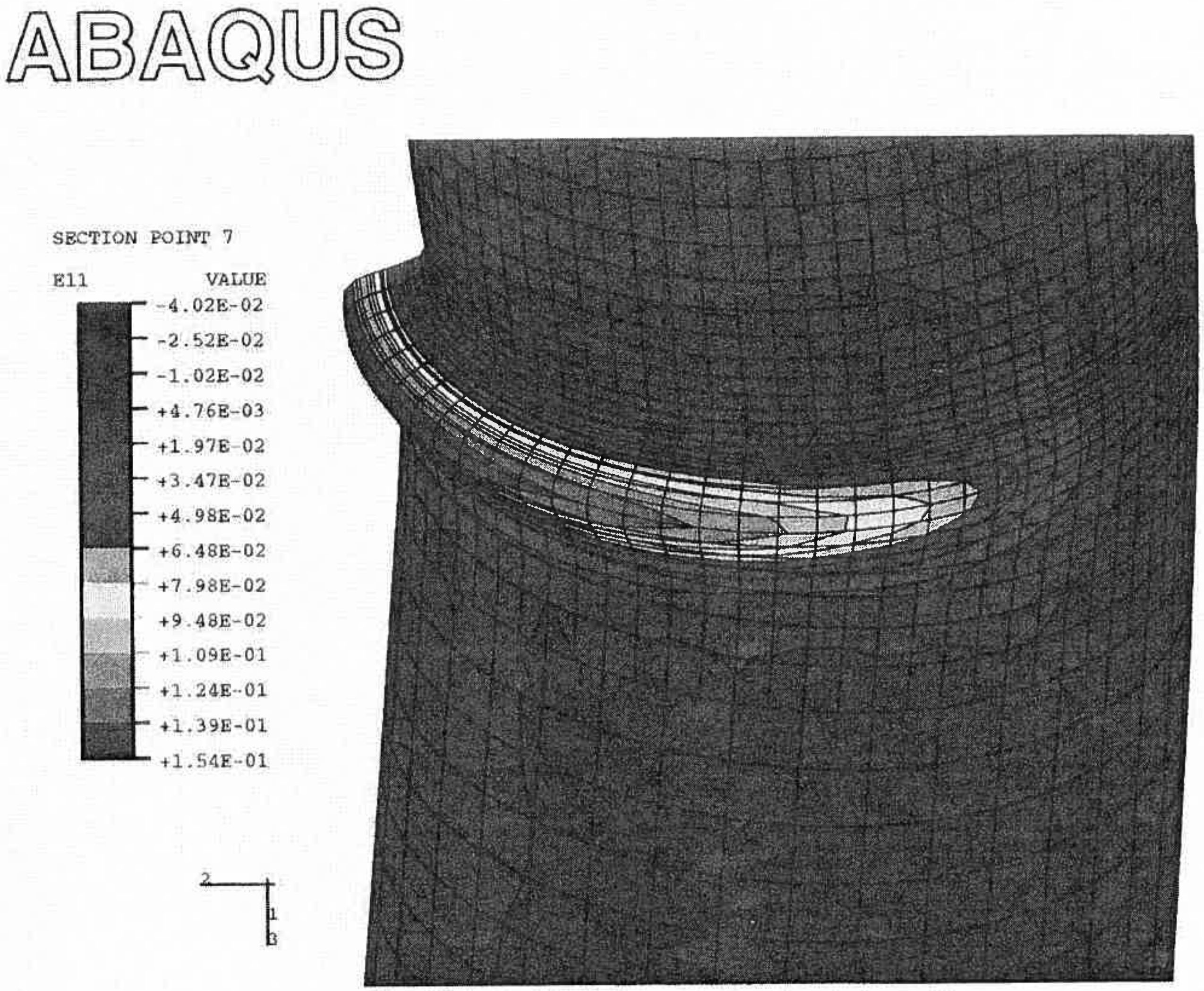

Figure 3.6.4. Circumferential Strain (E11) at Section Point S7 for specimen HGA20WEF3.

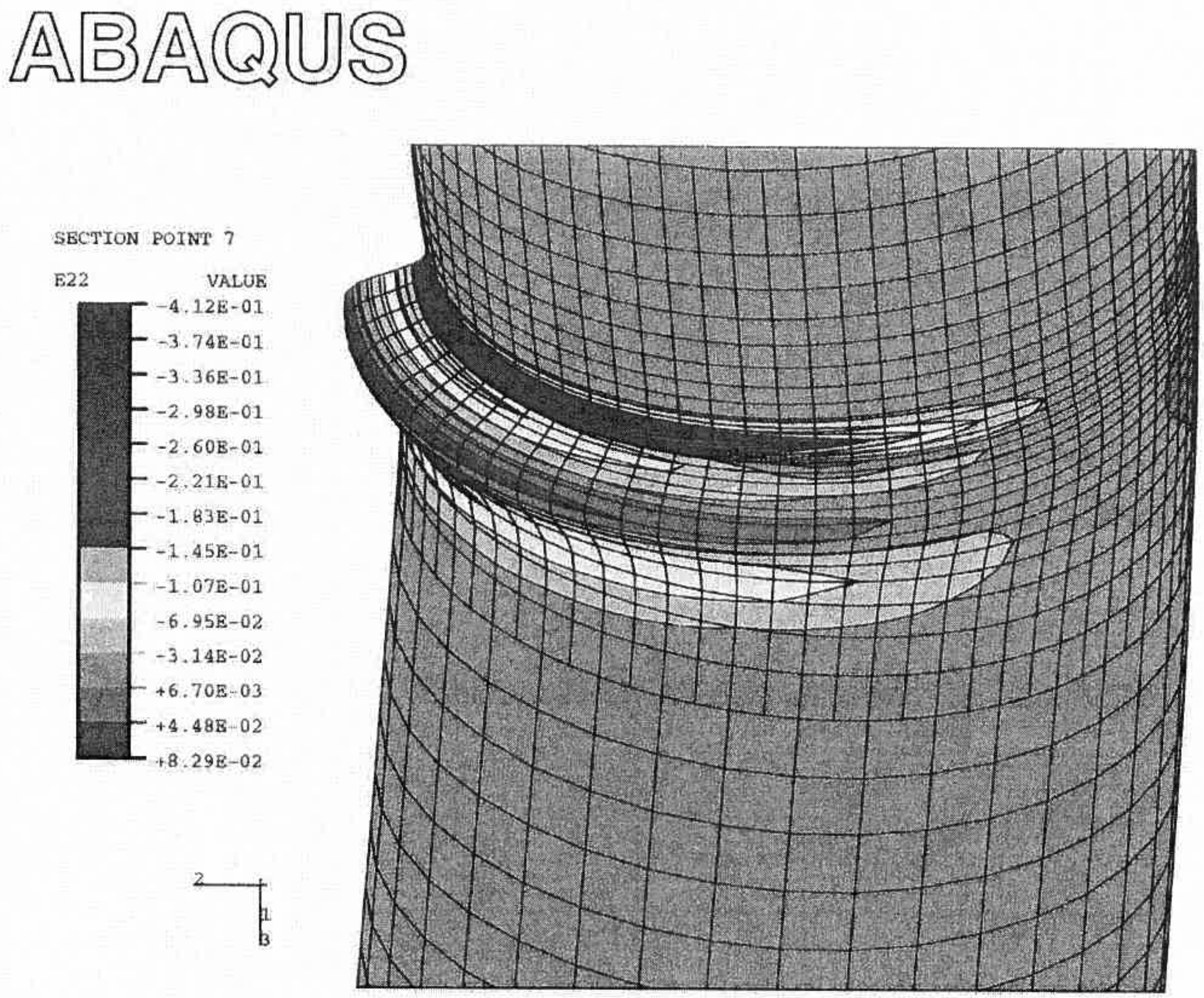

Figure 3.6.5. Longitudinal Strain (E22) at Section Point S7 for specimen HGA20WEF3.

3.7 - SPECIMEN DGA20W

The results for the fully pressurized 20-inch pipe subjected to axial load, internal pressure and imposed moments (rotations) are presented in this section. The analytical results corresponding to the specimen DGA20WEF3 are compared with the ones obtained from the test by Yoosef-Ghodsi, *et al*, (B1994b) defined in Table 1.2.

In Fig. 3.7.1 the average end moment vs. average curvature curve is shown both from the test and the analytical solution. The analytical ultimate resisting moment, which is equal to $\mathbf{M}_{\text{lim}}$ =399.05 kN., is 9.0% lower than the experimental ultimate resisting moment. In a manner similar to specimen DGA12W, the analytical moment vs. curvature curve in this case does not exhibit a distinct softening point but undergoes a gradual softening with the development of a relatively diffuse wrinkle. Again, this appears to be characteristic behavior for the analytical solutions of the local buckling and subsequent wrinkling in highly pressurized pipe. Consequently, the softening point is defined as that point at which the moment has decreased by 5% of the limit value, as discussed in Sect. 3.1. This point corresponds to an average curvature of $\mathbf{K}_{\text{lim}} = 33.13 \times 10^{-6} mm^{-1}$ which is 20.8% lower than the value obtained from the test, where the softening point is identified as the first point in the descending branch of the moment vs. curvature curve.

The evolution of the deformed configuration along the loading history is shown in Fig. 3.7.2 for selected points on the moment vs. curvature curve. The behavior of specimen DGA20WEF3, with D/t = 63, is very similar to the specimen's DGA12WEF3, with D/t = 50, analyzed in Sec. 3.4. It should be noted that, as in the case of specimen DGA12WEF3, the secondary buckle evident in (the lower portion of) Figs. 3.7.2(d) to (f) does not amplify during the development of the wrinkle. On the other hand it also does not disappear as a result of the softening, like the buckle immediately below the weld. This indicates that sufficient plastic deformation occured at this location so that a permanent bulge is retained during subsequent deformation.

In Fig. 3.7.3(a) the realistic computer rendering of the final buckling configuration for one-half of the pipe is shown. This corresponds to the point F in the moment vs. curvature curve. In Figure 3.7.3(b), a photograph of the test specimen, taken after the test at an orientation of 90° from the orientation of Fig. 3.7.3(a), is shown. Comparison of these two pictures indicates there is a reasonable correspondence in the behavior between the test and the analytical simulation even though the wrinkle in the experimental test developed at a location further removed from the girth weld. For both specimens the final configuration contains a one-bulge wrinkle located at some distance from the girth weld.

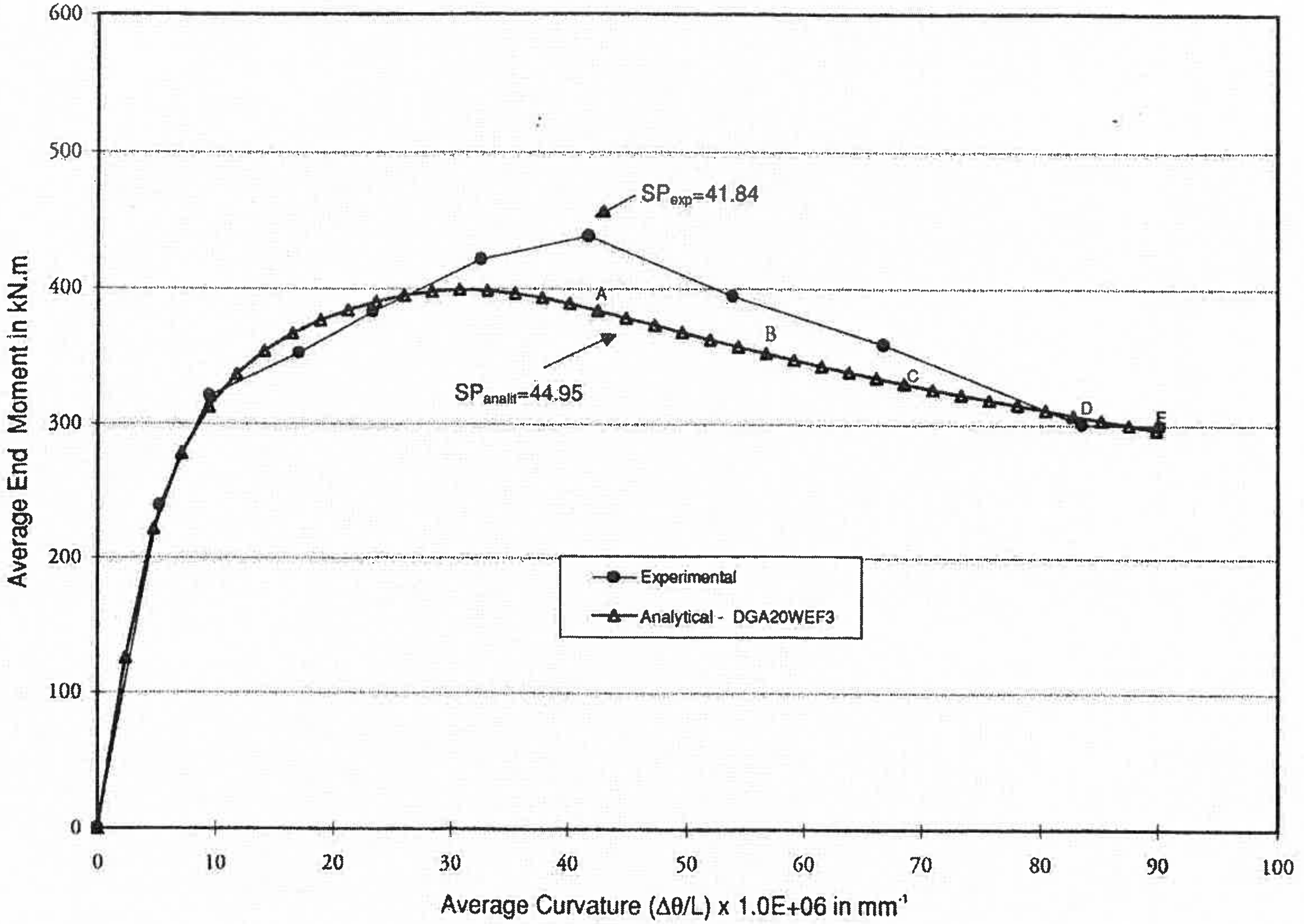

Figure 3.7.1. Average End Moment vs. Curvature for DGA20W pipe

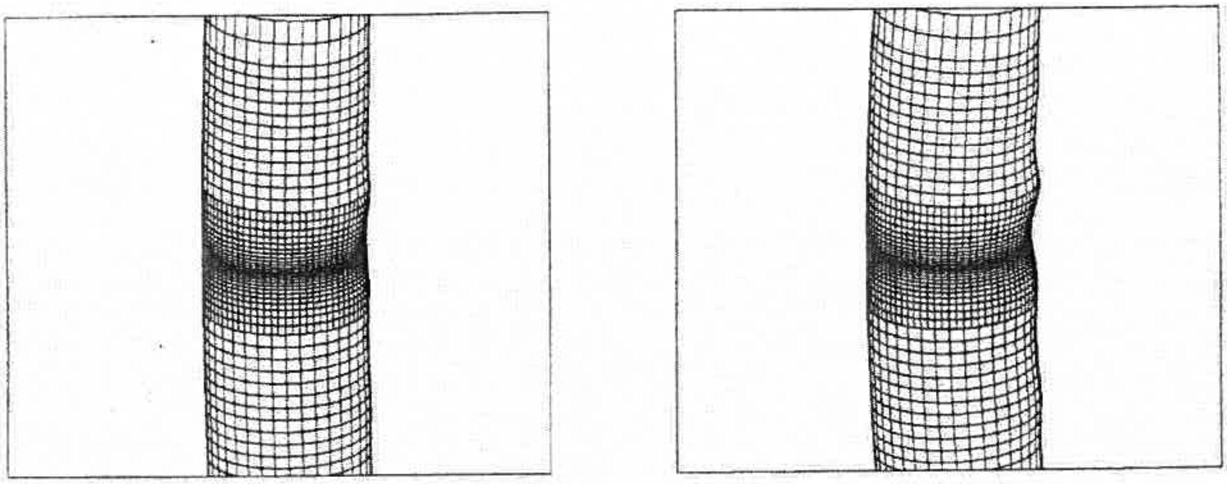

(a) Point A. K = 40.6E-06 /mm. Magnification Factor = 1.0.

(b) Point A. K = 40.6E-06 /mm. Magnification Factor = 2.0.

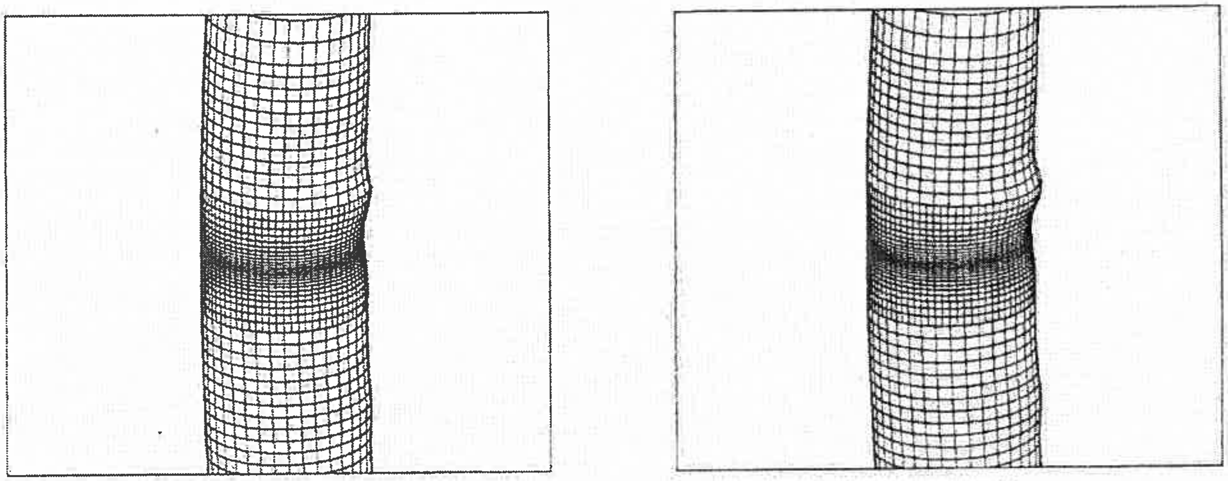

(c) Point B. K = 56.8E-06 /mm. Magnification Factor = 1.0.

(d) Point C. K = 68.6E-06 /mm. Magnification Factor = 1.0.

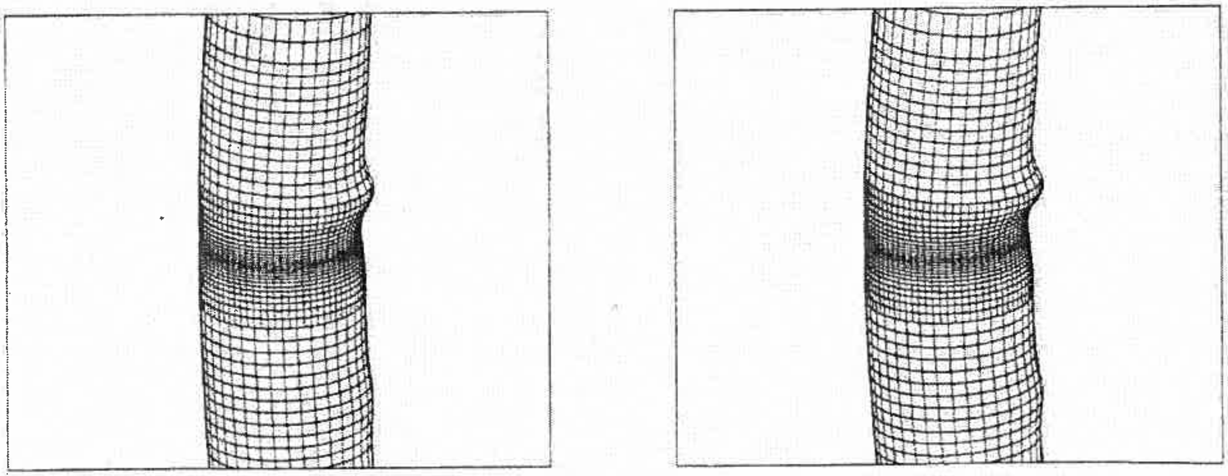

(e) Point D. K = 80.4E-06 /mm. Magnification Factor = 1.0.

(f) Point E. K = 94.6E-06 /mm. Magnification Factor = 1.0.

Figure 3.7.2. Evolution of buckling shape along the end moment vs. curvature (K) curve for specimen DGA20WEF3.

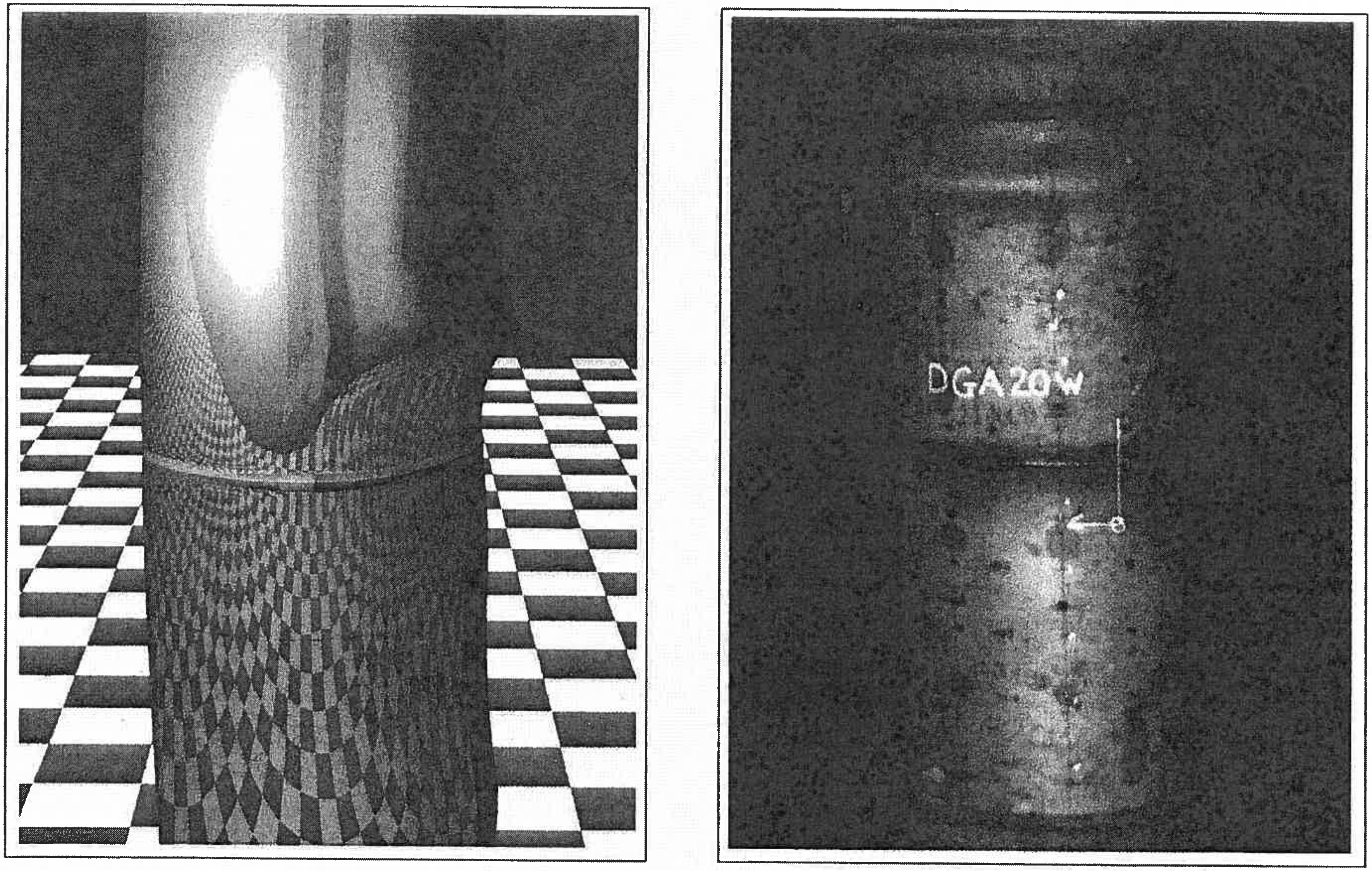

(a) Analytical Results for DGA20WEF3

(b) Experimental Test

Figure 3.7.3. Final Buckling Configuration for DGA20W pipe.

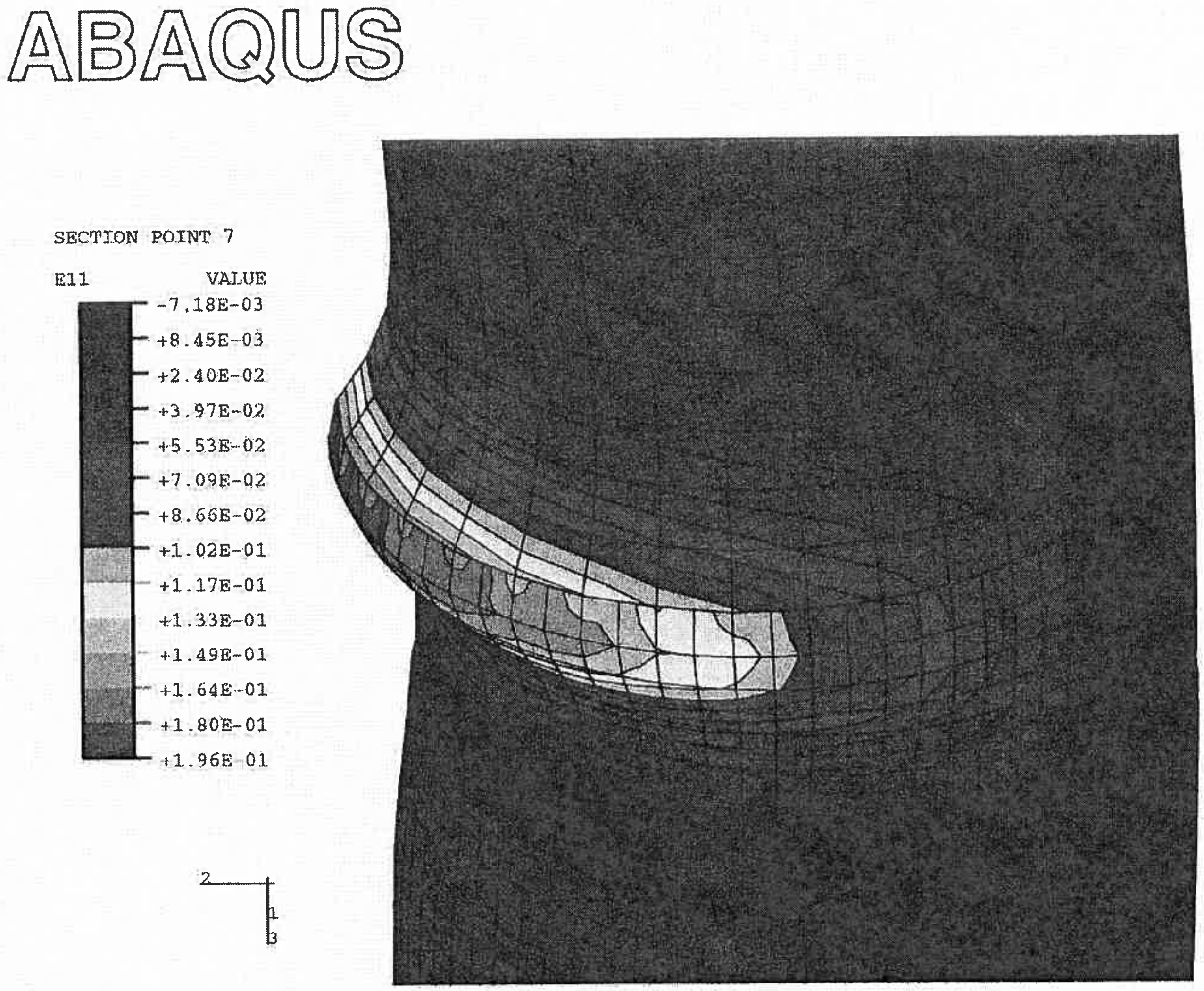

Figure 3.7.4. Circumferential Strain (E11) at Section Point S7 for specimen DGA20WEF3.

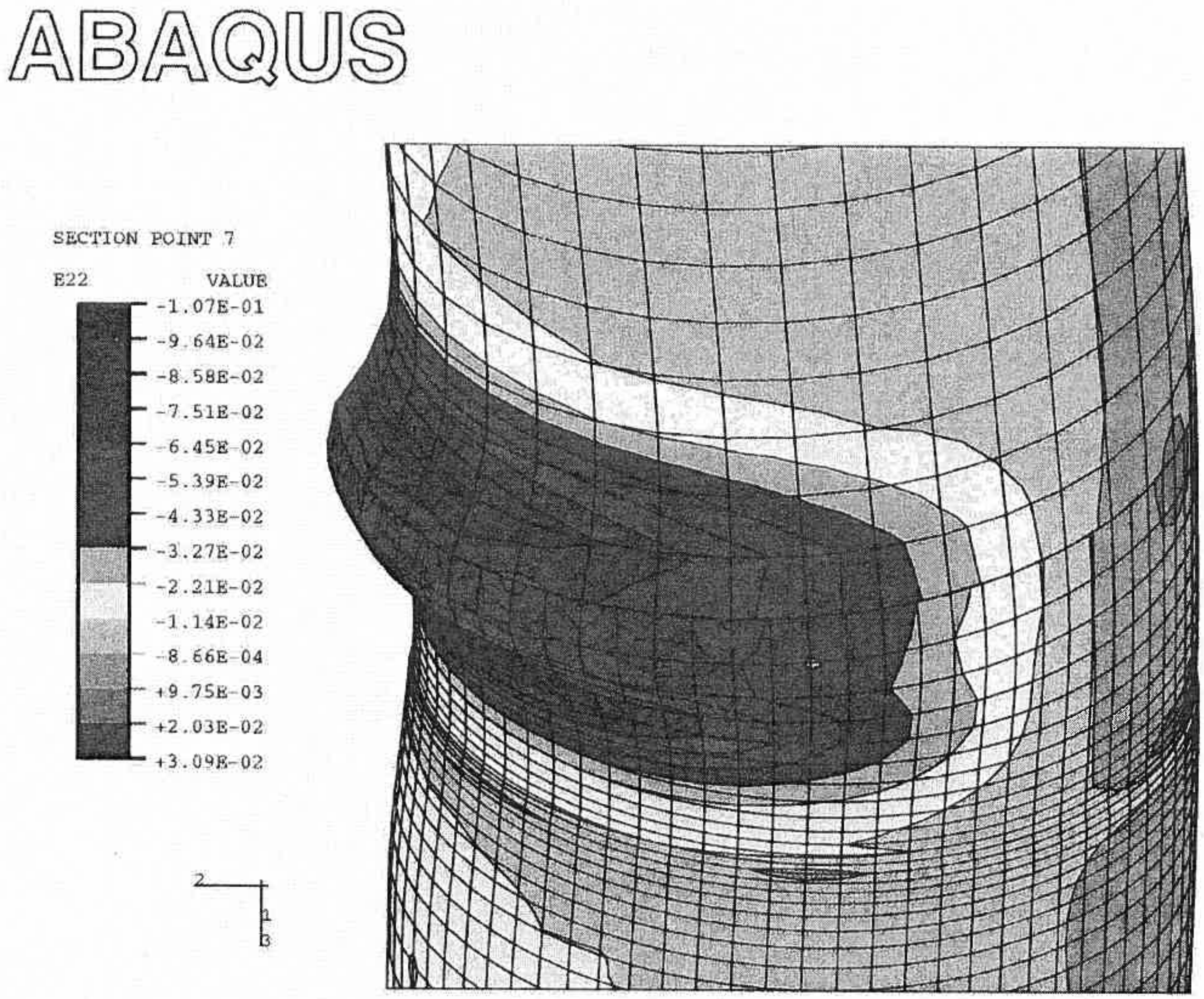

Figure 3.7.5. Longitudinal Strain (E22) at Section Point S7 for specimen DGA20WEF3.

Figures 3.7.4 and 3.7.5 show the strain distribution in the circumferential (E11) and the longitudinal (E22) directions, for the outside surface (section point S7 through the thickness). The circumferential strain distribution (E11) for this specimen, which is similar to the one from specimen DGA12WEF3, varies mostly in the regions where the wrinkles are developed. It reaches values in tension which exceed the yield strain, and whose maximum value is equal to of 19.60% (tension) on the outside surface along the compression side, on the crest of the wrinkle. The longitudinal strain distribution (E22) for this specimen is also similar to the one from specimen DGA12WEF3, reaching values of -10.70% (compression) along the compression side in the neighborhood of the wrinkle and 2.03% (tension) along the tension side.

4.0 CLOSURE TO PART A

The primary purpose for the analyses undertaken in this study is to validate the capability of analytical models employing finite element finite-strain elastic-plastic analysis to realistically predict the behavior of line pipe under the action of various levels of axial loads, various levels of internal pressure, and monotonically increasing curvatures. It was found that, in order to do this for girth-welded pipe, it was necessary to include the residual stress effects that are induced by welding and misalignments at the joint between the two cans. However, if these are properly accounted for the results for the analyses predict:

(a) moments and curvatures for which the moment vs. curvature curves closely resemble those arising from test results;
(b) deformed configurations with buckling and wrinkling patterns that closely resemble those arising from test results; and,
(c) post buckling response that closely resembles that arising in laboratory tests.

It should be noted that behavior, in particular post-buckling behavior, is sensitive to test procedures and alignments and that the experimental responses shown for the various tests are not necessarily unique results. In the present series of girth-welded tests this remark is particularly appropriate to the UGA20W tests for which the test procedure was defective.

The analytical model has shown consistent behavior with the test results for each pipe diameter and load case analyzed. In contrast to plain pipe, considerations of out-of-roundness and offset mismatch play an important role in the correct prediction of buckling modes of girth-welded pipes, being more critical for the unpressurized pipes. The use of finite strain finite elements together with the refined mesh adopted made it possible to incorporate very high localized strains in the wrinkle region and yet reach consistent results. The basis for the selection of the recommended modelling technique that was presented in Sects. 2.1 to 2.5, and by which all of the solutions presented so far have been obtained, will be examined in some detail in Part B. In this latter part of the report the effect of a number of variations in the recommended modelling technique will be examined.

Since the comparison with experimental results from the analyses conducted with the recommended modelling techniques are considered to be sufficiently reliable for design and assessment of pipeline behavior, the techniques developed may be recommended for the production of line pipe behavioral properties that can be included in line of pipe soil-structure interaction analyses such as those by Zhou and Murray (B1993b). Further development of this capability is presently underway.

PART B

ANALYTICAL EXPERIENCE AND INFLUENCE OF MODELLING TECHNIQUE ON SOLUTIONS

5.0. INTRODUCTION TO PART B

In the following sections (i.e. - Part B), some additional solutions are presented which give support to the analytical model that was used throughout Part A. In the finite element modelling of a shell structure, in particular girth-welded pipe subjected to large displacements and large strains in the post-buckling regime, the solution is influenced by several factors, such as, discretization, element type, material modelling, initial imperfections and residual stresses. In Part B solutions, all of these aspects involving the model are addressed, with the exception of the material modelling that has been determined directly from the experimental tests performed by Mohareb, *et al,*, (B1994) and is kept unchanged for all models. As shown in Sec. 2.2 the stress-strain curve does not include the softening region, corresponding to the necking in the uniaxial test. Therefore, localized stresses and strains, that exceed those for the nominal ultimate strength of the material, occuring in the neighborhood of the wrinkles may be only approximately determined in this study.

In Section 6 and 8 the influence of the discretization and the element type on the numerical solution is discussed. The effect of the mesh refinement on the solution, that is necessary to model the girth weld, is investigated. Uniform meshes as well as the experimental results, are used for comparison both in terms of moment vs. curvature relationships and in terms of the buckling shapes. The 4-node finite strain element, which was adopted in the analytical solutions in Part A, is compared with 4-node and 9-node elements based on the hypotheses of large displacement and small strains.

In Section 7 the influence of the initial imperfections, of the type of misalignment at the girth-weld joint, and of the residual stresses at this joint are addressed. Models of perfect pipes, with and without residual stresses, are compared with the models of girth-welded pipes.

In the analytical results presented in Part B an identification system is used that is similar to the one introduced in Table 2.4.2 and adopted for Part A. For plain pipes however a specimen is identified by a string code of the type XGAnnMN. One should note that the characters W and I of the specimen identifier defined in Table 2.4.2 have been omitted because these are related to girth-welded pipes only.

6.0. INFLUENCE OF MESH AND ELEMENT TYPE

6.1. Influence of mesh

In this section the influence of the discretization adopted on the finite element solution is presented. The unpressurized 20-inch plain pipe (UGA20) is modelled using six different meshes, whose characteristics and results are summarized in Table 6.1.1. In half of the specimens from this set (UGA20U1, UGA20U2, and UGA20U3) a uniform mesh was used which consists of equally spaced rows of elements both along the circumferential and the longitudinal directions. The symmetry conditions adopted in Part A (Fig. 2.1.1) apply to all specimens in Part B, except for the specimen UGA20U2. The specimen UGA20U2 is the only one modelled as the full pipe. It contains the same number of elements on each half as specimen UGA20U1. The purpose of this mesh was to check for non-symmetric buckling modes as well as to verify the validity of the boundary conditions on the symmetry plane adopted throughout the study.

The three other specimens from this set (UGA20R1, UGA20R2, UGA20F3) contain a central region with twice the number of longitudinal rows of elements (see Fig. 6.1.1), using multi-point constraints to the nodes adjacent to the common boundaries (Sec. 2.1.6). The purpose of comparing different refinements with uniform meshes is to make sure that the disturbance resulting from the introduction of the refinement does not in itself introduce erratic behavior that might otherwise be attributed to the residual stresses or initial imperfections in the analytical study of the girth-welded pipes. The discretization in the longitudinal direction is different for each of the specimens. The meshes corresponding to specimens UGA20R1 and UGA20R2 have the same number of elements and the same number of degrees of freedom. For the specimen UGA20R1, as shown in Figs. 6.1.1a and 6.1.6, there is a single circumferential row of elements in the middle of the pipe, of width equal to twice the pipe thickness. The remaining of the refined region is subdivided in 8 circumferential rows of elements. For the specimen UGA20R2 on the other hand, as shown in Figs. 6.1.1b and 6.1.7, there are nine circumferential rows of elements in the middle of the pipe, of width equal to twice the pipe thickness. The remaining of the refined region is subdivided in 4 circumferential rows and the size of the refined region along the longitudinal direction for this specimen corresponds to half of the refined region for the previous specimen. The third mesh refinement, which corresponds to specimen UGA20F3, is the one shown in Fig. 2.1.2 that was selected as the standard mesh for all of the analytical studies in Part A. The mesh shown in Fig. 6.1.1c utilizes the same number of nodal points as the standard mesh of Fig. 2.1.2 but the elements shown in Fig. 6.1.1c are nine node elements. Each 9-node element in this mesh coincides with four 4-node elements from UGA20F3. The standard mesh is the only one in its group, for which the 4-node finite strain element is used, and was included in this comparison to establish a reference for the rest of the specimens. For the other meshes, the 9-node element was used.

The unpressurized pipe was selected as the benchmark problem for mesh refinement comparisons because tests show that these specimens should develop a diamond-pattern buckled shape. The diamond-shape pattern is more difficult to predict analytically than bulging modes and, therefore, it is a better test of the adequacy of the mesh. In addition the mesh refinement studies have been carried out on a plain pipe specimen. The reason for this is that it is desirable to separate the influence of the mesh refinement on the solution without introducing additional complicating features associated with modelling the weld or with imperfections. All analytical specimens in this comparison are, therefore, 'perfect' plain pipe specimens.

In Fig. 6.1.2 the average moment vs. average curvature curves are shown corresponding to the analytical solutions obtained using this set of meshes. The experimental curve for plain pipe, obtained by Mohareb, *et al, (B1994),* is also shown. It fits within the spectrum of analytical results but, in the post-buckling range, falls below the curves obtained with uniform meshes. Except for the finite strain result, UGA20F3, the experimental curve in the post-buckling range falls above those obtained with refined meshes. The results for the moment capacity for all analytical specimens fall in the range [0.988M, 1.020M], where M is the maximum moment for specimen UGA20F3, taken as reference. The extreme values for the moment capacity were found to be the lower and upper bounds obtained from the specimens UGA20R1 and UGA20U3, respectively.

In the ascending branch of the average end moment vs. curvature curves shown in Fig. 6.1.2. there is a good agreement for all the meshes included in this group up to an average curvature of 15×10^{-06} /mm . Beyond this point and the limit point for each specimen, the specimens can be split in two groups. The first group consists of the specimens UGA20U3 and UGA20F3, which correspond to the finest uniform mesh using the 9-node element and the best refined mesh using the 4-node finite strain element, respectively. These specimens produce the highest moment capacity. To all the other specimens in this set, the average moment vs. curvature curve is nearly the same up to the limit point. The softening points for all specimens are in the range [0.899 SP, SP], where SP is the softening point for specimen UGA20F3.

The evolution of buckling shape for the various specimens modelling this pipe segment are shown in Figs. 6.1.2 to 6.1.7 and Fig. 7.2.2. All the three uniform meshes produced post-buckling behavior resulting ultimately in diamond-shaped configurations, for which the dimples occur alternatively with respect to the middle of the pipe (Figs. 6.1.3-5). However, these plots were produced using Souza's PostSynas, in which the resulting deformed configuration is plotted taking into account only the displacements at the nodal points (C^0 continuity). Hence there are apparent slope discontinuities in the figures, which do not really occur in the finite element models. These produce the spurious sharp edges evident at the wrinkles in the plots of the deformed configurations. In fact, such discontinuities are present in all of plots of deformed structures in this report (except for the rendered figures) but are more evident in Figs. 6.1.3-5 because the meshes are coarser.

Note that the diamond configurations evolve as a post-buckling phenomenon. The initial local buckles are generally of the bulging type but change configuration to a diamond configuration as the amplitude of the wrinkle increases. Figure 7.2.2 shows an excellent example of this.

As the solution for the full-pipe specimen (UGA20U2) shows (see Fig. 6.1.4), the buckling shape is symmetric about the bending plane, which serves to validate the boundary conditions for the numerical analyses of the models adopted throughout this study. It can also be noticed that the limit point changes only marginally as the number of degrees of freedom is doubled between specimens UGA20U1 and UGA20U3.

The descending branch of the average moment vs. curvature curves for specimens UGA20R1 and UGA20R2 (see Fig. 6.1.2) differ substantially from all the other specimens. This is believed to be a result of the more highly localized buckles (Figs. 6.1.6 and 6.1.7) as a consequence of the mesh refinement adopted in the middle of the pipe. Both specimens failed to predict the expected diamond shape buckling configuration that would be consistent with the experimental behavior, as shown for this specimen in Fig. 6.1.8 (Mohareb, *et al*, B1994b). Despite having the same number of elements and degrees of freedom, the specimens UGA20R1 and UGA20R2 also produced responses which differ substantially from each other.

Generally, both analytical and experimental results show that the more localized the wrinkle, the steeper the softening curve (Mohareb, *et al*, 1994). It should again be emphasized that since all the models under discussion are simulating a plain pipe, the differences observed in Figs. 6.1.2 to 6.1.7 are due only to mesh refinements and change of element type. The deviant behavior for specimens UGA20R1 and UGA20R2 appears to arise solely from the mesh refinement schemes. If these mesh refinements distort the results for plain pipe then they will produce unreliable results for girth-welded pipe as well. The mesh refinement for UGA20F3, of Figs. 2.1.2 and 7.2.2, does not suffer from the deficiencies associated with the meshes of UGA20R1 and UGA20R2. As a consequence of this and the results to be presented in Sect. 6.2, the mesh of UGA20F3 was adopted as the basic mesh for the analysis of girth-welded pipe in Part A.

The solution obtained using the specimens UGA20U1, UGA20U2, UGA20U3 and UGA20F3 (Figs. 6.1.3-5 and 7.2.2) resulted in the proper alternating diamond-shape patterns, displayed by the experimental tests on plain pipe conducted by Mohareb, *et al*, (B1994). The descending branch of the average moment vs. curvature curves for the specimens UGA20U2, UGA20U3 and UGA20F3 tend to a same curve at high average curvatures (of about 80×10^{-06} /mm), when the diamond pattern deformed shape is fully developed. This suggests that the discrepancies evident along the curves between the softening point and the high curvatures is due to the effect of the mesh discretization in the region where the diamond pattern occurs.

From the results presented in this section, and from additional tests performed using other models not included in this report, we can draw the conclusion that generally a mesh influences the buckling shape to a greater extent than it does the limit point and the moment vs. curvature curve. This assumes that the mesh used in the analysis produces an adequately fine discretization of the pipe in order that it can properly represent the configuration to be modelled. It is apparent that abrupt changes in the fineness of the mesh, such as those shown in Fig. 6.1.6 and 6.1.7, disrupt the solution and lead to erroneous results. The mesh shown in Fig. 2.1.2 has given consistent buckling shapes in all load cases tested, both with and without the introduction of girth-weld elements. This is believed to result from the gradual change of element dimensions between adjacent rows, which was achieved through the continuous gradation of the mesh towards the middle of the pipe, unlike the refined meshes presented in this section.

Table 6.1.1

Analytical Models for Comparative Analysis of Unpressurized Plain Pipe Specimens

Specimen	n_θ	n_l	**Number of Elements**	**Number of Nodes**	**Maximum M** (kN.m)	**Curvature at Softening Point** ($\times 10^{-6}$ /mm)
UGA20U1	9	16	144	631	651.27	18.93
UGA20U2	18	16	288	1192	654.59	21.30
UGA20U3	18	18	288	1225	671.14	21.30
UGA20R1	12 (24)	23 (9)	384	1635	652.43	18.93
UGA20R2	12 (24)	23 (13)	384	1635	650.13	18.93
UGA20F3	18 (36)	53 (25)	1440	1535	657.89	21.30

n_θ = number of elements in circumferential direction
n_l = number of elements in longitudinal direction
The numbers between brackets correspond to the number of elements in the refined region.

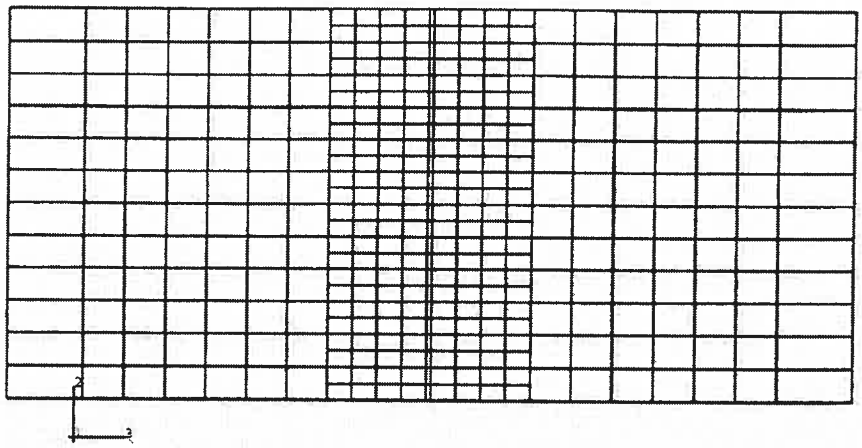

(a) Mesh Refinement #1

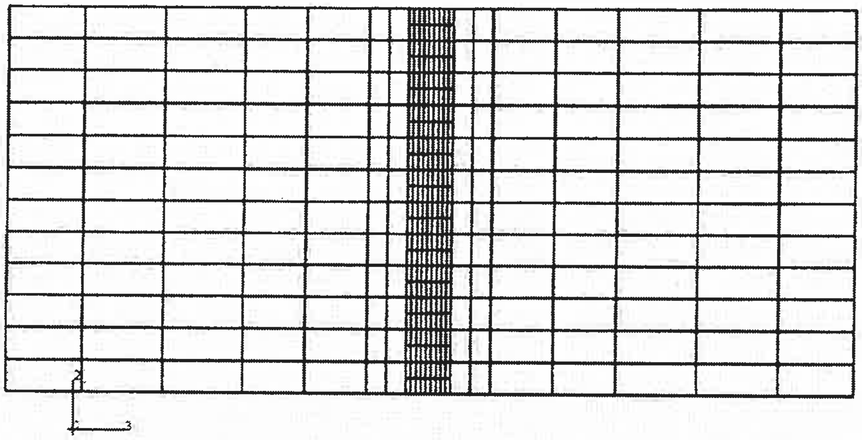

(b) Mesh Refinement #2

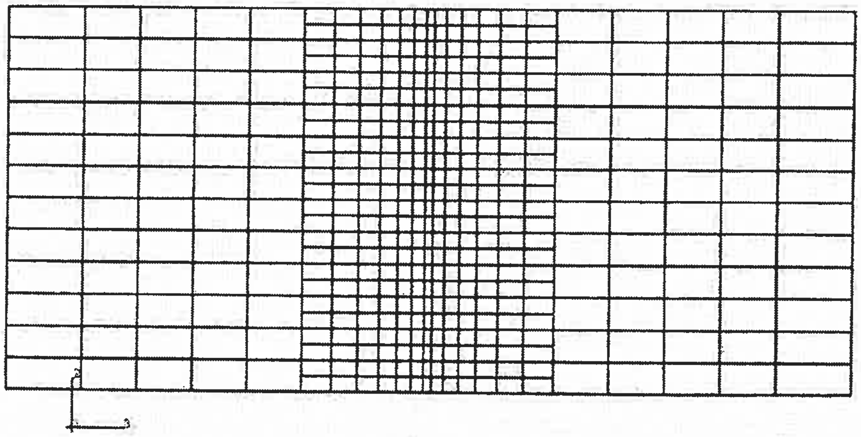

(c) Mesh Refinement #3

Figure 6.1.1.Developed refined meshes.

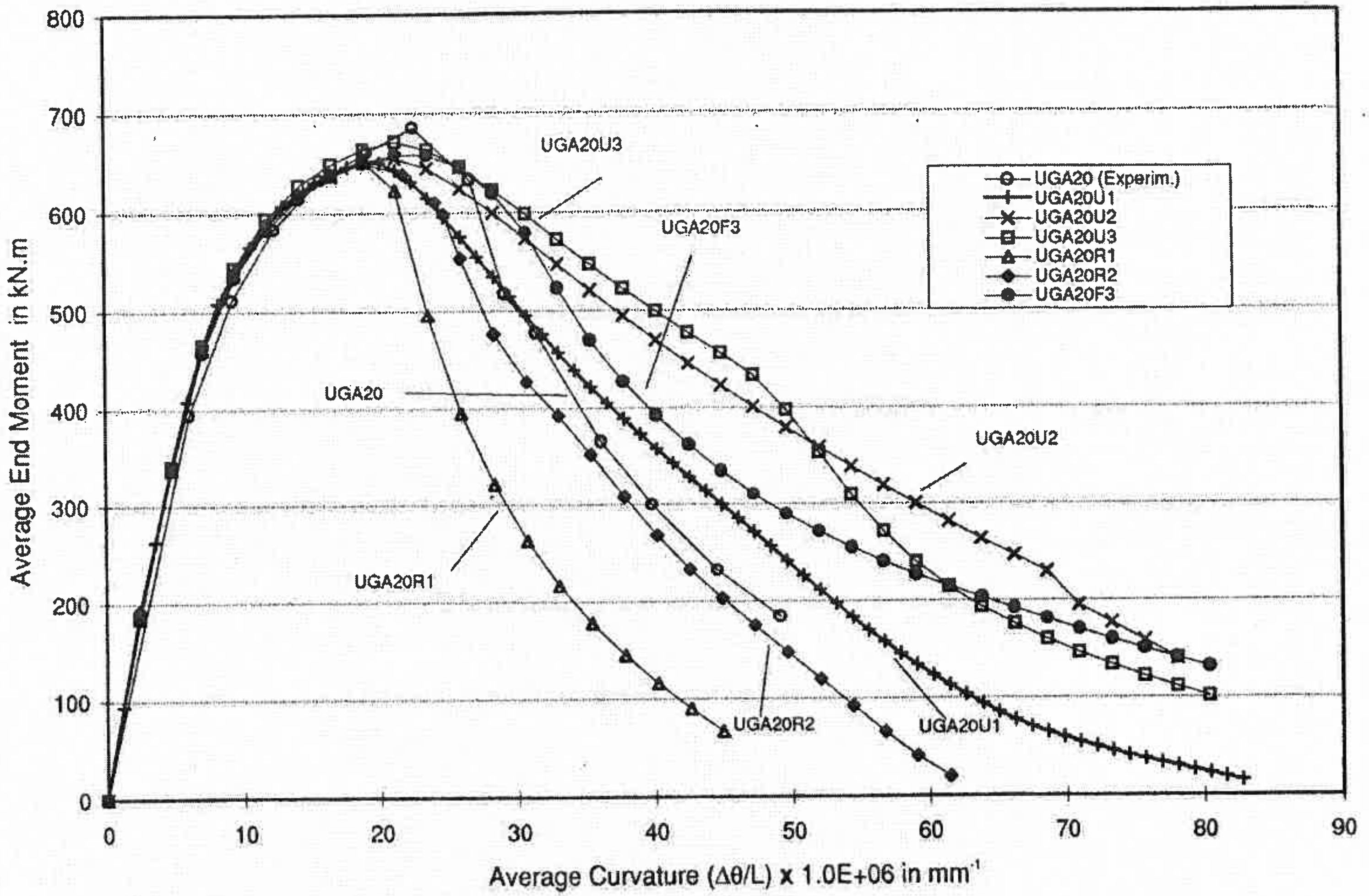

Figure 6.1.2. Influence of the mesh on the moment vs curvature curve for the empty 20-inch plain pipe

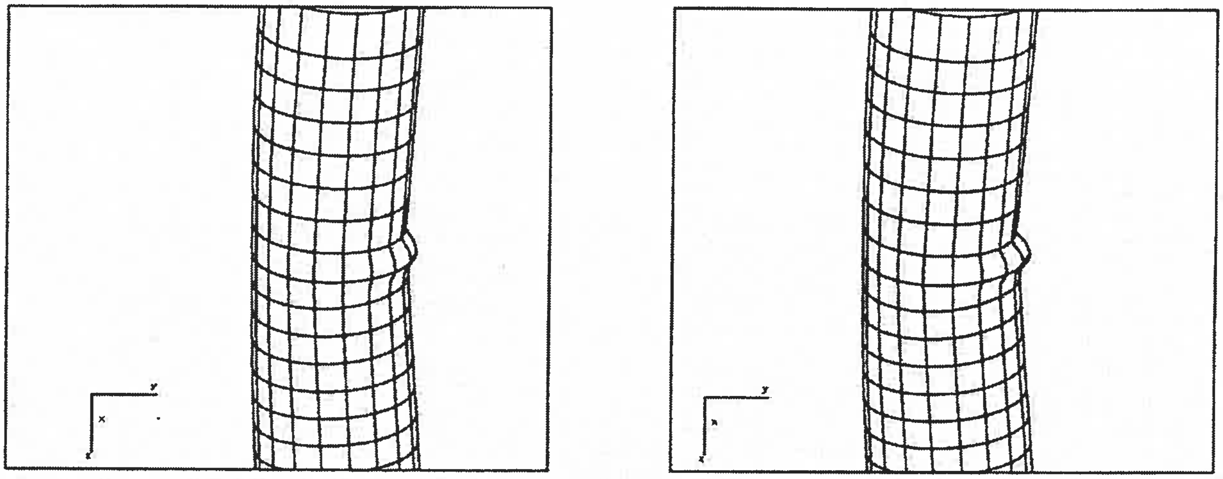

(a) K = 34.32E-06 /mm. Magnification Factor = 2.0.

(b) K = 40.24E-06 /mm. Magnification Factor = 2.0.

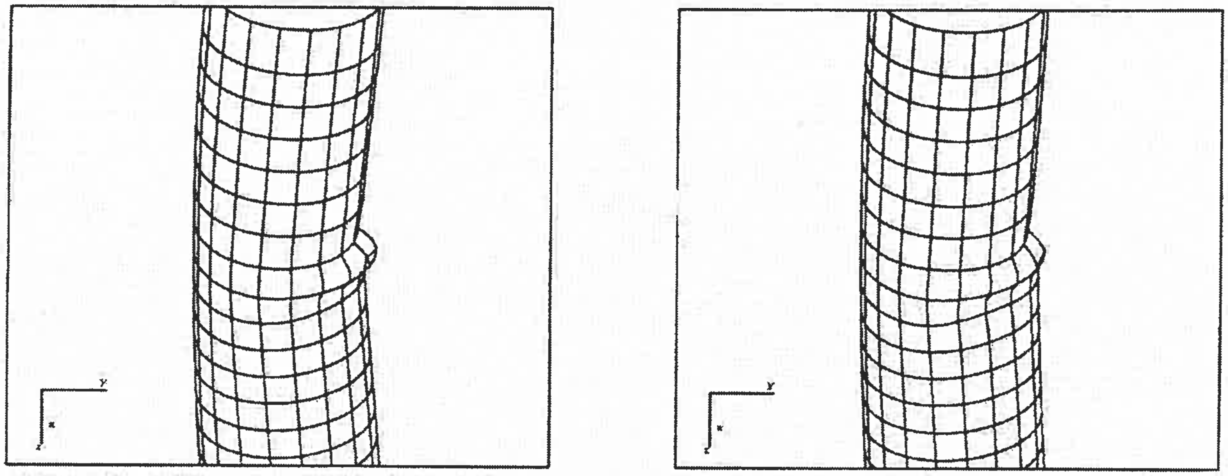

(c) K = 59.17E-06 /mm. Magnification Factor = 2.0.

(d) K = 59.17E-06 /mm. Magnification Factor = 1.0.

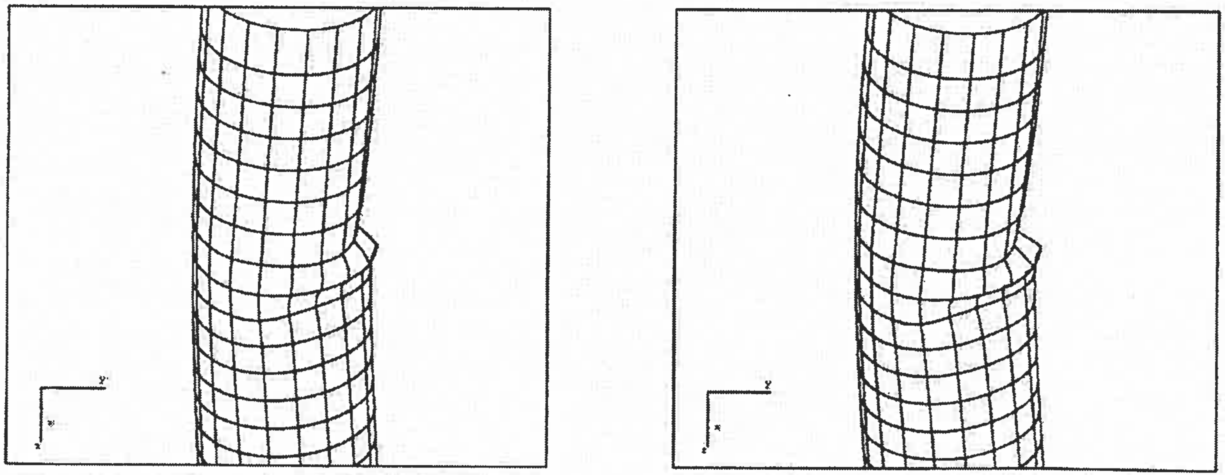

(e) K = 67.46E-06 /mm. Magnification Factor = 1.0.

(f) K = 82.84E-06 /mm. Magnification Factor = 1.0.

Figure 6.1.3. Evolution of buckling shape along the end moment vs. curvature (K) curve for specimen UGA20U1

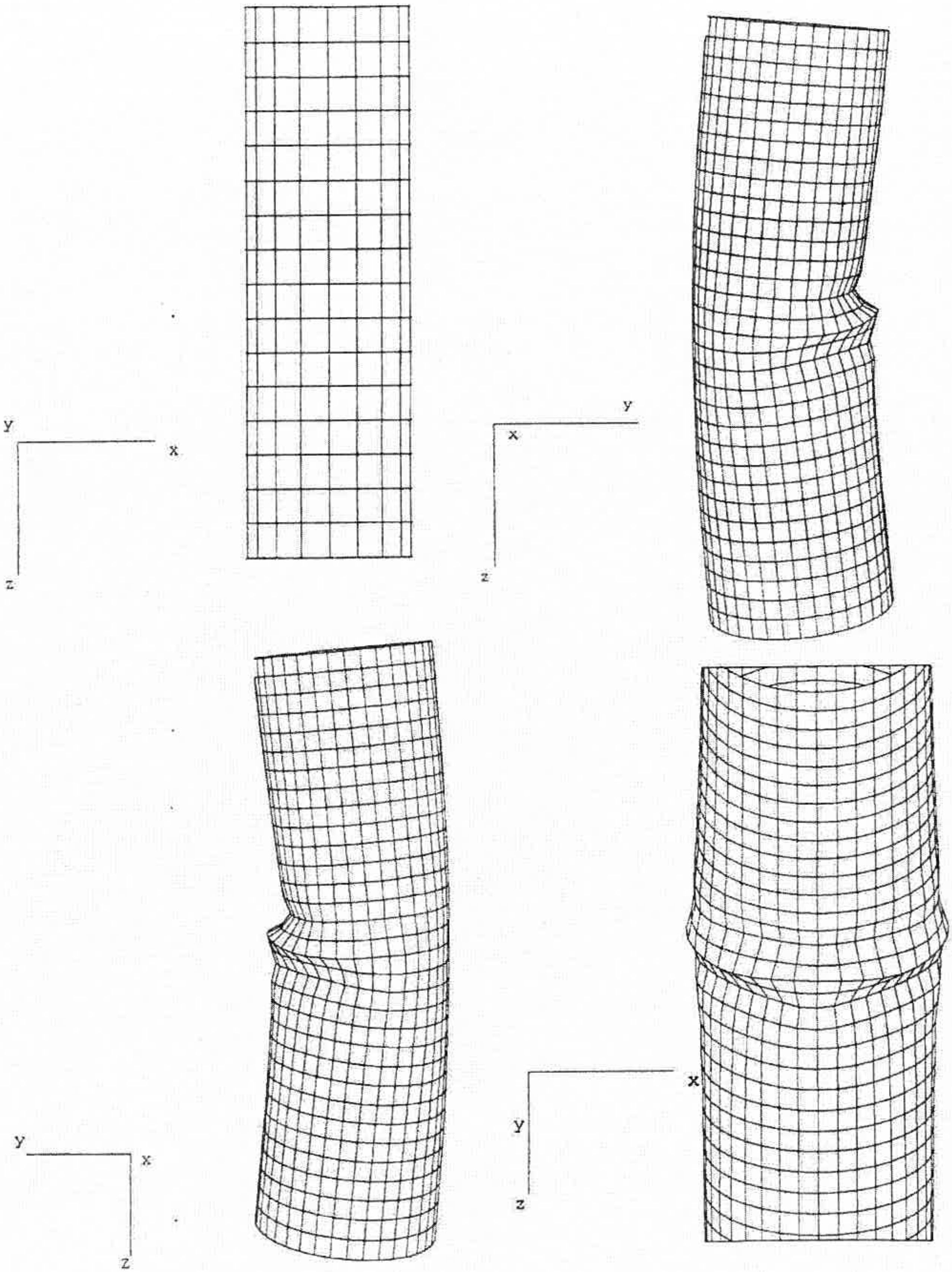

Figure 6.1.4. Mesh and the final buckling shape for specimen UGA20U2

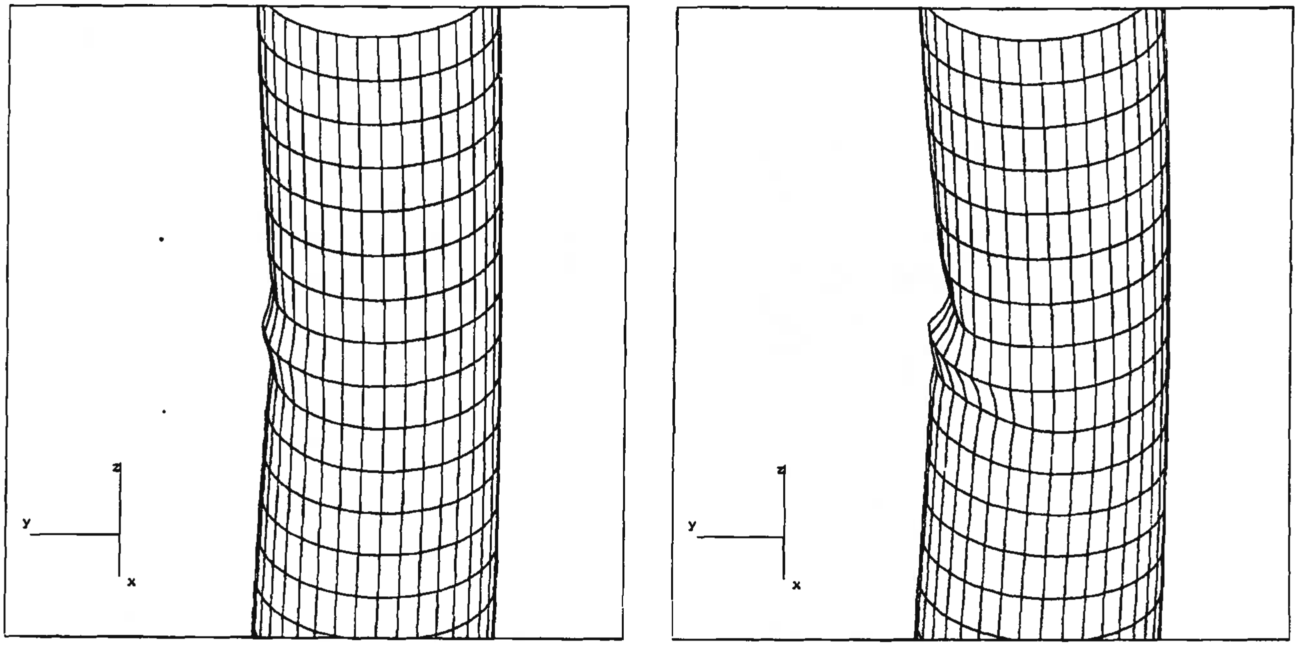

(a) K = 40.24E-06 /mm. Magnification Factor = 1.0.

(b) K = 61.54E-06 /mm. Magnification Factor = 1.0.

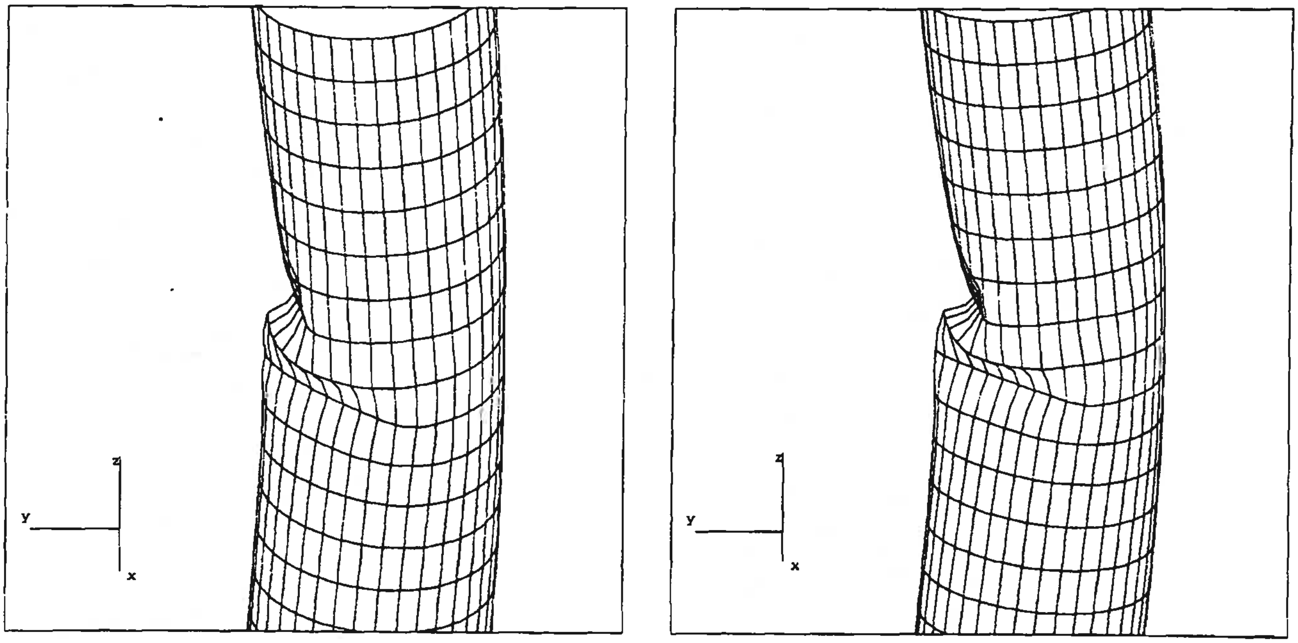

(c) K = 82.84E-06 /mm. Magnification Factor = 1.0.

(d) K = 115.98E-06 /mm. Magnification Factor = 1.0.

Figure 6.1.5. Evolution of buckling shape along the moment vs. curvature (K) curve for specimen UGA20U3

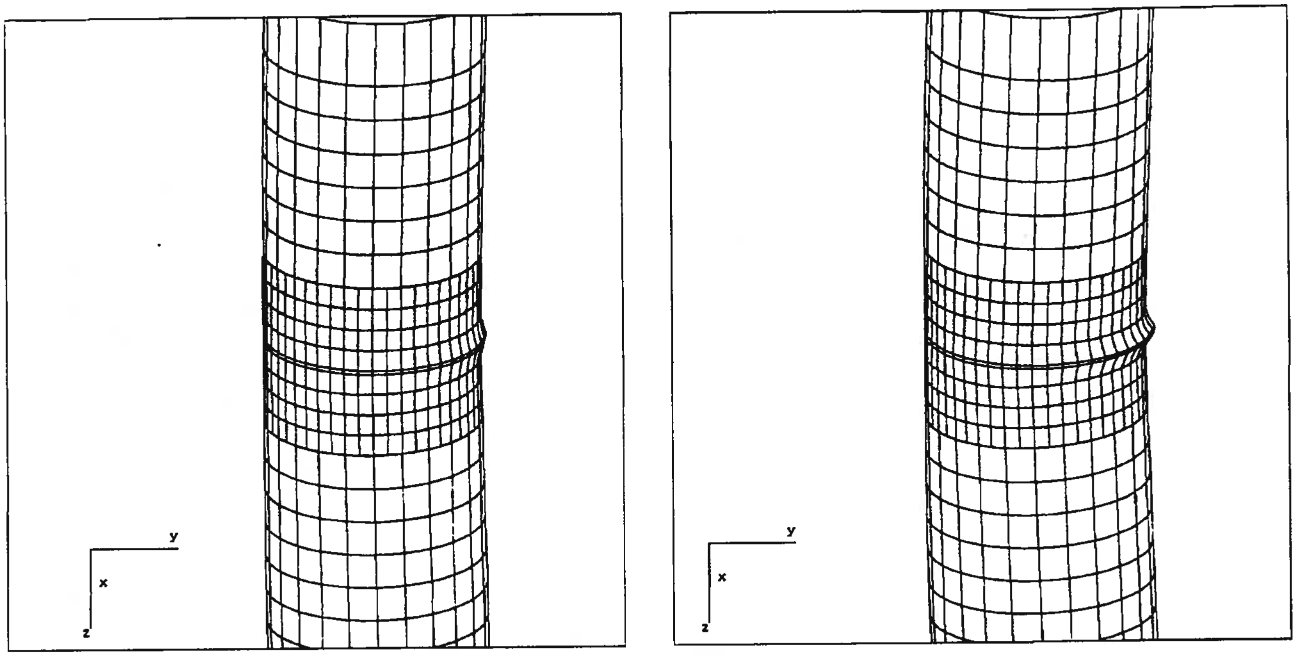

(a) K = 26.04E-06 /mm. Magnification Factor = 1.0.

(b) K = 37.87E-06 /mm. Magnification Factor = 1.0.

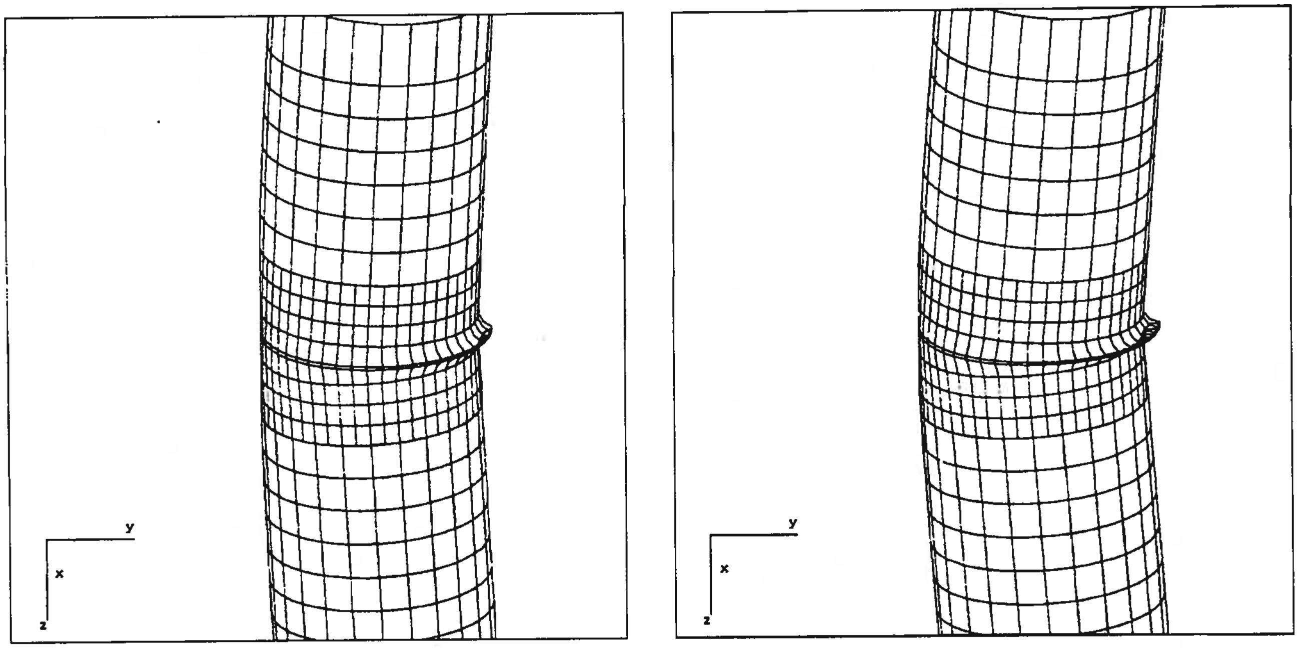

(c) K = 61.54E-06 /mm. Magnification Factor = 1.0.

(d) K = 85.21E-06 /mm. Magnification Factor = 1.0.

Figure 6.1.6. Evolution of buckling shape along the moment vs. curvature (K) curve for specimen UGA20R1

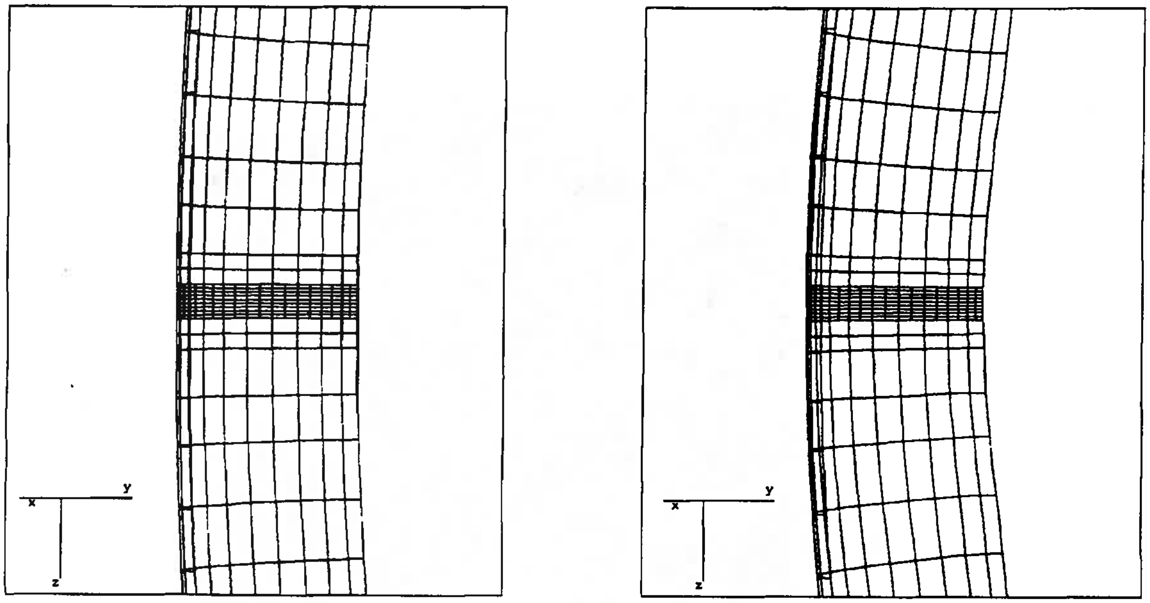

(a) Point A. K = 9.47E-06 /mm. Magnification Factor = 10.0.

(b) Point B. K = 16.5E-06 /mm. Magnification Factor = 10.0.

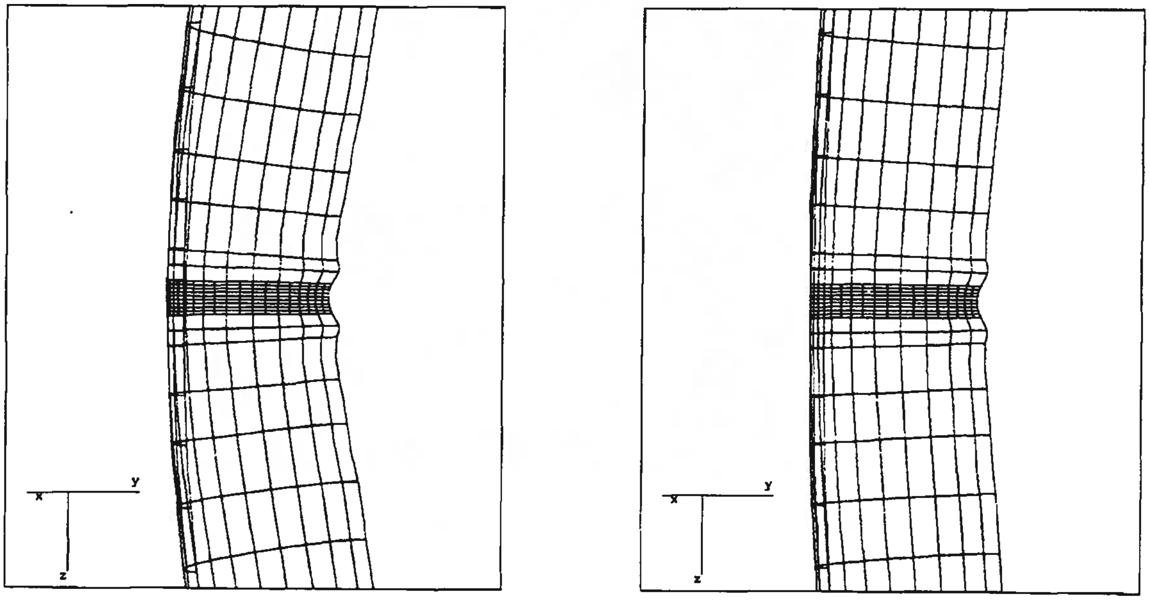

(c) Point C. K = 23.67E-06 /mm. Magnification Factor = 10.0.

(d) Point D. K = 24.85E-06 /mm. Magnification Factor = 4.0.

Figure 6.1.7. Evolution of buckling shape along the end moment vs. curvature (K) curve for specimen UGA20R2

Figure 6.1.8. Final deformed configuration for specimen UGA20 from experimental test.

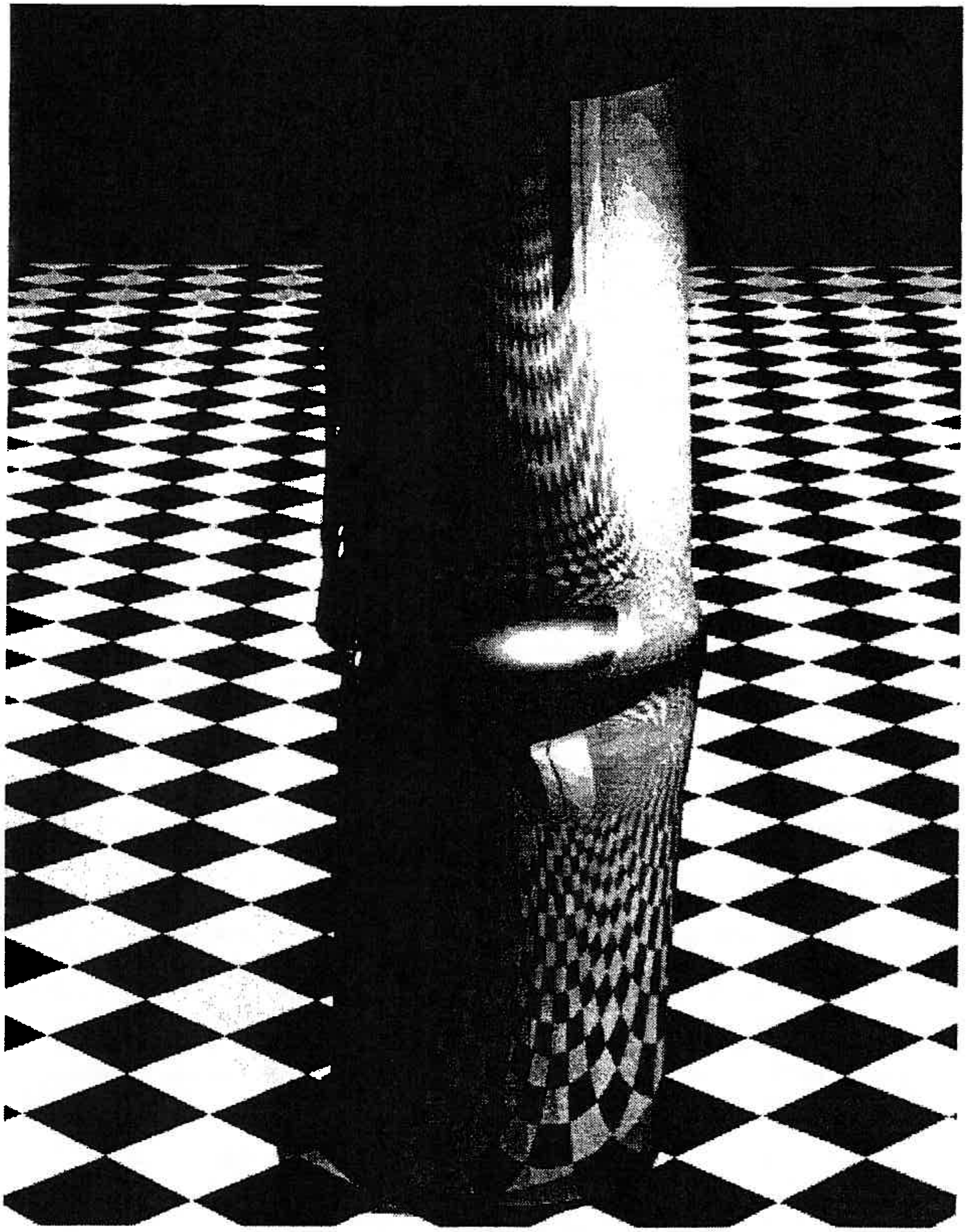

Figure 6.1.9. Final Buckling configuration for specimen UGA20U2

6.2. Influence of the element type

In this section the analytical solutions for the girth-welded 20-inch pipe are compared for two different element types for both the empty pipe (Specimen UGA20W) and the half-pressurized pipe (Specimen HGA20W). For the first case, corresponding to the empty pipe, the solution using the 4-node finite strain element (ABAQUS's S4RF element) is compared with the solution obtained using the 9-node element (ABAQUS's S9R5 element). For the second case, corresponding to the half-pressurized pipe, the solution using the 4-node finite strain element is compared with the solution using the 4-node element based on the hypothesis of large displacements and small strains (ABAQUS's S4R element).

6.2.1. Specimens UGA20W

The characteristics of the meshes and results for the specimens UGA20WEF3 and UGA20WER4 are presented in Table 6.2.1. The average moment vs. average curvature curve for these specimens is shown in Fig. 6.2.1. The solutions obtained using both types of elements are quite similar with respect to the maximum moment, the difference being within 2%. However, the 9-node element (Specimen UGA20WER4) presents a much stiffer behavior . The nearly linear behavior in the ascending branch, results in a softening point at an average curvature equal to 9.46×10^{-6} /mm as opposed to the softening point at an average curvature of 14.20×10^{-6} /mm for the specimen UGA20WEF3. The difference in the response is more noticeable in the descending branch of the moment vs. curvature curves.

The evolution of buckling shape along the moment vs. curvature curve is shown in Figs. 3.5.2 and 6.2.2 for the specimens UGA20WEF3 and UGA20WER4, respectively. There is a steep slope in the descending branch of the moment vs. curvature curve for the specimen UGA20WER4, and it fails to exhibit the diamond-shape buckle. The diamond wrinkle evident in Fig. 3.5.2f extends over a greater length than the bulging wrinkle evident in Fig. 6.2.2, Point D. Generally, the more localized the wrinkle, and the longer the specimen, the steeper is the slope of the softening branch. The fact that Specimen UGA20WER4 does not develop the diamond pattern evident in Fig. 6.1.8, whereas Specimen UGA20WEF3 does evolve into a diamond configuration, implies that the finite strain element produces a better model for predicting wrinkling behavior.

Figures 6.2.3 and 6.2.4 show the strain distribution for the specimen UGA20WER4 corresponding to the final step (average curvature = 86.39×10^{-6} /mm) along the circumferential (E11) and the longitudinal (E22) directions, respectively, for the outside surface (section point S7 through the thickness). The maximum strain magnitude occurred in the circumferential direction where values of 13.50% were reached. These are of the same order as for the strains obtained using the 4-node finite strain element, whose results were discussed in Sec. 3.5.

It should again be noted that the experimental results for Specimens UGA20W are not very reliable because both specimens were inadvertently preloaded and the magnitudes of average curvatures are reconstructed best estimates from the available data (Yoosef-Ghodsi, *et al, 1994)*. Consequently, the reader should not draw strong conclusions from the comparison between experimental and analytical results for the specimens shown in Fig. 6.2.1.

6.2.2. Specimens HGA20W

The characteristics of the meshes and results for the specimens HGA20WEF3 and HGA20WEQ3 are presented in Table 6.2.2. The average moment vs. average curvature curve for these specimens is shown in Fig. 6.2.5. Like the empty pipe presented in the previous section, the solutions obtained using both types of elements are quite similar with respect to the maximum moment, the difference being within 2%. In the ascending branch of the moment vs. curvature curves, both specimens are nearly coincident up to the neighborhood of the limit point. For the specimen HGA20WEQ3, in which the 4-node small strain element is used, the softening point occurs at an average curvature of 21.30×10^{-6} /mm. The softening point is at an average curvature of 26.03×10^{-6} /mm for the specimen HGA20WEF3. As is to be expected The difference in the response is greater in the descending branch of the moment vs. curvature curves than in the ascending branch.

The evolution of deformed shapes along the moment vs. curvature curves are shown in Figs. 3.6.2 and 6.2.6 for the specimens HGA20WEF3 and HGA20WEQ3, respectively. The specimen HGA20WEQ3 buckles as an outward bulge, similar to the experimental test and specimen HGA20WEF3, except that the wrinkle becomes more localized as the rotation is increased. Overall, the solution obtained using the 4-node finite strain element agrees better with the experimental results, both in terms of moment vs. curvature relationship and the deformed shape.

Consequently, the results of the comparisons for solutions utilizing different elements for both the HGA20W specimen (Sect. 6.2.1), and for the UGA20W specimen (Sect. 6.2.2) support the adoption of the finite strain element as the one that gives the most reliable results.

Table 6.2.1
Analytical Models for Investigating Effect of Element Type on Solution for Unpressurized Pipe Specimens

Specimen	Number of Elements	Number of Nodes	Maximum M (kN.m)	Curvature at Softening Point ($\times 10^{-06}$/mm)
UGA20WEF3	1440	1535	527.29	14.20
UGA20WER4	432	1827	538.00	9.46

Table 6.2.2
Analytical Models for Investigating Effect of Element Type on Solution for Half-pressurized Pipe Specimens

Specimen	Number of Elements	Number of Nodes	Maximum M (kN.m)	Curvature at Softening Point ($\times 10^{-06}$/mm)
HGA20WEF3	1440	1535	533.25	26.03
HGA20WEQ3	1440	1535	523.19	21.30

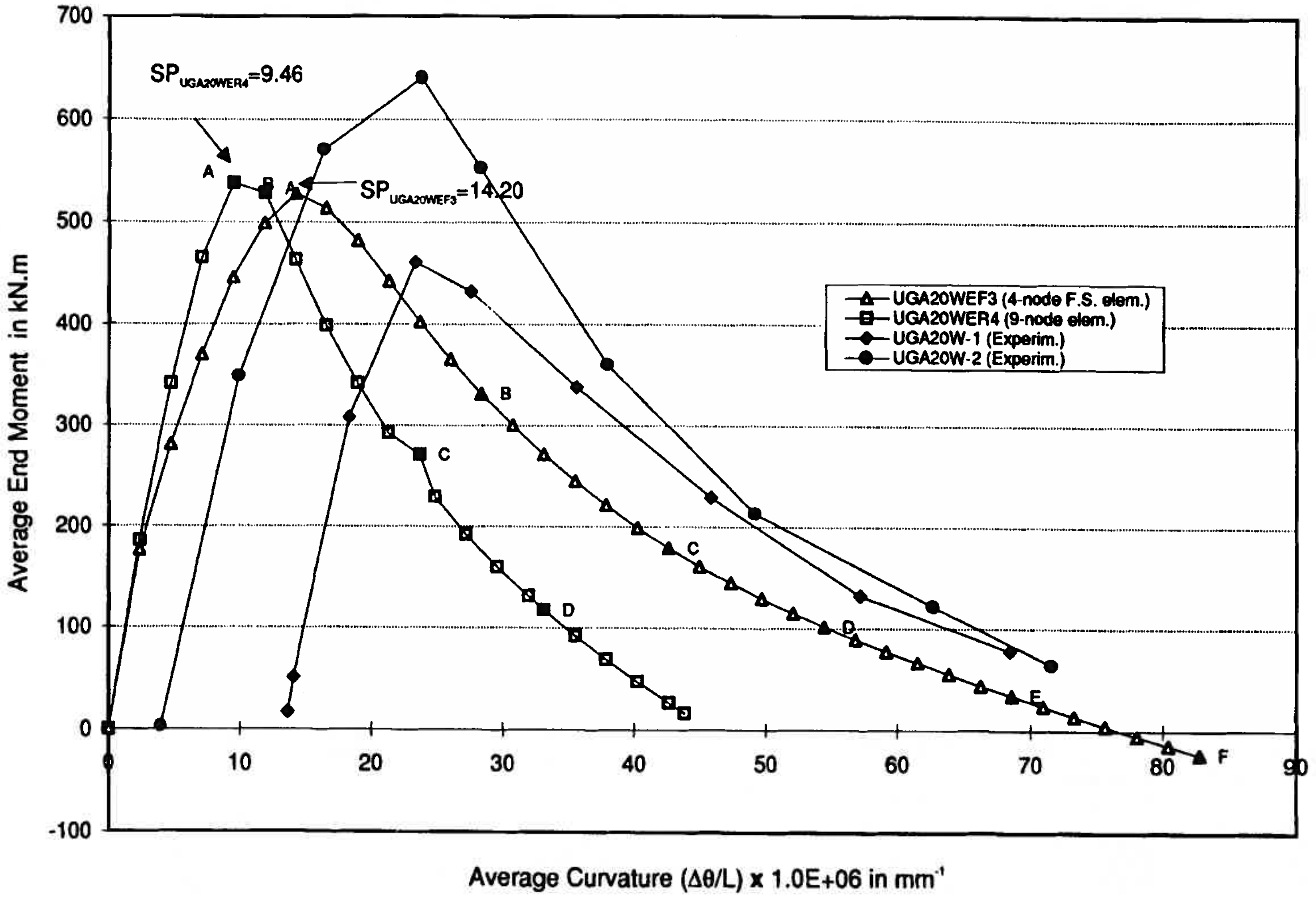

Figure 6.2.1. Effect of the element type for the empty 20-inch pipe

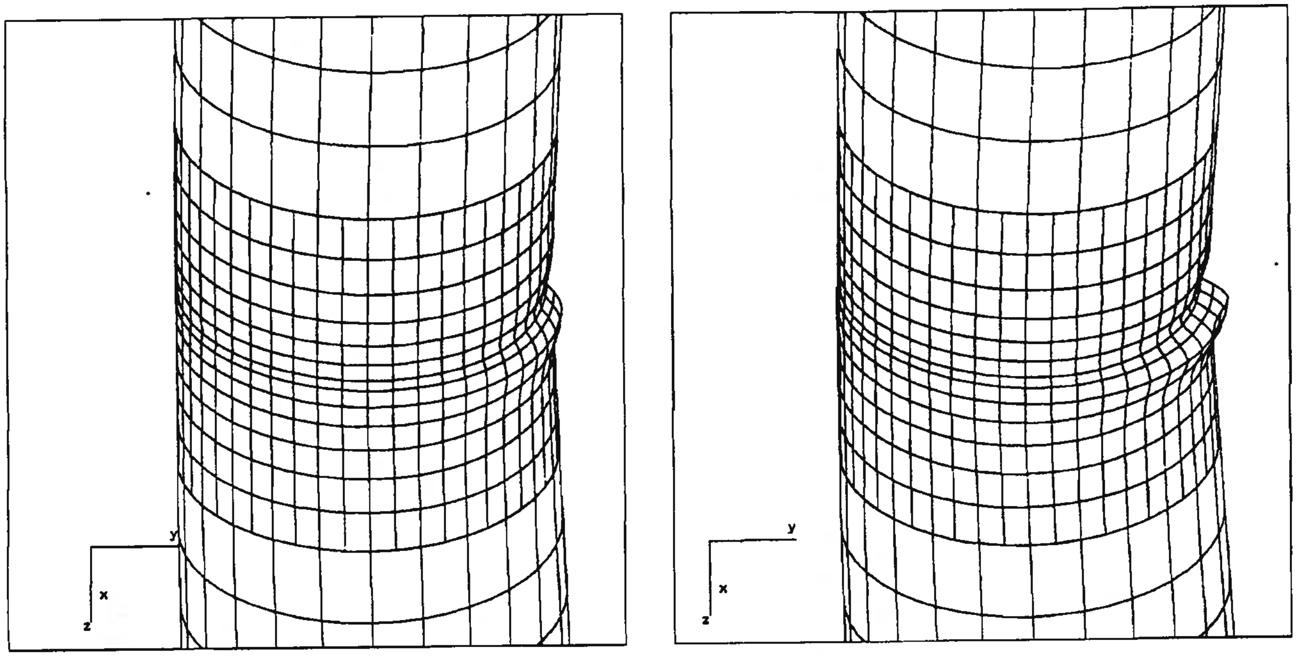

Point A. K = 9.47E-06/mm. Magnification Factor = 4.0.

Point B. K = 11.84E-06 /mm. Magnification Factor = 4.0.

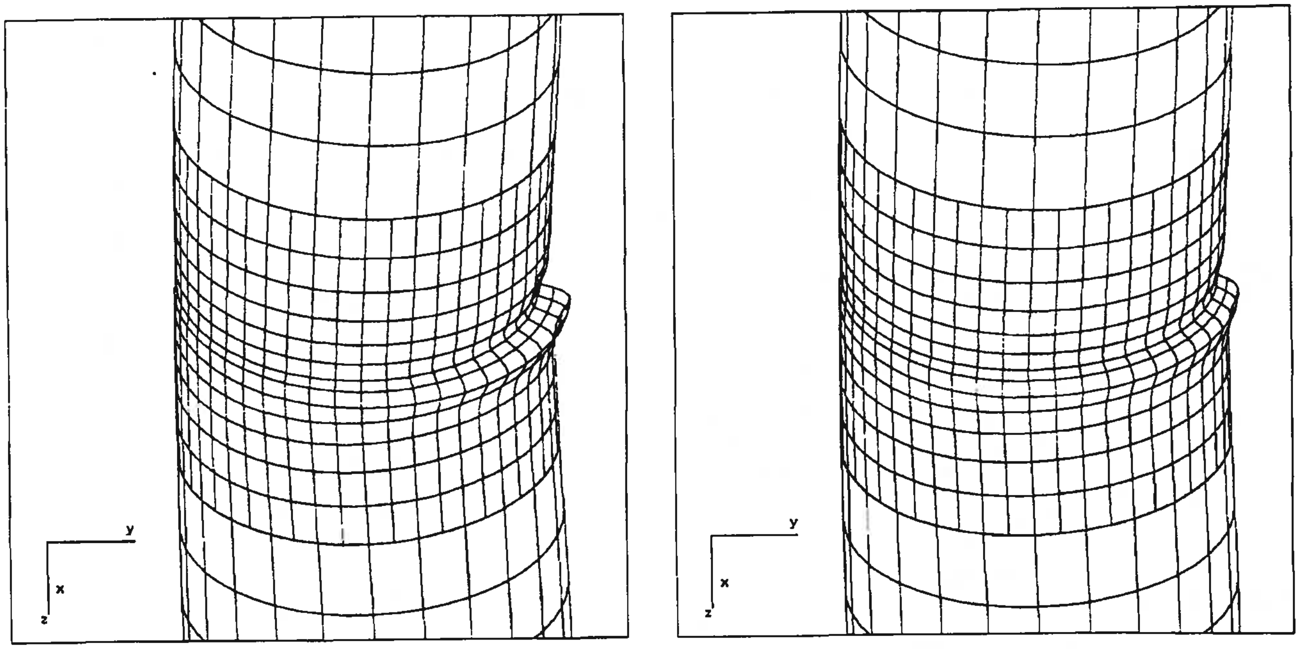

Point C. K = 23.19E-06 /mm. Magnification Factor = 2.0.

Point D. K = 33.84E-06 /mm. Magnification Factor = 1.0.

Figure 6.2.2. Evolution of buckling shape along the end moment vs. curvature (K) curve for specimen UGA20WER

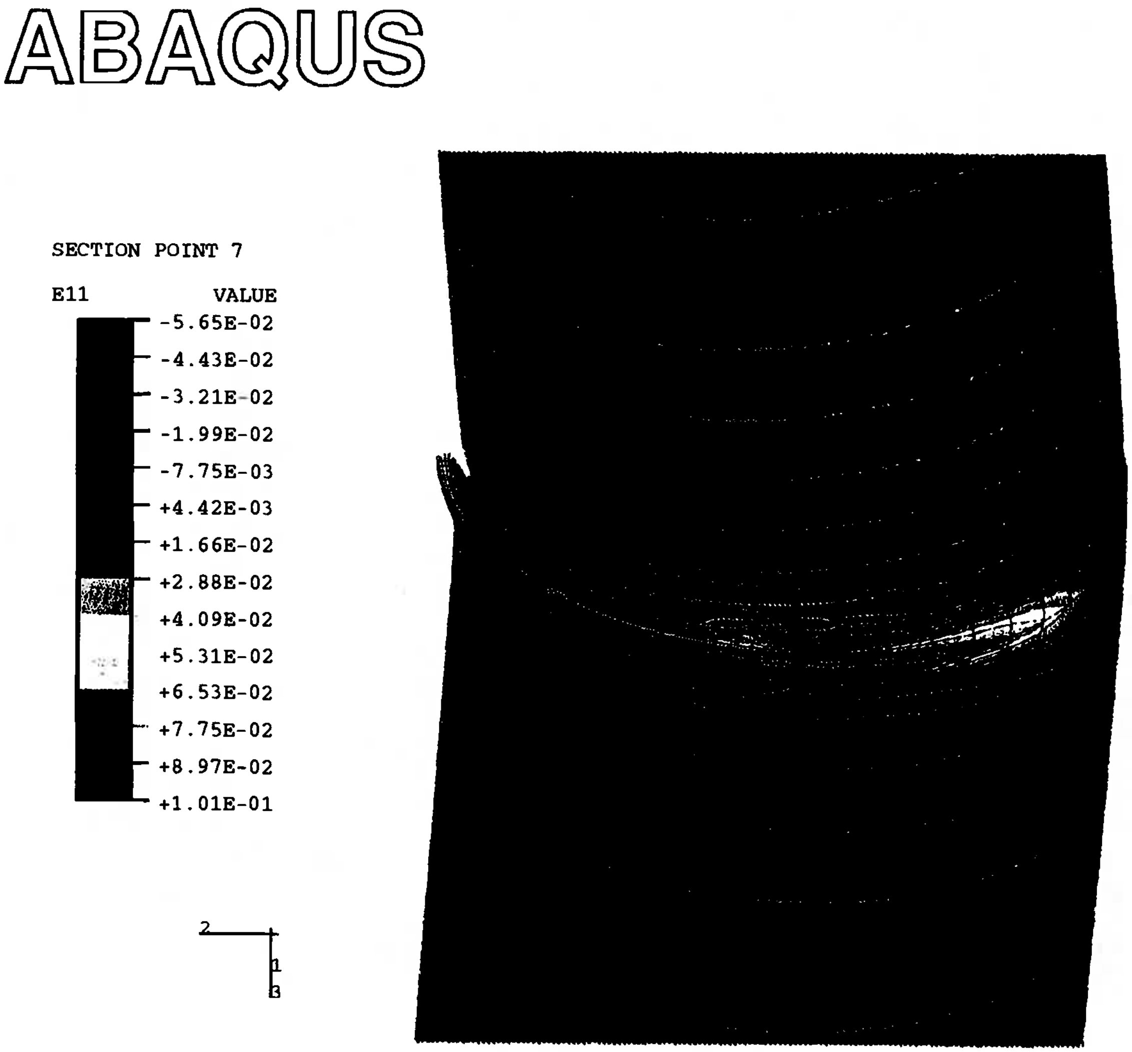

Figure 6.2.3. Circumferential Strain (E11) at Section Point S7 for specimen UGA20WER4.

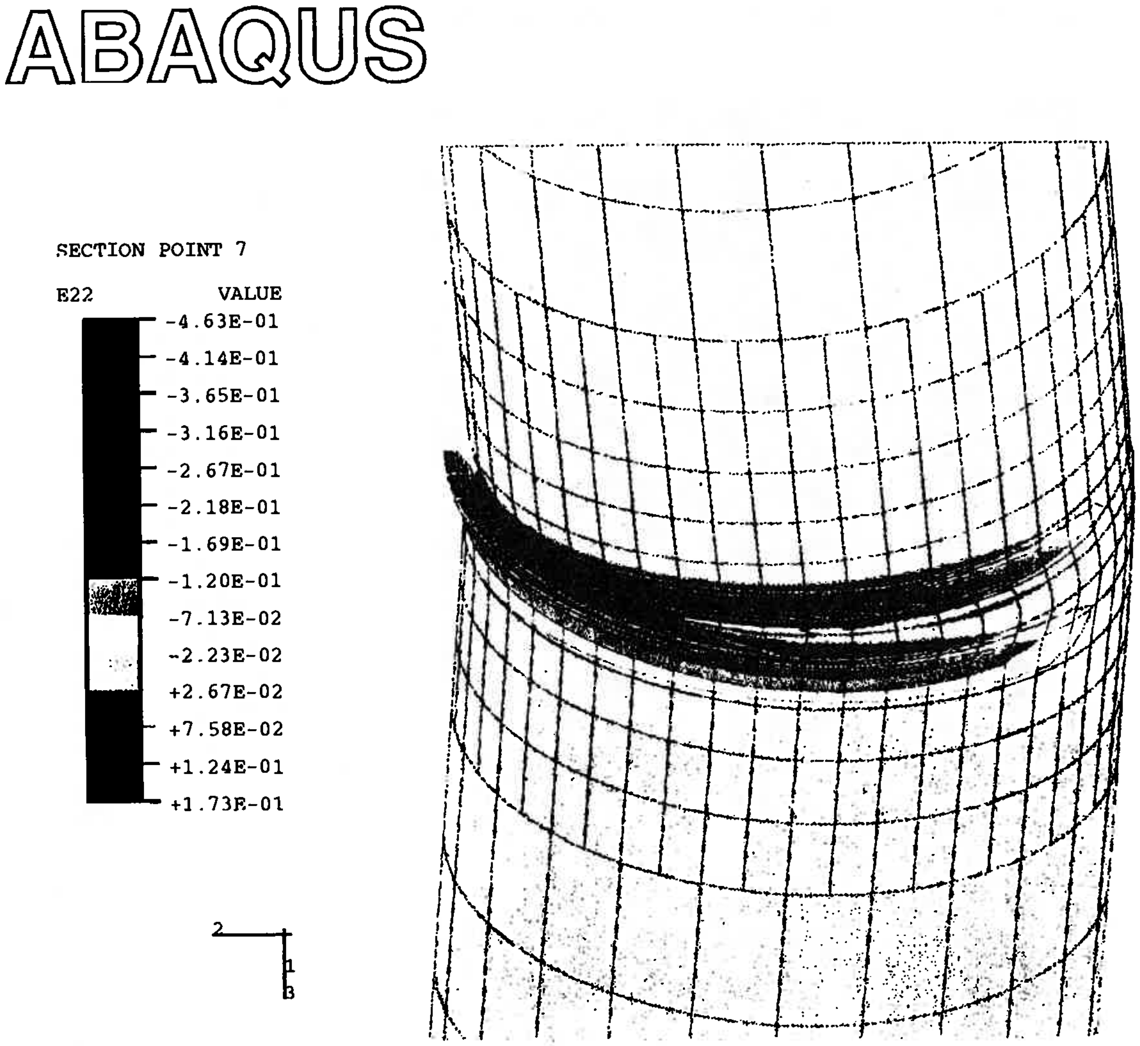

Figure 6.2.4. Longitudinal Strain (E22) at Section Point S7 for specimen UGA20WER4.

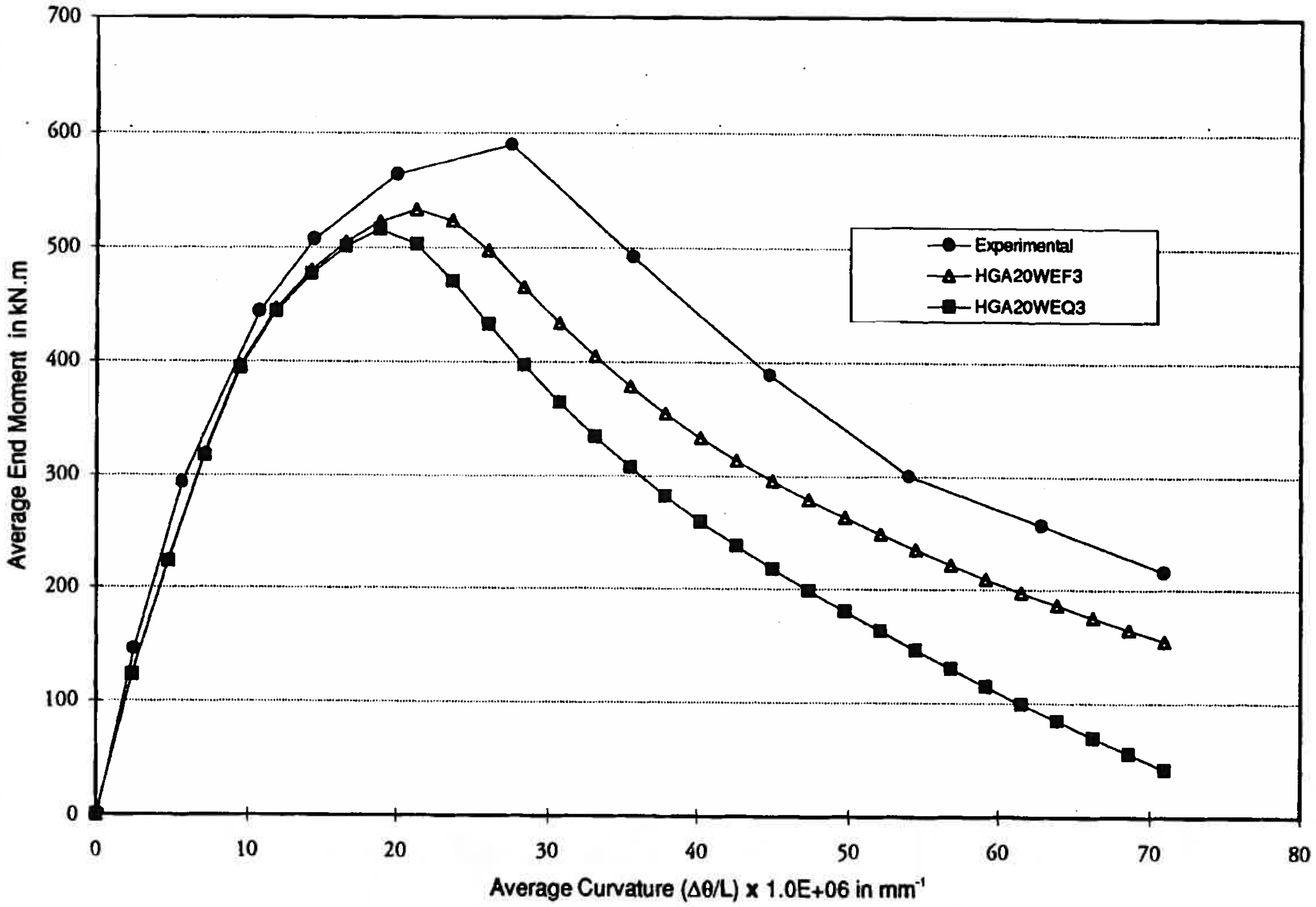

Figure 6.2.5. Influence of the element type on the moment vs. curvature curve for the half-pressurized 20-inch girth-welded pipe

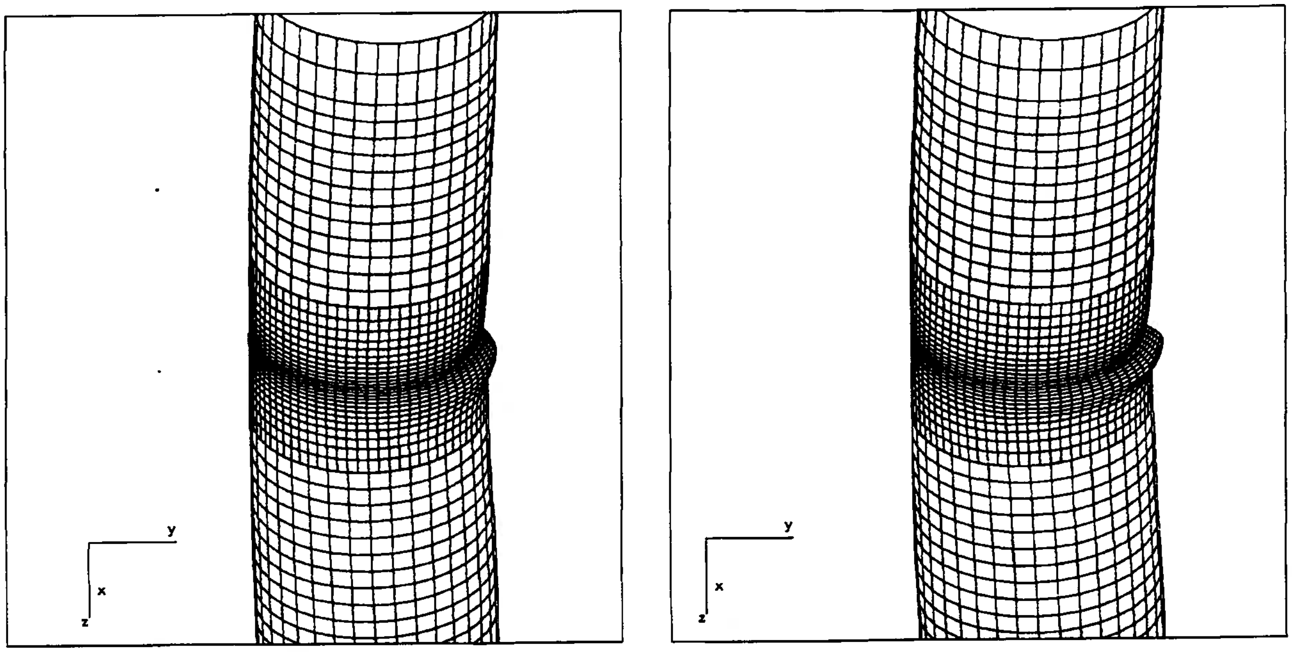

Point A. K= 26.03E-06 /mm. Magnification Factor = 2.0.

Point B. K= 52.05E-06 /mm. Magnification Factor = 1.0.

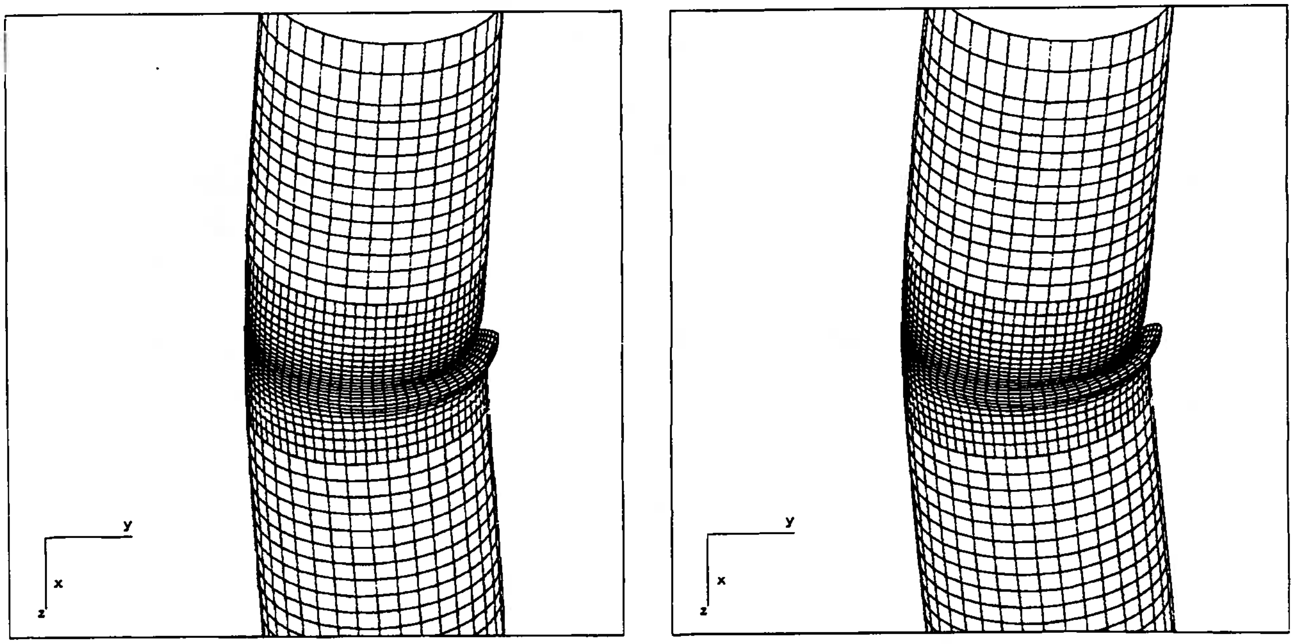

Point C. K= 73.32E-06 /mm. Magnification Factor = 1.0.

Point D. K= 96.93E-06 /mm. Magnification Factor = 1.0.

Figure 6.2.6. Evolution of buckling shape along the end moment vs curvature (K) curve for specimen HGA20WEQ3

7.0. INFLUENCE OF MISMATCH AND RESIDUAL STRESSES

In this section the influence of the initial geometric mismatch between the two cans at the junction for the weld, and of the residual stresses arising from the weld, are investigated. In the model that was used in Part A to simulate the girth-welded pipe, the residual stresses were introduced through the procedure involving a thermal cycle. In addition, initial imperfections were introduced into the model by the incorporation of an elliptical mismatch.

The influence of the mismatch is investigated first, for the 12-inch girth-welded empty pipe (specimens UGA12W). Later the influence of the residual stresses is investigated for the 20-inch pipe for the three load cases considered in the study (i.e., specimens UGA20, HGA20, DGA20).

7.1. Influence of Mismatch

The unpressurized 12-inch plain pipe (UGA12) is modelled using the mesh properties tabulated in Table 7.1.1, containing 432 9-node elements and 1827 nodal points. This mesh refinement #4 (denoted as mesh R4) is identical to mesh refinement #3, shown in Fig. 6.1.1.c, in the longitudinal direction. In the circumferential direction, however, it contains three more rows of elements outside the refinement region, and six more rows of elements within the refinement region. The three specimens which are analyzed in this section were all subjected to the thermal cycle described in Section 2.3 in order to produce the residual stresses. The specimen UGA12WPR4 does not have any mismatch (see Table 2.4.2). The specimens UGA12WER4 and UGA12WOR4 introduce misalignments of elliptical type and offset type, respectively (Sec. 2.4).

In Fig. 7.1.1 the curves for average moment vs. average curvature are shown corresponding to the analytical solutions for the three models identified above. The numerical results for the specimens are summarized in Table 7.1.1. The three specimens show very similar moment capacity, with less than 2 % difference. The maximum and minimum moment capacity occurred respectively for the specimens UGA12WPR4 and UGA12WOR4.

The final deformed shapes for each of these specimens, using Souza's PostSynas post processor, are shown in Figs. 7.1.2 to 7.1.4. In these plots, for plotting purposes only, each 9-node element is subdivided into four 4-node elements in order to reduce the concentration of slope discontinuity caused by the graphical representation of the 9-node elements as flat elements by PostSynas. For specimens UGA12WPR4 (Fig. 7.1.2) and UGA12WOR4 (Fig. 7.1.4) the specimens buckle as an outward bulge which is not located immediately adjacent to the row of girth-weld elements. In contrast, for specimen UGA12WER4 (Fig. 7.1.3) the characteristics of a diamond-shape pattern, similar to that exhibited by the specimen UGA12WEF3 and shown in Figs. 3.2.2 and 3.2.3, are evident. Consequently for the meshes using the 9-node element, the correct buckled shape (diamond shaped pattern) in the case of the 12-inch pipe is only achieved if the elliptical type of mismatch is employed. Other tests show that, for meshes using 4-node elements both elliptical and offset mismatches produce the correct prediction for the buckling shape for all pipe/load cases tested.

From experiences with these and other trial meshes to model the unpressurized 12-inch girth-welded pipe, it was determined that the elliptical out of roundness between adjacent cans such as used for Specimen UGA12WEF3, shown in Figs. 3.2.2 and 3.2.3, is most appropriate for the development of a diamond displacement pattern similar to the shape obtained in the experimental tests. For the 20-inch pipe (see Fig. 3.5.5) the introduction of mismatch seems to be less critical.

Table 7.1.1
Analytical Models for Investigating the Effect of Mismatch between Cans at Girth-Weld Joint

Specimen	Number of elements	Number of nodes	Maximum M (kN.m)	Curvature at Softening Point ($\times10^{-6}$ /mm)
UGA12WPR4	432	1827	184.41	23.67
UGA12WER4	432	1827	180.30	21.30
UGA12WOR4	432	1827	175.52	18.93

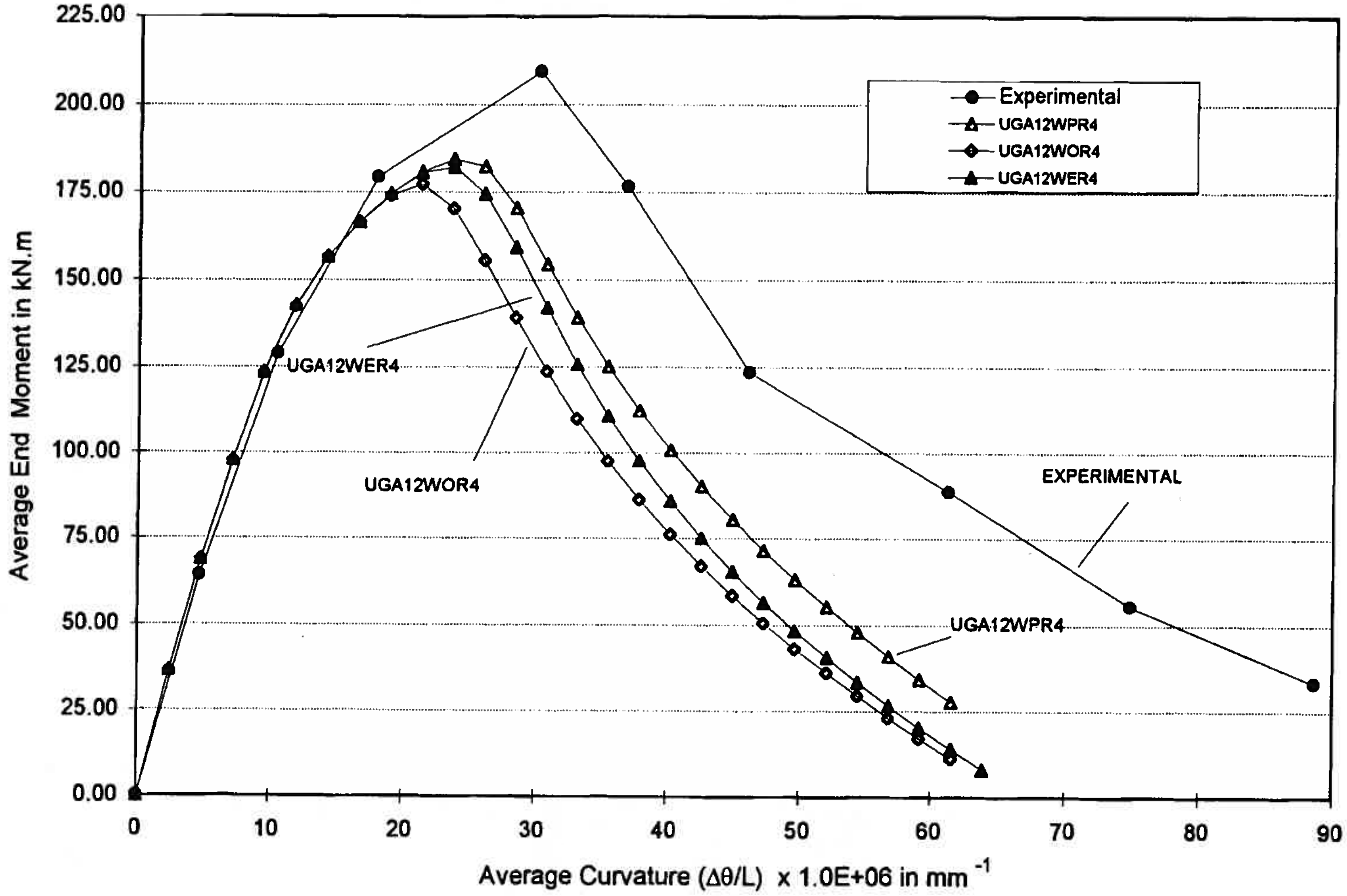

Figure 7.1.1. Effect of the mismatch on the moment vs. curvature curve for the 12-inch empty girth-welded pipe

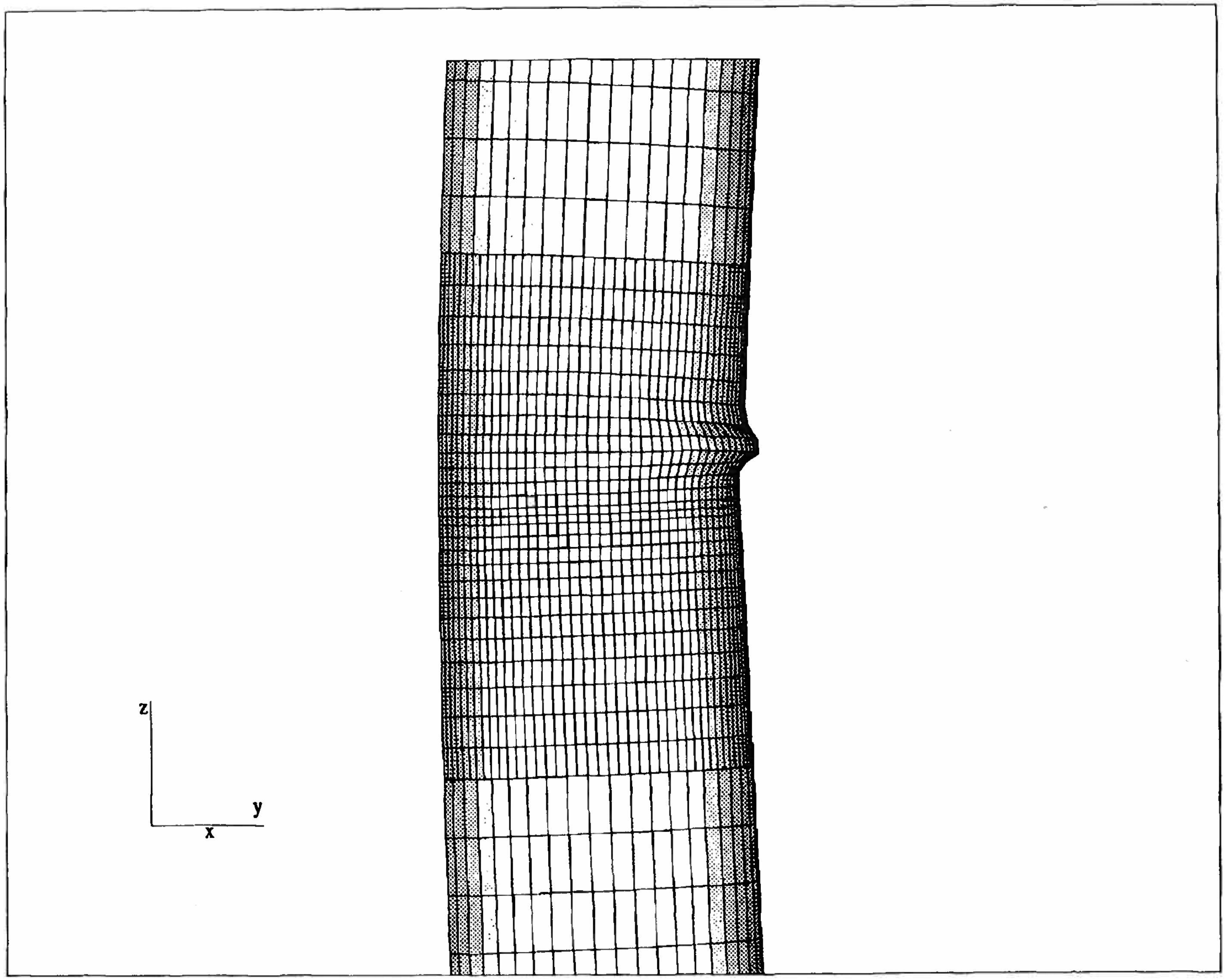

Figure 7.1.2. Final buckling shape for specimen UGA12WPR4

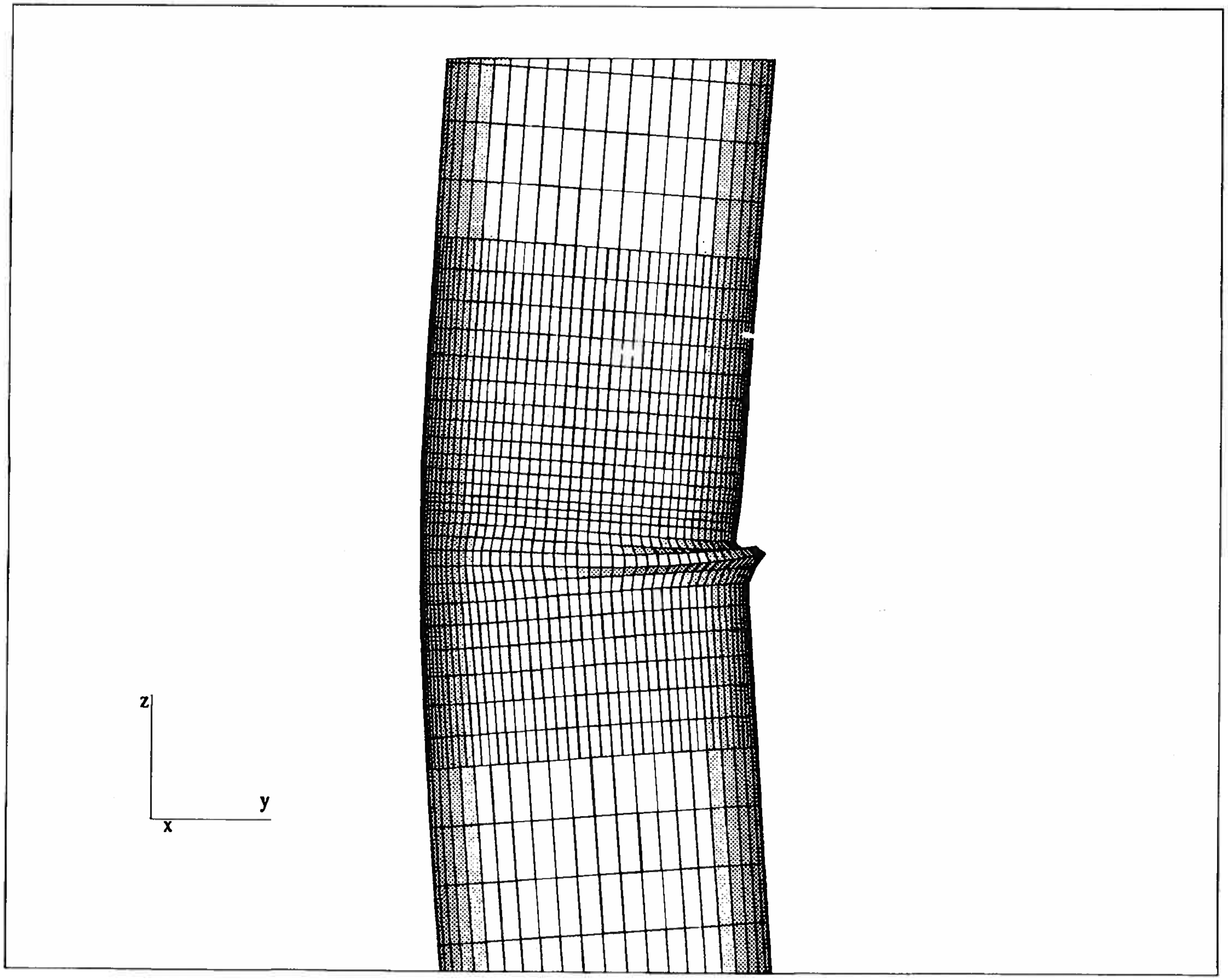

Figure 7.1.3. Final buckling shape for specimen UGA12WER4

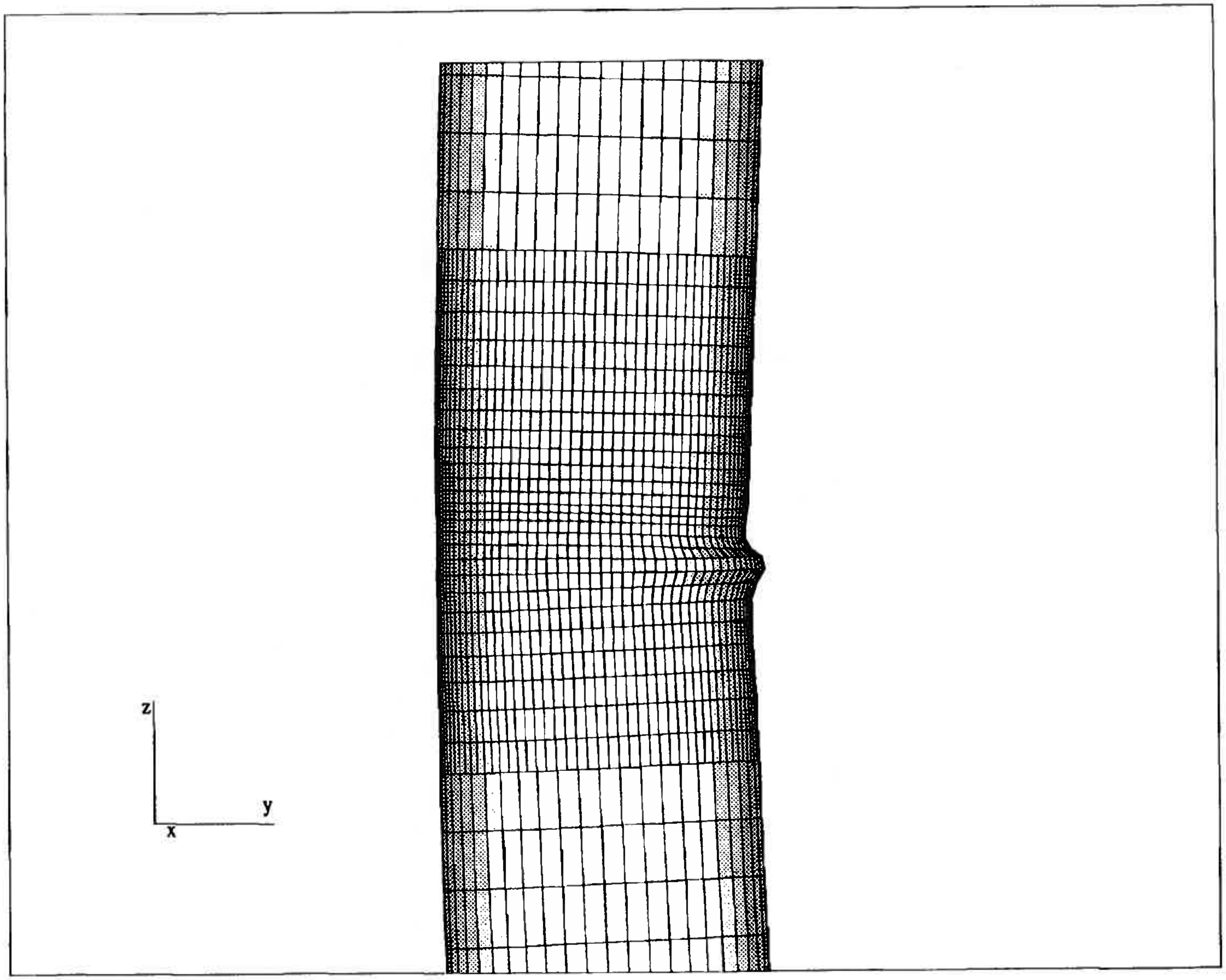

Figure 7.1.4. Final buckling shape for specimen UGA12WOR4

7.2. Influence of Residual Stresses

The influence of the residual stresses for the 20-inch pipe is examined in this section. The mesh used is the same as adopted in Part A (see Fig. 2.1.2), which consists of 1535 nodal points and 440 four-node finite strain elements. In the previous section the effect of the mismatch was investigated for the 12 inch pipe, while keeping the residual stresses the same for all the specimens being compared. The influence of the residual stresses can be determined if all the model properties are kept the same except for the treatment of the elements located in the girth weld. For all welded specimens of the type XGA20WEF3 the material used is that defined in Table 2.2.3. For the plain specimens of the type XGA20F3 the material properties are those of the base metal.

7.2.1 Specimens UGA20W and UGA20

The solution for UGA20F3 simulates the behavior of plain unpressurized pipe. The solution from UGA20WEF3 simulates the behavior of unpressurized welded pipe with an elliptical mismatch at the weld and including the effects of residual stresses. The numerical results for maximum moment and softening point curvature for all of the 20-inch specimens, with different levels of internal pressure, are summarized in Table 7.2.1. The average moment vs. average curvature curves for the specimens UGA20WEF3 and UGA20F3 are shown in Fig. 7.2.1. The difference between the two solutions is the effect of the girth weld. The softening point for the girth-welded model occurs at an average curvature 33% lower than the one from the plain pipe model. At the same time, the introduction of the misalignment and residual stresses has also affected the moment capacity. The maximum moment is 20% lower for the girth-welded model.

The evolution of the deformed shapes along the moment vs. curvature curves is shown in Figs. 3.5.2 and 7.2.2, for the specimens UGA20WEF3 and UGA20F3, respectively. The solutions obtained for both of these specimens results in alternating diamond-shape deformation patterns, similar to those occuring in the experimental tests conducted by Mohareb, *et al*, (1994). For the plain model, however, the diamond-shape buckle occurs at a distance from the middle of the pipe approximately of the order of the half-width of the refinement region. The experimental post-buckling configuration of this plain pipe specimen is that shown in Fig. 6.1.8.

7.2.2 Specimens HGA20W and HGA20

The solutions for the average moment vs. average curvature curves for specimens HGA20WEF3 and HGA20F3, which correspond to the half-pressurized 20-inch pipe, with and without the consideration of the residual stresses are compared in Fig. 7.2.3. The results for these specimens are included in Table 7.2.1. The softening point for the girth-welded specimen in this case occurs at an average curvature 15% lower than that for the plain pipe model. The introduction of the misalignment and residual stresses also affected the moment capacity, resulting in a maximum moment 8% lower for the girth-welded model. The evolution of the deformed configuration along the moment vs. curvature curves is shown in Figs. 3.6.2 and 7.2.4 for the specimens HGA20WEF3 and HGA20F3, respectively. The solutions obtained for both specimens result in a single outward bulge similar to the experimental tests. However, unlike for the plain model, the buckle for the girth-welded specimen starts developing in the neighborhood of the weld.

7.2.3 Specimens DGA20W and DGA20

The solutions for the average moment vs. average curvature curves for the specimens DGA20WEF3 and DGA20F3, which correspond to the fully-pressurized 20-inch pipe with and without the consideration of the residual stresses, respectively, are compared in Fig. 7.2.5. The results for these specimens are included in Table 7.2.1. The softening point for the girth-welded model in this case occurs at an average curvature 10 % lower than that for the plain pipe. The introduction of the misalignment and the residual stresses affects the moment capacity only marginally, being 2 % lower for the girth-welded model.

The evolution of deformed configuration along the moment vs. curvature curves is shown in Figs. 3.7.2 and 7.2.6 for the specimens DGA20WEF3 and DGA20F3, respectively. For the girth-welded specimen a single outward bulge occurs at a distance from the middle of the pipe of the order of the width of the refinement region. A second bulge starts to develop at the end of the loading history. For the plain pipe two outward bulges developed symmetrically about the middle of the pipe. Therefore, although the moment vs. curvature response was only slightly affected by the introduction of the residual stresses, the resulting buckled shapes differ significantly between the two models.

Table 7.2.1
Analytical Models for Investigating the Effect of Residual Stresses on Girth-Welded Pipe Specimens

Specimen	Number of elements	Number of Nodes	Maximum M (kN.m)	Curvature at Softening Point ($\times 10^{-6}$ /mm)
UGA20WEF3	1440	1535	527.97	14.20
UGA20F3	1440	1535	657.89	21.30
HGA20WEF3	1440	1535	533.25	26.03
HGA20F3	1440	1535	581.21	30.76
DGA20WEF3	1440	1535	399.04	44.95
DGA20F3	1440	1535	406.82	49.69

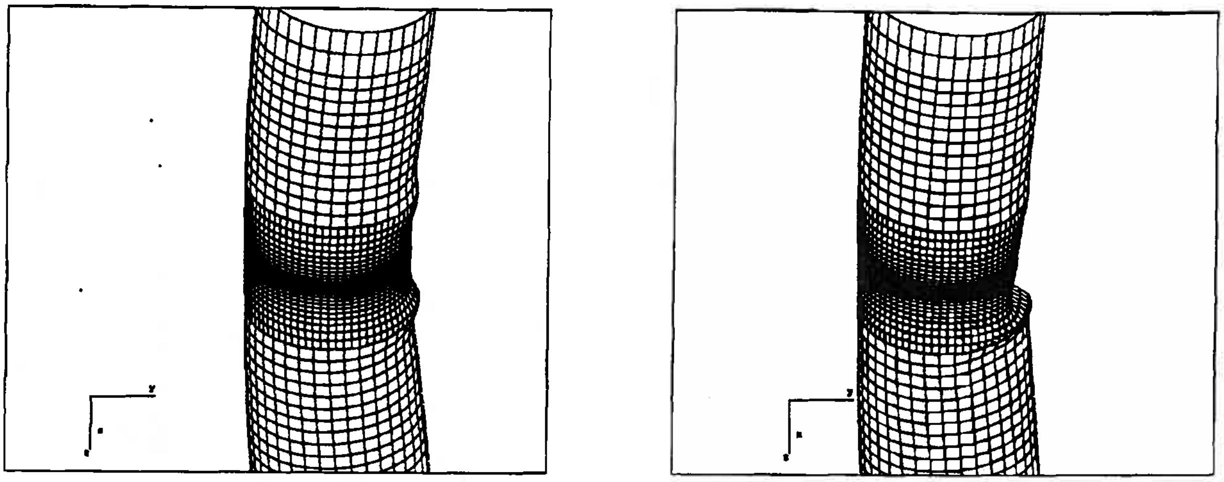

(a) K = 26.03E-06 /mm. Magnification Factor = 4.0.

(b) K = 37.87E-06 /mm. Magnification Factor = 2.0.

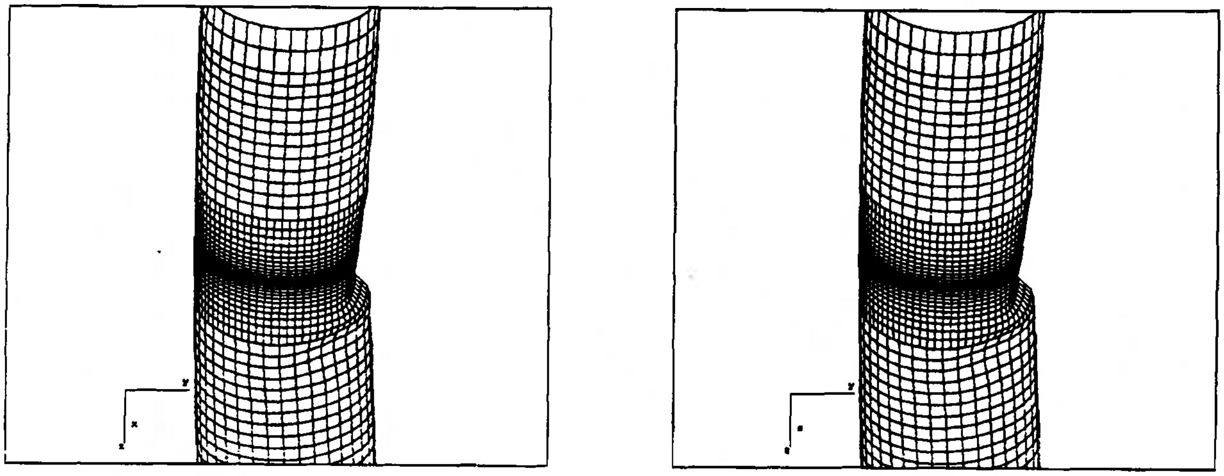

(c) K = 49.70E-06 /mm. Magnification Factor = 1.0.

(d) K = 61.54E-06 /mm. Magnification Factor = 1.0.

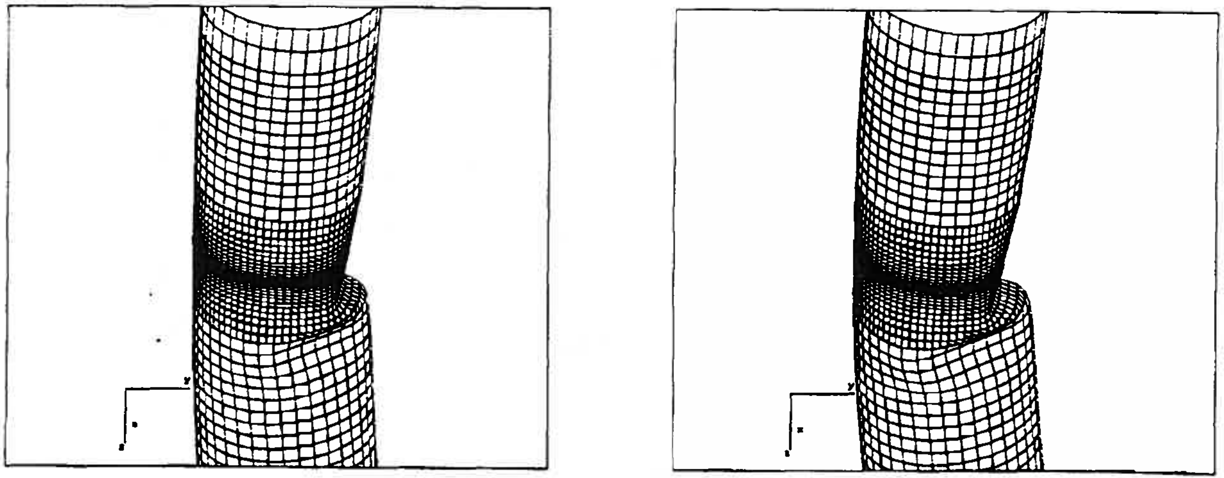

(e) K = 75.74E-06 /mm. Magnification Factor = 1.0.

(f) K = 99.41E-06 /mm. Magnification Factor = 1.0.

Figure 7.2.2. Evolution of buckling shape along the end moment vs. curvature (K) curve for specimen UGA20F3

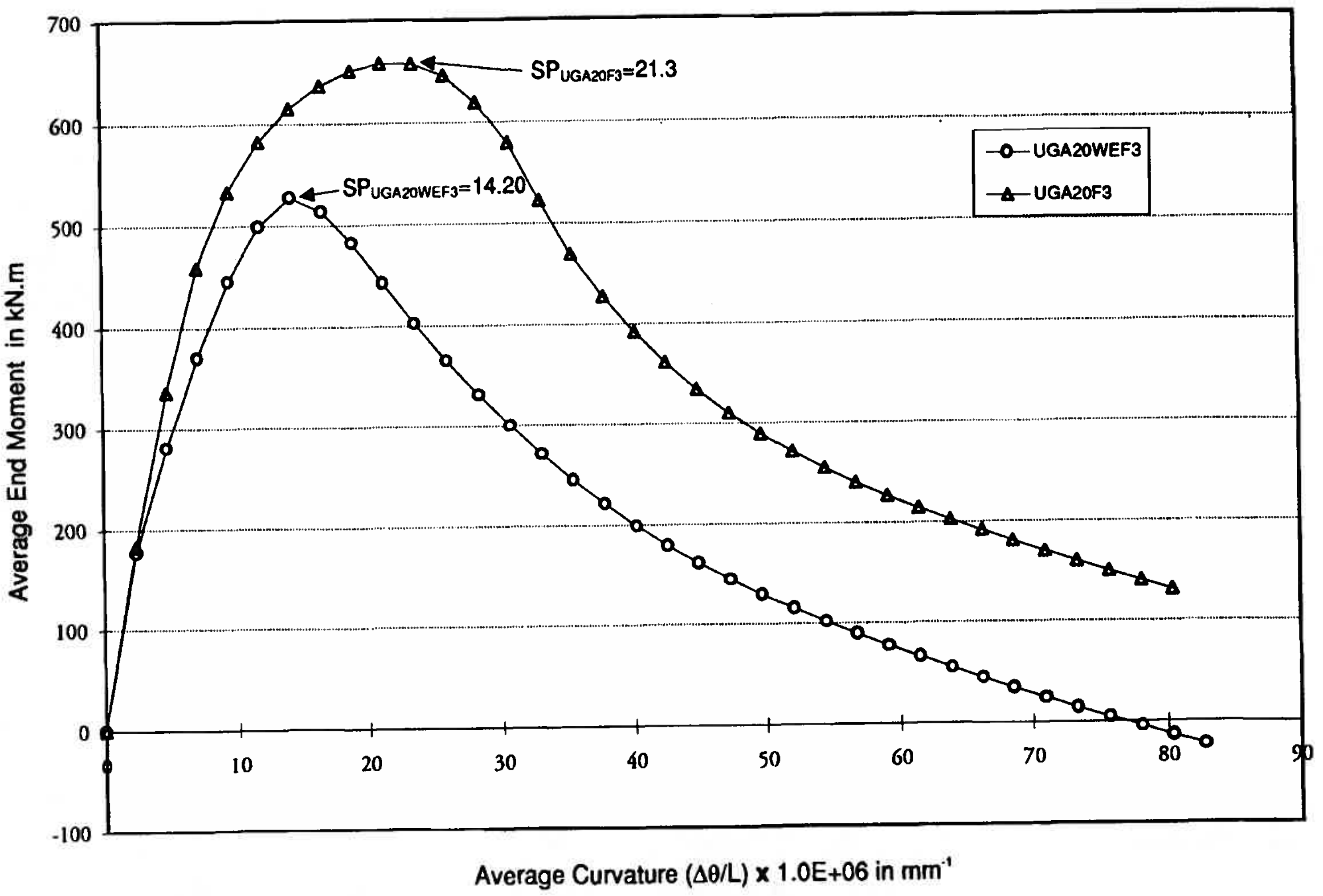

Figure 7.2.1. Effect of the residual stress and initial imperfection on the moment vs. curvature curve for the empty 20-inch pipe

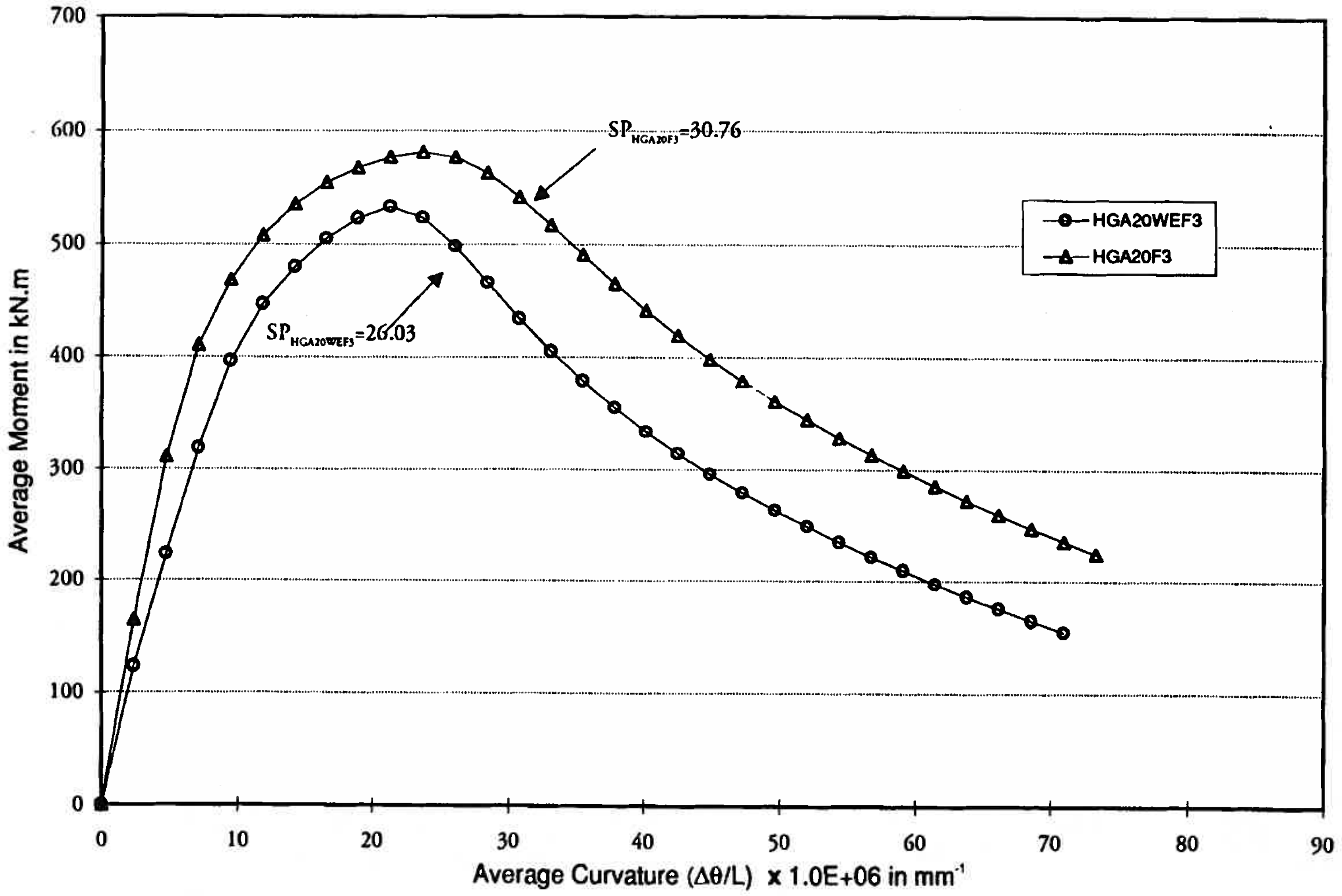

Figure 7.2.3. Effect of the residual stress and initial imperfection on the moment vs. curvature curve for the half-pressurized 20-inch pipe

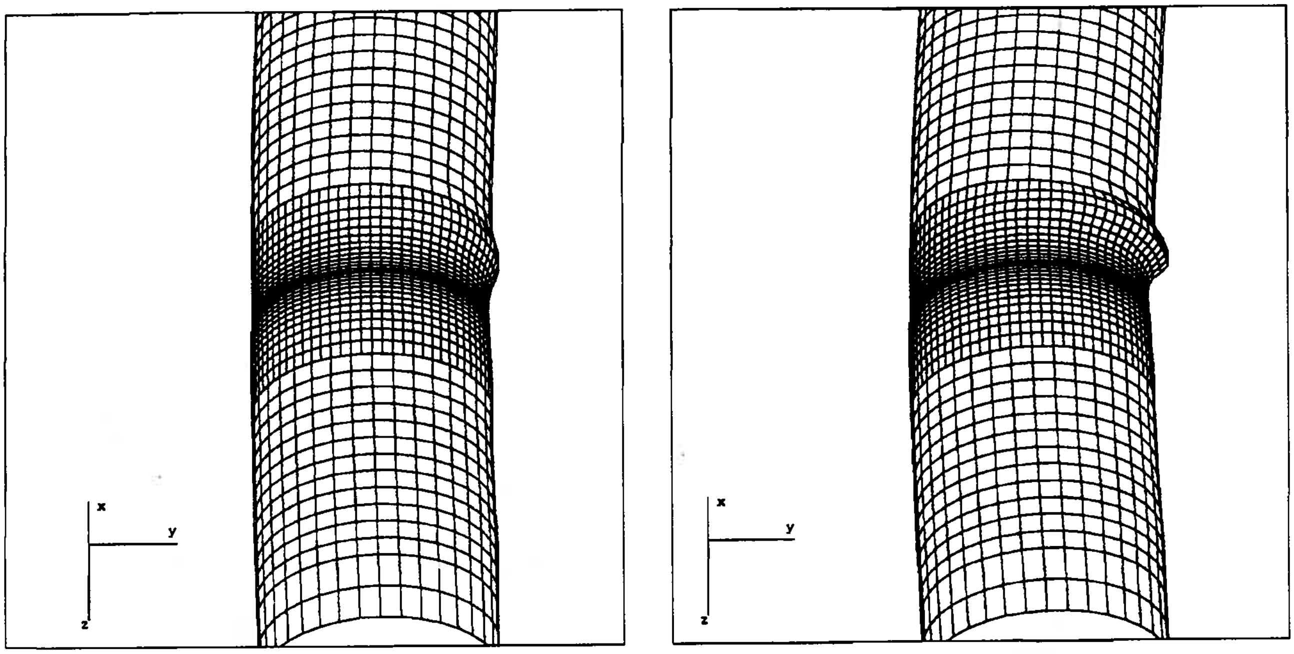

(a) K = 34.56E-06 /mm. Magnification Factor = 1.0.

(b) K = 56.16E-06 /mm. Magnification Factor = 1.0.

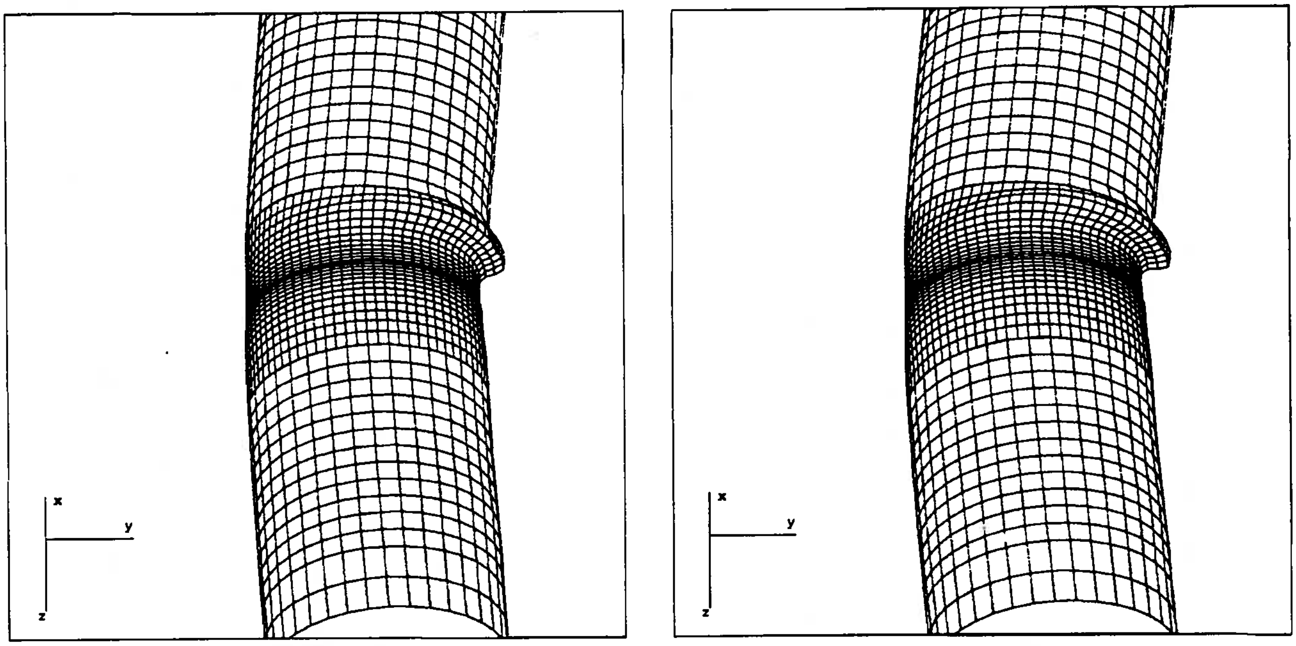

(c) K = 75.60E-06 /mm. Magnification Factor = 1.0.

(d) K = 95.04E-06 /mm. Magnification Factor = 1.0.

Figure7.2.4. Evolution of buckling shape along the end moment vs. curvature (K) curve for specimen HGA20F3

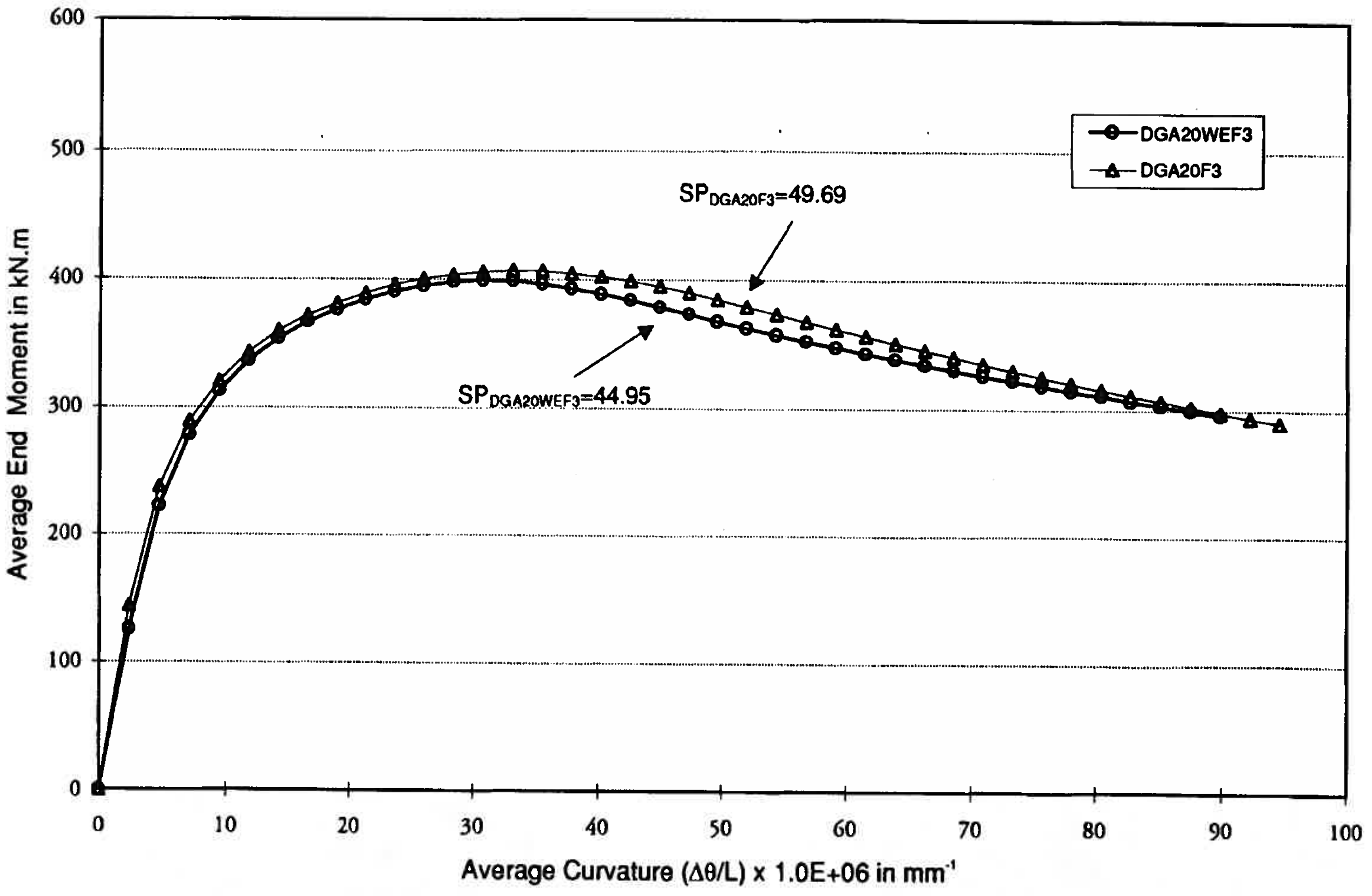

Figure 7.2.5. Effect of the residual stress and initial imperfection on the moment vs. curvature curve fully pressurized 20-inch pipe

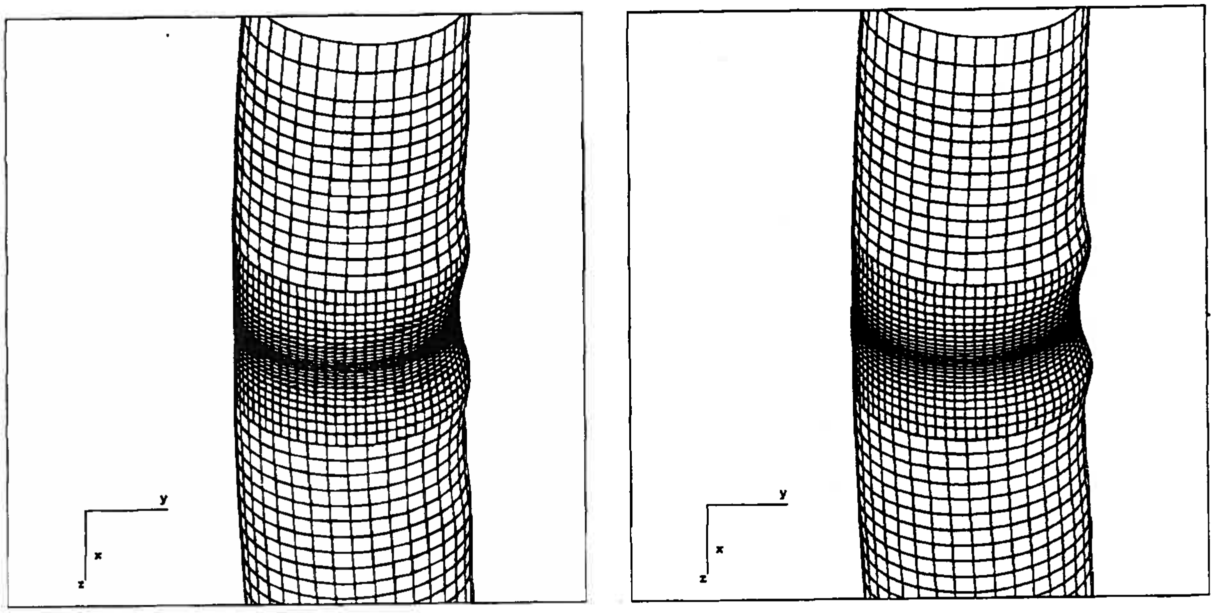

(a) K = 34.56E-06 /mm. Magnification Factor = 2.0.

(b) K = 56.16E-06 /mm. Magnification Factor = 1.0.

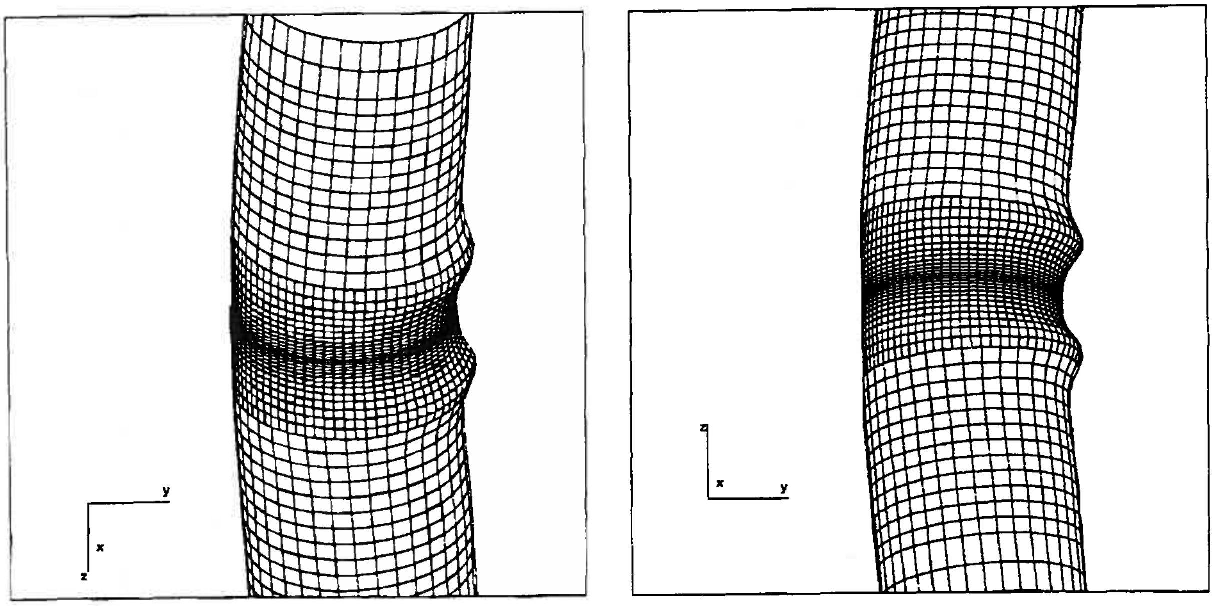

(c) K = 77.76E-06 /mm. Magnification Factor = 1.0.

(d) K = 99.36E-06 /mm. Magnification Factor = 1.0.

Figure7.2.6. Evolution of buckling shape along the end moment vs. curvature (K) curve for specimen DGA20F3

8.0 OBSERVATIONS ON EFFECT OF MODELLING ON LOCAL BUCKLING AND WRINKLING SOLUTIONS FOR LINE PIPE

8.1 Influence of Finite Strain

In Section 6.2 the solutions using the 4-node finite strain element were compared with the solutions using 9-node and 4-node elements whose formulation are based on the hypothesis of large displacement and small strains. Although the use of finite strain elements influences the solution, particularly with respect to the moment vs. curvature response, the solutions obtained from other elements also produced a correct pattern of deformation for the deformed shapes. Nevertheless, from the comparisons made in Sec. 6 we can conclude that the consideration of the finite strain improves the solution. The larger the region of the pipe subjected to strains of finite magnitude, the more noticeable is the improvement using finite strain elements over the other element types. In all pipe/load cases analyzed in this study the region where strains of finite magnitude occur is very localized, being located where the wrinkles develop. For this reason, the other types of finite elements not based on finite strains can still produce correct global responses up to the softening point but may have difficulty in following the configuration in the region of the wrinkles.

8.2 Evolution of Deformed Configuration in Post-buckling Regime

The development of the local bucking modes for the pipes modelled in this study share some common characteristics. For all models of the pipe/load cases analyzed, a simple buckling mode of the bulge type starts to develop following the limit point. For the half-pressurized and fully-pressurized pipes this buckling mode amplifies along the descending branch of the moment vs. curvature curve. As has been verified in the solutions for specimen UGA12W (Sec. 7.1), and for specimens UGA20, HGA20 and DGA20 (Sec. 7.2), the deformed shape which develops subsequently to local buckling is influenced by the nature of the initial imperfection. The initial imperfection appears to trigger a particular buckling mode.

For the unpressurized pipes, after the wrinkle has been substantially developed, the pattern of deformation starts to develop inward, while the bulge progressively decreases in amplitude. This mechanism can be associated with an evolution of the initial buckling mode, which is similar in all pipes, to a higher mode that includes diamond-shape patterns. The fully developed diamond-shape buckle, however, is completely developed only at the end of the loading history.

The evolution of the deformed shape for the pipes can be followed in the analytical study, due to the displacement/rotation-solution control of the incremental procedures.

This allows for increase of rotation simultaneously with the reduction of the moment. The end moments in this case are reactive forces determined to equilibrate the finite element incremental solutions. In experimental tests, however, it may be difficult to follow the evolution of the buckling shape if the tests are load-controlled and the passage from one buckling mode to another occurs suddenly.

8.3 Recommendations for Modelling of Pipe Wrinkling

Throughout this study several comparisons have been made in order to explore the influence of the different aspects of the finite element modelling on the analytical results. The motivation was to develop a modelling technique that could be used to produce reliable results for the modelling of pipe wrinkling phenomena.

It can be concluded that the mesh plays an important role in the model. The discretization should be defined not only in terms of number of elements and degrees-of-freedom but also the mesh itself must be capable of incorporate buckling modes that are expected to occur during the incremental post-buckling analysis. The degree of mesh refinement adopted in this study seems to have satisfactorily fulfilled this requirement, due to the correct prediction of deformed shapes. In addition the model is capable of representing the girth weld by a single row of elements of approximately of the same width as the physical weld.

When elements for welds are required the refinement of the mesh in the longitudinal direction should be gradual. Abrupt changes in element size appear to influence the shapes of the deformed configurations that develop and consequently follow the wrong bifurcation path in the solution space. The finite strain shell element should be used in the analysis program when it is available if the analyst wishes to explore wrinkles of large amplitude. However, other types of large displacement shell elements produce reasonable and realistic results, without compromising the solution, for wrinkles of moderate amplitudes.

The incorporation of residual stresses and initial imperfections of the mismatch type were necessary for the correct prediction of buckling modes for the empty pipe and should be included in the model.

The displacement-control analysis by the imposition of rotational boundary conditions yields very smooth load-deflection curves and convergence problems did not occur to any of the specimens tested. The size of the rotation increments, while not critical, may force the structure to skip over bifurcations for lower buckling modes if the increments are too large. This was experienced for some analytical results not presented here, in the early part of this study when the size of the rotation increments to be adopted for this study were being investigated. Because such solutions are completely erroneous they must be avoided. On the other hand, if the analyst is reasonable in his expectations it is not difficult to avoid this problem. It appears that solutions for which the boundary displacement increment sizes are controlled to reach the limit point in 10 to 15 increments are reliable and that this degree of refinement in the load control is sufficient to eliminate potential problems.

Realistic temperature-dependent material properties for the weld should be determined to place the thermal analysis on a firm basis. In this study the data used was the only data available to the knowledge of the authors. The base metal properties should also be determined from properly conducted tests.

APPENDIX A : REFERENCES

Hibbitt, Karlsson & Sorensen, Inc., (1992a). *ABAQUS Theory Manual v. 5.2.* Pawtucket, RI 02860-4847

Hibbitt, Karlsson & Sorensen, Inc., (1992b). *ABAQUS User's Manual I v. 5.2,* Pawtucket, RI 02860-4847

Hibbitt, Karlsson & Sorensen, Inc., (1992c). *ABAQUS User's Manual II v. 5.2,* Pawtucket, RI 02860-4847

Swanson Analysis System, Inc., (1989a). *ANSYS User's Manual v. 4.4*

Swanson Analysis System, Inc., (1989b). *ANSYS Theatrical Manual v. 4.4*

API, (1977). *Specification for Fabricated Structural Steel Pipe,* Spec. 2B, Third Edition, American Petroleum Institute, Washington, November 1977

Arbosz, J., (1983). "Shell stability analysis: Theory and Practice", *Collapse: The Buckling of Structures in Theory and Practice.*(ed.: J.M.T. Thompson and G.W. Hunt), Cambridge University Press, Cambridge, 1983. (Proceedings of the I.U.T.A.M. Symposium, University College London, 31 August 1982)

Brush, D.O. and B.O. Almroth, (1975). *Buckling of Bars, Plates and Shells*, McGraw-Hill, New York, 1975

Bushnell, D., "Static Collapse: A Survey of Methods and Modes of Behavior", *Finite Elements in Analysis and Design*, 1985, pp. 165-205

Coy S., (1992). *Vivid 386 User's Manual v. 2.0*

Elishakoff, I., (1983). "How to introduce the imperfection sensitive concept into design", *Collapse: The Buckling of Structures in Theory and Practice* (ed.: J.M. Hunt), Cambridge University Press, Cambridge, 1983)

Heuser,A, R. Twickler, and W. Dahl, (1987). "Experimental Investigations of the Failure Behaviour of Welded Joints and its Numerical Simulation by Using Elastic-Plastic Finite Element Calculations", *The Fracture Mechanics of Welds*, EGF Pub. 2 (Edited by J.G. Blauel and K.H. Schwalbe), Mechanical Engineering Publications, London, 1987, pp. 97-124.

Hu, S., (1991). *An Analytical Investigation of the Compressive Behavior of Fabricated Steel Tubes*, Ph.D. Dissertation, Dept. of Civil Engineering, University of Toronto, Toronto-ON, Canada, 1991

Krätzig, W.B., Y. Basar and U. Wittek, (1982). "Nonlinear behavior and elastic stability of shells - Theoretical Concepts - Numerical Computations - Results", *Buckling of Shells*, Proceedings of the State-of-the-Art Colloqium, Universität Stuttgart, Germany, May 6-7, 1982, Ed.: E. Ramm, Springer-Verlag, 201-236, 1982.

Marion, T.L., (1989). *Casing Formation Interaction Model for Thermal Recovery Wells*, Centre for Frontier Engineering Research, January 1989.

Ramm, E., (1980)."Strategies for tracing nonlinear response near limit points", *Europe-US-Workshop: Nonlinear Finite Element Analysis in Structural Mechanics*, July 28-31, 1980.

Riks, E., (1979). "An incremental approach to the solution of snapping and buckling problems", *Int. J. Solids Struct.*, Vol 15, pp. 529-551, 1979

Singer, J., (1980). *Buckling Experiment on Shells - A Review of Recent Developments*, Technion Israel Institute of Technology, Department of Aeronautical Engineering Report TAE N. 403, 1980.

Stegmüller, H., (1984). *Nonlinear Inelastic Structural Analysis (NISA) - The User Manual*, Institute Fur Baustatik, Universität Stuttgart, Stuttgart, West Germany, 1984

Souza, L.T., (1991). *Um sistema para análise incremental estática e dinâmica de cascas em processo de flambagem com computação gráfica interativa*, Ph.D. Dissertation, Pontifícia Universidade Católica do Rio de Janeiro, Rio de Janeiro, Brazil, 1991

Souza, L.T.(1994). *SYNAS - A system for nonlinear analysis of shells - User's Manual v. 1.0,*, 1994 (to be published)

Timoshenko, S.P. and J.M. Gere, (1961).*Theory of Elastic Stability*, McGraw-Hill, New York, 1961

Zhou, Z. and Murray, D.W., (1993). *Numerical Structural Analysis of Buried Pipelines*, Structural Engineering Report 181 Dept. of Civil Engineering, University of Alberta, Edmonton-AB, Canada, 1993

APPENDIX B

REFERENCES AND PUBLICATIONS ARISING FROM U OF A STRUCTURAL PIPELINE RESEARCH

B1. Mohareb, M., Elwi, A.E., Kulak, G.L., and Murray, D.W. (1994). **Deformational Behavioral of Line Pipe,** Structural Engineering Report No. 202, Department of Civil Engineering, Univ. of Alberta, Edmonton, AB. T6G 2G7

B2. Mohareb, M., Zhou, Z., Kulak, G.L., and Murray, D.W. (1992). **Preliminary Report on Test Results for 12 x 0.25 inch X52 Grade Line Pipe,** Internal Report to Interprovincial Pipe Line Co. Ltd., Department of Civil Engineering, Univ. of Alberta, Edmonton, AB. 22 pgs.

B3. Mohareb, M., Alexander, S.D.B., Kulak, G.L., and Murray, D.W. (1993). **Laboratory Testing of Line Pipe to Determine Deformational Behavior,** Proc. of the 12th Inter. Conf. on OMAE, Vol. V-Pipeline Technology, ASME, pp. 109-114.

B4. Yoosef-Ghodsi, N., Elwi, A.E., Kulak, G.L., and Murray, D.W. (1994a). **Preliminary Report: Test Results for 12.75 x 0.25 Inch Diameter ERW X52 Grade Girth-Welded Pipes,** Internal Report to Interprovincial Pipe Line Co. Ltd., Edmonton, AB, 45 pgs.

B5. Yoosef-Ghodsi, N., Kulak, G.L., and Murray, D.W. (1994b). **Behavior of Girth-Welded Line Pipe,** Structural Engineering Report No. 203, Department of Civil Engineering, Univ. of Alberta, Edmonton, AB. T6G 2G7.

B6. Zhou, Z., and Murray, D.W.(1993a), **Numerical Structural Analysis of Buried Pipelines,** *Structural Engineering Report 181*, Dept. of Civil Engineering, Univ. of Alberta, Edmonton AB, Canada T6G 2G7. 355 pgs.

B7. Zhou, Z., and Murray, D.W. (1993b). **Behavior of Buried Pipelines Subjected to Imposed Deformations.** Proc. of the 12th Inter. Conf. on OMAE, Vol. V - Pipeline Technology, ASME, pp. 115-122.

B8. Zhou, Z., and Murray, D.W. (1993c). **Towards Rational Deformation Limit States for Buried Pipelines.** Proc. of the 3rd ISOPE Conf., Vol II, pp. 18-24.

B9. Zhou, Z., and Murray, D.W.(1994a). **Analysis of Postbuckling Behavior of Line Pipe Subjected to Combined Loads.** Submitted to the International Journal of Solids and Structures. July 19, 1993.

B10. Zhou, Z., and Murray, D.W.(1994b). **Formulation and Verification for Pipeline Beam Models Using Stiffness-Property-Deformation Relations.** Submitted to the International Journal of Solids and Structures. July 19, 1993.

B11. Zhou, Z., and Murray, D.W.(1994c). **An Incremental Solution Technique for Unstable Equilibrium Paths of Shell Structures.** Submitted to Computers and Structures, Dec. 14, 1993.